Galactic cosmic rays from star clusters and nearby supernovae remnants

A THESIS
SUBMITTED FOR THE DEGREE OF
Doctor of Philosophy
IN THE FACULTY OF SCIENCE

by

Sourav Bhadra

Under the supervision of
Prof. Biman B. Nath (Raman Research Institute)
Prof. Prateek Sharma (Indian Institute of Science)

Joint Astronomy Program
Department of Physics
Indian Institute of Science
Bangalore – 560 012, INDIA

July 2024

Declaration

I, Sourav Bhadra, hereby declare that the work reported in this doctoral thesis titled 'Galactic cosmic rays from star clusters and nearby supernovae remnants' is entirely original and is the result of investigations carried out by me under the supervision of Prof. Biman Nath & Prof. Prateek Sharma at the Department of Astronomy and Astrophysics, Raman Research Institute under the joint astronomy program hosted by the Department of Physics, Indian Institute of Science, Bangalore.

I further declare that this work has not formed the basis for the award of any degree, diploma, fellowship, associateship, or similar title of any University or Institution.

Date: Tuesday 28th January, 2025
Bangalore, India

Sourav Bhadra
Department of Physics
Indian Institute of Science

To,
My parents,
Shri Pashupati Bhadra
&
Smt. Sima Bhadra

Acknowledgements

Still, I can recall that day very well from my childhood, as if it is a matter of just yesterday. It was a popular science seminar arranged by my school where I was first introduced to some pictures of astrophysical objects and phenomena. At that time they seemed to be some wonderful pictures to me, but in the deep of my mind, I was attracted too much by those figures. The articles on stars, galaxies, nebula, and various astrophysical objects and phenomena in popular science books always fascinated me from my school days. Having been born in a small town I had enough opportunity to stare at the pollution-free night sky for hours. I was always interested in identifying the various constellations and would be overwhelmed by the extent of this infinite universe. All these things planted the seed of a future astrophysicist in me.

When I was in my undergraduate studies at Jadavpur University, I became sure that I was destined to pursue my higher studies in astrophysics. My interest grew immensely when I started reading popular books on astrophysics during my under graduation. During this time, I started to read some very basic books on astrophysics under the guidance of a faculty member in my department. However, I needed more mathematical insight to get a proper understanding of natural phenomena occurring at a very large length scale. So, I decided to choose astrophysics and cosmology as my special paper in my post-graduation which piqued my interest in this field. The decision to join the IISc astrophysics and astronomy doctoral program was driven by all this background knowledge in astrophysics. I am grateful to my supervisors Prof Biman Nath and Prof Prateek Sharma, who have been very supportive throughout my research journey. They have been excellent mentors to guide me through the complex trajectory of a Ph.D life and enhanced my curiosity to learn even more. I enjoyed working with Siddhartha Gupta, and Satyendra Thoudam, who have provided insightful understandings of my research and helped me in every possible way during my research. I would like to thank Prof Shiv Sethi and Prof Vikram Rana for their suggestions as my PhD committee members. I acknowledge the Prime Minister's Research Fellowship (PMRF) and Govt. of India for providing the financial support for the full PhD tenure. I am grateful to Prof Tarundeep Saini and Prof Ranjan Laha for providing me with helpful suggestions during my PMRF review processes.

I am thankful to the Chairman of the Department of Physics for providing me a chance to pursue a research career in astrophysics in that department. I am grateful to the Director of Raman Research Institute (RRI) for providing me with a wonderful research environment. I also thank the current Astronomy group secretary for helping process the official work. I want to thank the RRI library staff for maintaining important books and journals, moreover, for arranging the books and journals if they are not present in the library. I am thankful to all the academic staff in the RRI astrophysics and IISc physics departments for discussing various aspects of science during various periods of my life here in Bangalore. My sincere thanks to Naren da, Anjan da, Manami, and Ranita di for their support in my academic and personal life. I am also thankful to all the faculty members of the IISc astrophysics group and the Astronomy & Astrophysics division, RRI.

I thank all my friends in RRI and IISc for converting a hectic research life into five enjoyable years. A big thanks to Jyotirmoy Mukherjee, and Chitrak Sarkar for supporting me through the thick and thin of my life. I have enjoyed spending time with my friends Sandeep, Anirban, Mukesh, Manish, Kinjal, Dipanshu, Gunjan, and Shovan in RRI, who have been a large part of my Ph.D life. I would like to thank my IISc friends Alankar, Ritali, Arpit, Yashi, and Ashwin for being part of my journey. I especially thank all the members of our RRI cricket team for making the weekends filled with cheers. The acknowledgement is truly not complete without mentioning my parents who have supported me in every phase of my life. I am lucky to have them.

Preface

Cosmic rays (CRs) are high-energy particles, predominantly originating from outside the Earth's atmosphere. These particles, ranging from protons to heavier nuclei, propagate through space at nearly the speed of light, carrying immense amounts of energy. Those are believed to come from sources from our galaxy (such as supernovae explosions, young massive star clusters, etc) as well as from outside of our galaxy (such as black holes, radio galaxies, and other energetic events in the universe). It is important to understand various sources, especially particle acceleration mechanisms in different energy ranges in these systems and several phenomena associated with particle propagation. In this thesis, we explore young massive star clusters as potential cosmic ray accelerators, particularly in the TeV-PeV energy range. Based on recent gamma-ray observations from young star clusters, we use numerical simulations and phenomenological models to explain the various aspects of cosmic ray acceleration and propagation. Our results shine light on many interesting features, such as (i) recent gamma-ray observations from young star cluster Westerlund1 can be associated with underlying cosmic rays that are accelerated in this environment, (ii) the cosmic rays originating from a distribution of massive star clusters in the Galaxy can act as potential second component of Galactic cosmic rays, (iii) the effect of nearby cosmic ray sources on the observed spectra. We connect our numerical and analytical work with available cosmic-ray data, γ-ray data, and X-ray observation. We also develop numerical models that solve the propagation equation of cosmic rays considering different associated microphysics. Using this model we try to explain different observed spectral features of different cosmic ray elements.

Cosmic ray induced gamma-ray observation from young star clusters

We investigate the implications of cosmic ray acceleration within the massive compact star cluster Westerlund 1, following its recent detection in γ-rays (Aharonian et al., 2019; Abeysekara et al., 2021). Recent observations unveil a radial distribution of the CR energy density following a $1/r$ profile. We delve into whether this profile can serve as a discriminator between two debated scenarios: (1) continuous CR acceleration within stellar wind-driven shocks in the star cluster and (2) discrete CR acceleration within multiple supernova shocks. Utilizing idealized two-fluid simulations and exploring various acceleration sites and diffusion coefficients, we derive the CR energy density profile and luminosity to best fit the γ-ray observations. We discover significant discrepancies between the inferred CR energy density profiles from γ-ray luminosity and mass observations and the true radial profile. CR acceleration occurring either at the cluster's core region or the wind termination shock can account for the observations, provided the diffusion coefficient is approximately $\kappa_{\rm cr} \sim 10^{27}$ cm^2 s^{-1} and around $10\% - 20\%$ of the shock power/post-shock pressure is allocated to the CR component. Additionally, we explore the possibility of discrete supernova (SN) explosions driving CR acceleration and find that with an injection rate of one SN occurring approximately every 0.03 Myr, the observed γ-ray profile can be explained. This multiple SN scenario remains consistent with X-ray observations only if the thermal conductivity closely resembles the Spitzer value.

Origin of cosmic rays between 'knee' and 'ankle'

Supernova shocks are thought to be responsible for accelerating lower-energy cosmic rays up to approximately 10^{5-6} GeV (Lagage & Cesarsky, 1983a; Axford, 1994) and the extra-galactic cosmic ray component dominates above $\sim 10^9$ GeV energy (Unger et al., 2015; di Matteo, 2015; Rachen, 2015). Therefore the origin of cosmic rays between $10^7 - 10^9$ GeV remains unexplained. We show that massive young star clusters present potential candidates for accelerating Galactic cosmic rays (CRs) in this range. Various conceivable scenarios, such as acceleration at the wind termination shock (WTS) and supernova shocks within these young star clusters, have been proposed. We develop a model for the generation of different nuclei in CRs from massive stellar winds utilizing the observed distribution of young star clusters in the Galactic plane. Our study encompasses a meticulous calculation of CR transport in the Galaxy, incorporating the effects of diffusion, interaction losses during propagation, and particle re-acceleration by aged supernova remnants to determine the all-particle CR spectrum. Utilizing the Hillas criterion's maximum energy estimate, we contend that a young massive star cluster can accelerate protons to several tens of PeV. When compared with observed data, our model necessitates a CR source spectrum featuring an exponential cutoff at $5 \times 10^7 Z$ GeV ($50 Z$ PeV) from these clusters, in conjunction with a cosmic-ray injection fraction of approximately 5% of the wind kinetic energy. We discuss the feasibility of meeting these criteria in star clusters, along with associated uncertainties, within the framework of considering star clusters as the inherent accelerators of the 'second component' of Galactic cosmic rays.

Observed spectral bump at TeV energy range

The presence of discrete nearby cosmic-ray sources can introduce interesting effects on the observed properties of cosmic rays. Recent observations from the DAMPE (An et al., 2019; Alemanno et al., 2021) and CALET (Adriani et al., 2022a, 2023) experiments have unveiled a distinct bump-like feature in the proton and helium spectra within the energy range of approximately $1-100$ TeV. Despite this observation, the origin of the feature remains unclear. In this study, we undertake an enhanced and more detailed analysis compared to previous works. This includes using the latest age and distance estimates of nearby supernova remnants, considering time-dependent escape mechanisms of cosmic rays, and so on. We demonstrate that the spectral bump can be attributed to the contribution of cosmic rays originating from nearby supernova remnants, particularly highlighting the role of the Vela remnant. Furthermore, we establish that the contribution from these nearby remnants aligns well with the observed spectra of heavier cosmic ray elements, ranging from carbon to iron when combined with the background flux of cosmic rays originating from distant supernova remnants. Our model remains consistent with the measured all-particle cosmic-ray spectrum up to approximately 10^{17} eV when augmented by an additional component of cosmic rays originating from young compact star clusters within our Galaxy.

List of Publications

1. **Bhadra, S.**, Gupta, S., Nath, B., Sharma P., *Cosmic rays from massive star clusters: a close look at Westerlund 1*, Monthly Notices of the Royal Astronomical Society, **510**, 5579, 2022.

2. **Bhadra, S.**, Thoudam, S., Nath, B., Sharma P., *Between the Cosmic-Ray 'Knee' and the 'Ankle': Contribution from Star Clusters*, The Astrophysical Journal, **961**, 215, 2024.

3. **Bhadra, S.**, Thoudam, S., Nath, B., Sharma P., *TeV spectral bump of cosmic-ray protons and helium nuclei: the role of nearby supernova remnants*, submitted in ApJ.

Table of contents

List of figures

List of tables

1

Thesis Objectives

1.1 Review of cosmic rays

Cosmic rays (CRs) are high-energy charged particles that travel through space at nearly the speed of light. They originate from various sources in our Galaxy as well as from distant galaxies. When these CRs collide with Earth's atmosphere, they generate cascades of secondary particles. Observationally it has been found that approximately 98% of the particles are protons, and heavier nuclei and the remaining $\sim 2\%$ are electrons (Longair, 1992). Figure 1.1 shows a holistic picture of the complete CR energy spectrum measured by different experiments. These particles have a wide range of energies from hundreds of MeV to $\sim 10^{11}$ GeV and the observed spectrum can be described by a power law distribution of kinetic energy $\sim E^{-2.7}$ up to $\sim 10^6$ GeV. There are however important features in the spectrum which include the 'knee' at $\sim 3 \times 10^6$ GeV where the slope changes from -2.7 to -3.1 and then again a flattening back to -2.7 at $\sim 4 \times 10^9$ GeV, which is known as the 'ankle'. However, it is evident that the overwhelming majority originate from beyond the solar system but these sources remain within our Galaxy. The most energetic CRs (beyond $\sim 10^9$ GeV) exhibit gyro-radii within typical galactic magnetic fields that surpass the Galaxy's dimensions, suggesting a potential extragalactic origin for these particles (Gaisser, 1990). Eventually, at $\sim 10^{11}$ GeV the CR

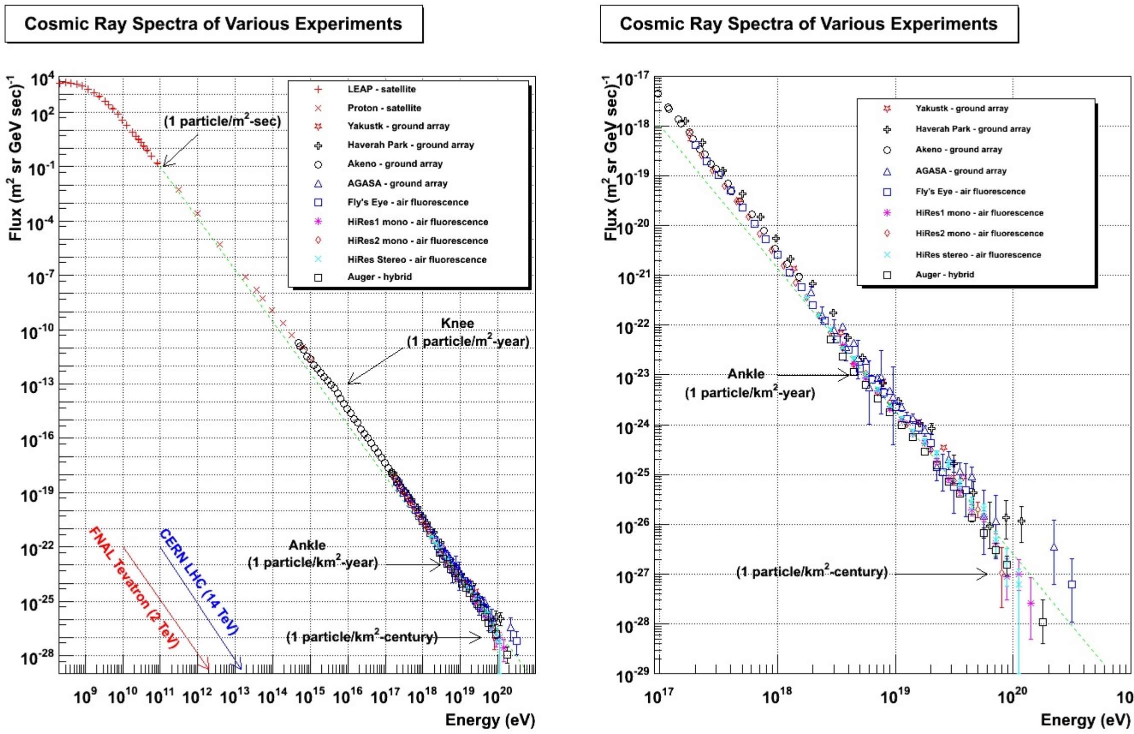

Fig. 1.1 The energy distribution of cosmic rays as observed across different experiments is depicted. Notable characteristics in the spectrum, such as the ‘knee’ around 10^6 GeV and the ‘ankle’ near 10^9 GeV, are highlighted. The occurrence rates of particles with varying energies are shown, alongside the energies achievable in diverse accelerator experiments. On the right, the same plot is presented, emphasizing the higher energy range exclusively, spanning from 10^{17} to 10^{21} eV (https://web.physics.utah.edu/ whanlon/spectrum.html).

spectrum is believed to terminate in the so-called Greisen-Zatsepin-Kuzmin (GZK) cutoff due to interaction with cosmic microwave background (CMB) photons (Greisen, 1966; Zatsepin & Kuz’min, 1966). Although this issue is not yet settled in light of recent claim from the Auger Collaboration. Their findings suggest complexities in interpreting cosmic ray energy spectra and composition. The Auger Collaboration has observed a suppression in the energy spectrum consistent with the GZK effect, but they emphasize that alternative explanations, such as local source limitations or heavier nuclei contributions, could also produce similar spectral features (Góra & Pierre Auger Collaboration, 2018).

1.1.1 The energy spectra of cosmic ray protons, nuclei & electrons

The energy distributions of CR nuclei show well-fitted power-law patterns, as depicted in Fig. 1.1. Figure 1.2 shows the differential energy spectra for various nuclei, including protons, helium, carbon, oxygen, iron, and other heavier nuclei, as a function of the kinetic energy per nucleon of the particles. At low energies, the flux is affected by the solar wind which decreases the flux of low energy particles. This phenomenon which is known as 'solar modulation', occurs because CR particles diffuse toward Earth from interstellar medium through the solar wind which is directed outward from the solar system. The increase in solar activity results in greater disturbances in the interplanetary magnetic field, which hinder the propagation of particles with energies below approximately 1 GeV per nucleon towards Earth (Gleeson & Axford, 1968). The differential energy spectra of the different CR nuclei can be described well by power-law distributions of kinetic energy of the form $N(E)dE = \kappa E^{-\gamma} dE$ with $\gamma = 2.7$ in the energy range $1 < E < 10^6$ GeV. The approximate intensity of primary CR nucleons within the energy range from several GeV to slightly above 100 TeV can be written as (Longair, 1992),

$$I_N(E) \sim 1.8 \times 10^4 \, E^{-2.7} \text{ nucleons m}^{-2}\,\text{s}^{-1}\,\text{sr}^{-1}\,\text{GeV}^{-1}\,, \tag{1.1}$$

where E is the energy per nucleon in GeV. Notable differences, however, exist in the energy spectra among various elements (see fig 1.2). Generally, it has been observed that the primary CR species (those which are accelerated within sources) tend to exhibit somewhat flatter spectra when compared to secondary species. These secondary species are predominantly formed through nuclear collisions between primary species and interstellar gas nuclei or molecules during the propagation of CR primary particles through the interstellar medium (ISM). This process is referred to as 'spallation'. The measured spectra of different primaries can also be slightly different (as can be seen in Figure 1.2), due to various propagation effects.

On the other hand, the energy spectrum of CR electrons is slightly different from the CR nuclei. CR electron spectra have been assessed using data gathered from both ground-based experiments and experiments using space-based satellites. Figure 1.3 shows the differential spectra of CR electrons as a function of energy. The vertical axis is shown in terms of $E^3 N(E)$ so that the power law distribution of electrons $N(E) \sim E^{-3}$ would represent a parallel line to the x-axis. It is clear that the electron spectrum is somewhat steeper than that of CR protons and nuclei. This is because electrons are significantly affected by various energy loss mechanisms, such as synchrotron radiation and other similar processes. Therefore, they must come from a few nearby sources (Aharonian et al., 1995; Kobayashi et al., 2004). The electron spectrum is significantly impacted by solar modulation effects for energies below ~ 1 GeV. However, for particles with energies ≥ 10 GeV, observations are less affected by these effects. The energy density of CR electrons is found to be ~ 0.01 of the total CR energy density (Amsler et al., 2008). This value has some uncertainty. From observations in the solar system, at CR energy ~ 10 GeV, where solar modulation effects are low, the ratio of CR electron to proton energy is known to be 1% (Longair 1992, section 15.1). For energies ≥ 10 GeV (where solar modulation can be neglected), the observations can be characterized by a power-law spectrum as described

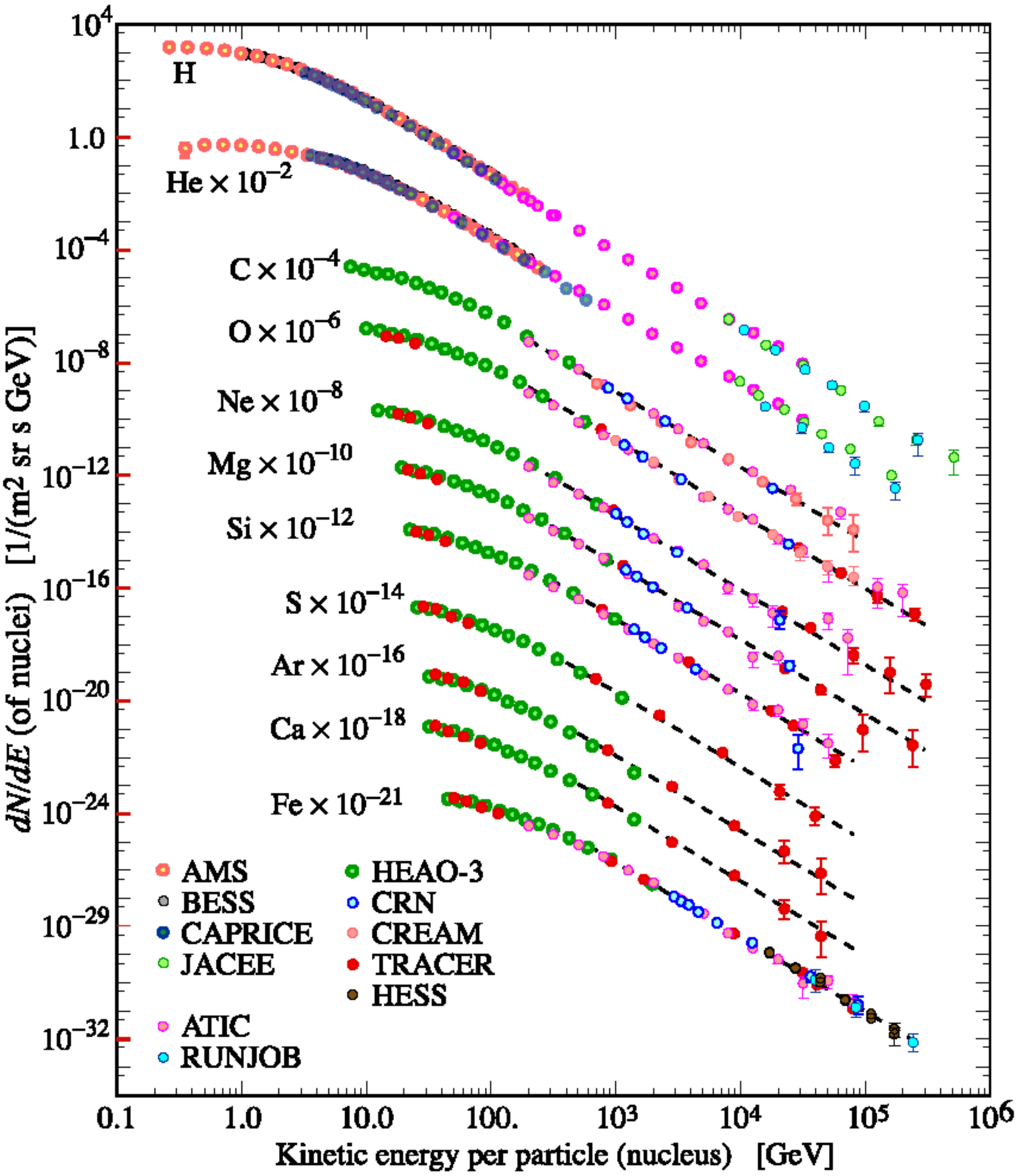

Fig. 1.2 The differential energy spectrum of different Cosmic rays elements measured by different experiments over a large energy range, from Beringer et al. (2012). Note that these data refer to the total energy per particle rather than the energy per nucleon.

by Webber (1983),

$$N(E)\,dE = 700\,E^{-3.3}\,dE \text{ particles m}^{-2}\,\text{s}^{-1}\,\text{sr}^{-1}, \tag{1.2}$$

where particle energy is measured in GeV. Comparing equations 1.1 and 1.2 one can see that the electron spectrum is steeper than the CR proton and nuclei spectrum.

1.1.2 Elemental abundances of cosmic rays

As we previously discussed, CRs consist of various elements, including protons, helium, and other heavier elements. The chemical abundances of CRs provide important clues to their origin, types (primaries or secondaries), and the processes of propagation from their sources to the Earth. A comprehensive summary of data on the chemical abundances in CRs has been provided by Simpson 1983; Lund 1984. A substantial portion of the highest-quality data was previously gathered through the experiments during the HEAO-C2 mission, along with balloon experiments that utilized extensive detector packages at high altitudes. Recently AMS, AMS-02, ATIC, CREAM, PAMELA, etc experiments have provided with high-quality data on different CR elements (Maurin et al., 2014). The cosmic abundances of the elements in CRs (black line) compared with the Solar System abundances (blue line) and shown in figure 1.4. Some of the important features are mentioned below:

(1) Except for hydrogen and helium, the abundance peaks at heavier elements such as carbon, nitrogen, oxygen, and the iron group nuclei. (2) The light elements, such as lithium, beryllium, and boron, exhibit significantly higher abundances in CRs compared to their abundances within the Solar System. These elements are essentially absent as end products of stellar nucleosynthesis. They are nevertheless present in cosmic radiation as spallation products (i.e. secondary particles) of the abundant nuclei of carbon and oxygen. (3) There is an excess abundance in the CRs of elements with atomic and mass numbers just less than those of iron, that is, elements between calcium and iron. These are (Sc, Ti, V, Cr, Mn) the spallation products of Iron. (4) There is an underabundance of hydrogen and helium in the CRs relative to the heavy elements. (5) The odd-even effect, which reflects the varying stabilities of nuclei based on atomic number and is observed in Solar System abundances of elements, is similarly evident in CRs, albeit to a slightly lesser extent.

In general, the distribution of elemental abundances in CRs closely resembles typical solar system abundances. However, some of the variances noted earlier can be attributed to spallation occurring in the interstellar medium during their propagation. Due to collisions, heavier CR nuclei are fragmented, and this results in the production of nuclei with atomic and mass numbers less than those of the primary nuclei, which we call ‘secondary’ CRs. Note

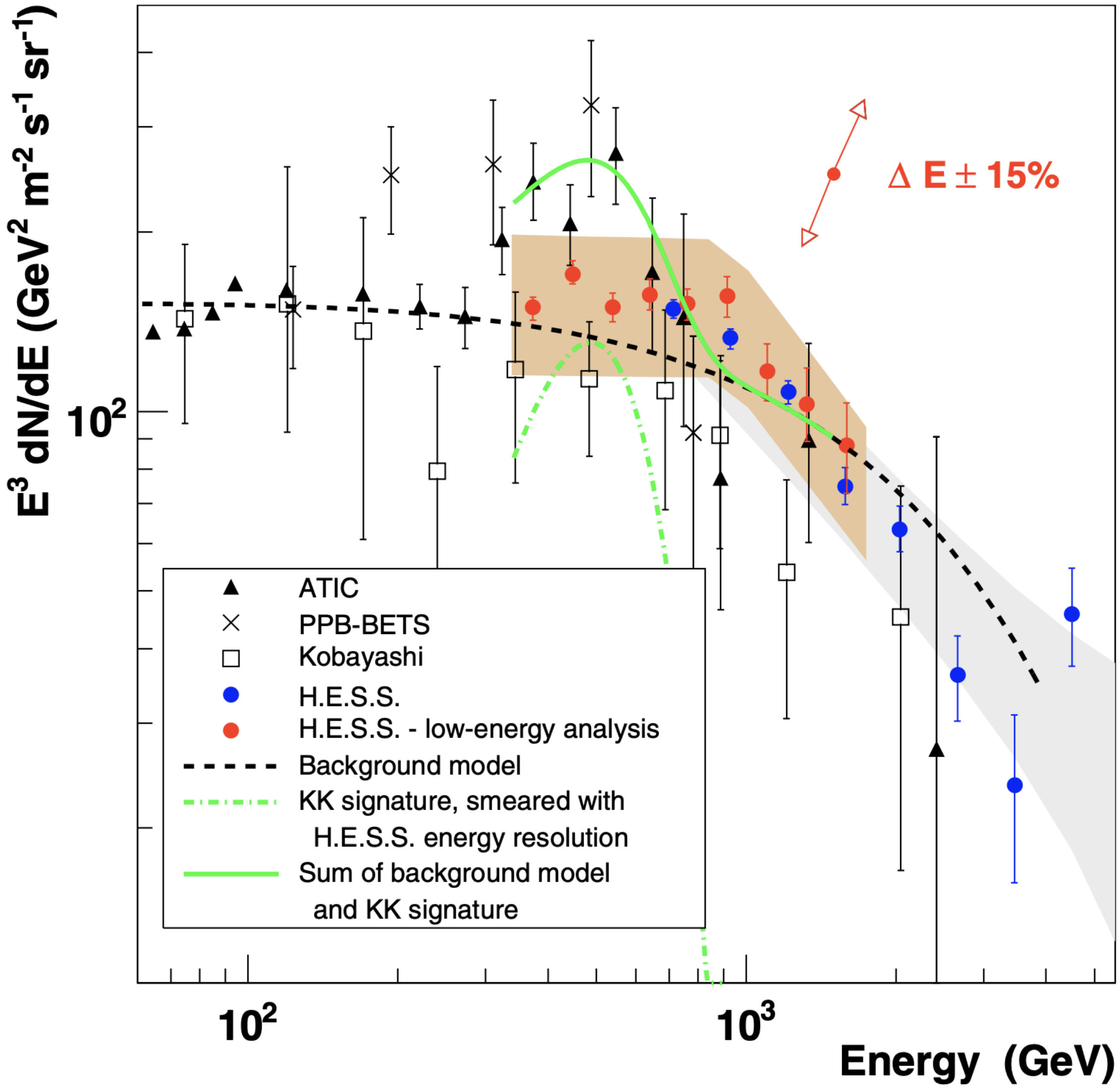

Fig. 1.3 The energy spectrum $E^3 dN/dE$ of cosmic-ray electrons as measured by ATIC, PPB-BETS, emulsion chamber experiments, FERMI (the gray band shows the FERMI systematic uncertainty, the double arrow labeled with $^{+5\%}_{-10\%}$ the uncertainty of the FERMI energy scale) and H.E.S.S. Previous H.E.S.S. data are shown as blue points, and the result of the low-energy analysis is presented as red points (Aharonian et al., 2009).

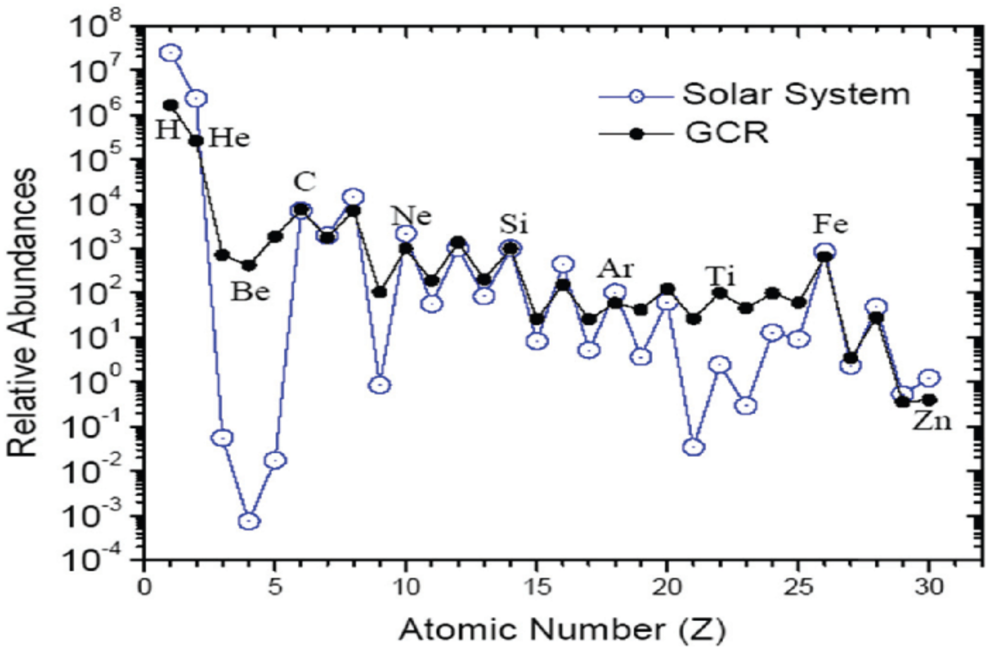

Fig. 1.4 The cosmic abundances of the elements in the cosmic rays (black line) compared with the Solar System abundances (blue line) (Alessandra, 2017).

the implication that secondaries such as photons, neutrinos, and antiprotons should also be produced at a certain rate as CRs propagate through the ISM. In addition to these species, a small percentage of CR electrons also exists.

From a knowledge of the cross sections for spallation, one can learn something about the amount of matter traversed by CRs between production and observation. For the bulk of the CRs, the mean amount of matter traversed is of order X = 5 to 10 g/cm^2 (Gaisser, 1990). The number density n in the disk of the Galaxy is of order 1 proton per cm^3, so this thickness of material corresponds to a distance of.

$$l = X/(m_p n) = 3 \times 10^{24}\,\mathrm{cm} \sim 1000\,\mathrm{kpc}\,. \tag{1.3}$$

As CRs potentially traverse the less dense regions of the galactic halo, this serves as a minimum estimate for their traveled distance. As l is significantly greater than $d \sim 0.1$ kpc, the half-thickness of the Galaxy's disk, suggests that CR confinement involves a diffusive process, wherein particles meander for extended periods before eventually venturing into intergalactic space (Gaisser, 1990).

1.2 Acceleration of cosmic rays

There are several potential sites for CR acceleration, with supernova shock waves being the most significant. At the end of their life cycle, massive stars ($\geq 8M_\odot$) undergo supernova explosions (SNR). As the material expelled from the exploded star collides with the Interstellar Medium (ISM), it generates shock waves, which is a surface of discontinuity moving through the ISM faster than the sound speed upstream (ISM). These shock waves sweep up interstellar matter with themselves while propagating. They are believed to be the sites where particles are accelerated to high energies, thereby producing CRs. Before delving into the role of SNR shocks in CR acceleration, we will first explore the original concept of Fermi's second-order acceleration.

1.2.1 Fermi second-order acceleration

According to Fermi's initial concept, charged particles can be reflected/scattered from 'magnetic mirrors' which are produced by irregularities within the Galactic magnetic field (Fermi, 1949). Massive interstellar clouds act as these types of mirrors. These mirrors (i.e. clouds) are assumed to move randomly with an average velocity denoted as V. Fermi demonstrated that particles gain energy through stochastic processes during their reflections from these clouds.

Let us briefly revisit Fermi's calculation for particle acceleration. Consider the collision between the particle and the mirror occurs with an angle θ. Here θ is the angle between the initial direction of the particle and the normal to the surface of the mirror i.e. the cloud. For the sake of simplicity, let us also consider that the cloud is infinitely massive and the velocity of the cloud after the collision remains unchanged (Longair, 1992). Under these assumptions, the center of momentum frame of reference is defined by the cloud moving at a velocity V along the x direction, while the particle moves with velocity υ (see the right panel of figure 1.5). In this frame, the energy gain of the particle is

$$E' = \gamma_V (E + Vp\cos\theta), \quad \text{where } \gamma_V = (1 - V^2/c^2)^{-1/2} \ . \tag{1.4}$$

The x-component of the momentum can be expressed as,

$$p'_x = \gamma_V \left(p\cos\theta + \frac{VE}{c^2} \right) . \tag{1.5}$$

In the collision, the particle energy remains conserved, and the momentum in the x direction

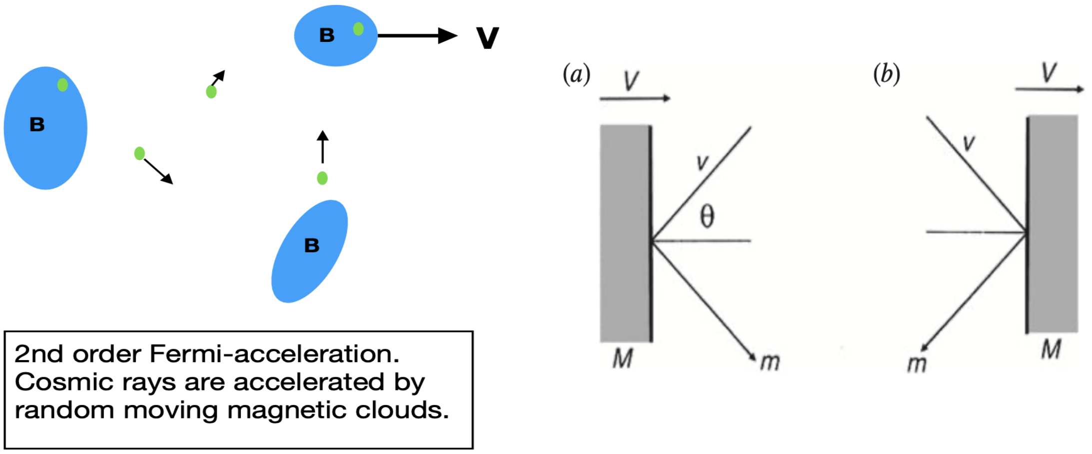

Fig. 1.5 Left: Illustration of 2nd and 1st order Fermi-acceleration in the astrophysical scenario; Right: Illustrating the collision between a particle of mass m and a cloud of mass M: (a) a head-on collision; (b) a following collision.

gets reversed i.e. $p'_x \to -p'_x$. Transforming back to the observer frame we can express,

$$E'' = \gamma_V (E' + V p'_x)\,. \tag{1.6}$$

If we substitute equations 1.4 and 1.5 into 1.6 we get the energy of the particle,

$$E'' = \gamma_V^2 E \left[1 + \frac{2V \upsilon \cos\theta}{c^2} + \left(\frac{V}{c}\right)^2 \right]. \tag{1.7}$$

We can expand it to the second order and get the expression for the energy gained by the particle,

$$\Delta E = E'' - E = E \left[\frac{2V \upsilon \cos\theta}{c^2} + 2\left(\frac{V}{c}\right)^2 \right]. \tag{1.8}$$

One can, therefore work out the mean increase in energy by averaging over a random distribution of angles θ. The probabilities of head-on and following/tail-on collisions are proportional to the relative velocities of the approach of the particle and the cloud, namely, $(\upsilon + V\cos\theta)$ and $(\upsilon - V\cos\theta)$ respectively. Since $\upsilon \sim c$ for the particles, the probabilities are proportional to $1 + (V/c)\cos\theta$ where $0 < \theta < \pi$. Therefore, there is a slightly greater probability of head-on encounters (when $0 \leq \theta \leq \pi/2$) as opposed to following collisions (when $\pi/2 \leq \theta \leq \pi$). Recalling that the probability of the angle lying in the angular range θ to $\theta + d\theta$ is proportional to $\sin\theta\, d\theta$, and averaging over all angles in the range 0 to π, the first term in 1.8 in the limit

$\upsilon \to c$ becomes (Longair, 1992),

$$\left\langle \frac{\Delta E}{E} \right\rangle = \left(\frac{V}{c} \right) \frac{\int_{-1}^{1} x[1+(V/c)x]\,dx}{\int_{-1}^{1} [1+(V/c)x]\,dx} = \frac{2}{3}\frac{V^2}{c^2}, \tag{1.9}$$

where $x = \cos\theta$. After adding the last term in equation 1.8 with this term the total energy gain can be written as,

$$\left\langle \frac{\Delta E}{E} \right\rangle = \frac{8}{3} \left(\frac{V}{c} \right)^2 . \tag{1.10}$$

So, the energy gain in this mechanism is second order in V/c. This results in an exponential growth in the particle's energy, as the same fractional increase takes place per collision. There were, however, problems with this picture. The random velocities of interstellar clouds within the Galaxy are extremely small compared to the speed of light, with $V/c \leq 10^{-4}$. Moreover, the mean free path for CRs scattering in the interstellar medium is approximately 0.1 parsec (Longair, 1992), resulting in only a few collisions per year and thus a slow energy gain for the particles. A more promising approach might involve focusing on regions with small-scale turbulence, such as the shells of young supernova remnants, where significant small-scale structure exists and velocities are much higher than in the broader interstellar medium.

1.2.2 Acceleration of CRs in supernova shocks (DSA)

Since the late 1970s, a prevalent acceleration mechanism in astrophysical scenarios has been linked to the acceleration of particles around strong shock waves, commonly known as diffusive shock acceleration (Axford et al., 1977; Bell, 1978; Blandford & Ostriker, 1978). These shocks are predominantly collisionless, meaning that the transfer of momentum between the shocked material and the newly accumulated material occurs via the magnetic field, rather than through direct particle collisions. The magnetic field in the ambient ISM is compressed around the shock, and small-scale magnetic fluctuations of substantial strength can be created around the shock. Magnetic fluctuations can also be created due to the streaming instabilities, or turbulent motion on either side of the shock wave. These magnetic fluctuations act as 'magnetic mirrors' which can reflect high-energy particles. Let us examine a strong SNR shock moving at a velocity denoted as U through the interstellar medium, and how it interacts with relativistic particles within a specific region. These particles, which possess energy $E(\sim pc)$, remain unaffected by the shock's discontinuity but instead scatter off the magnetic irregularities present on both sides of the shock (Longair, 1992).

Let us briefly discuss the DSA mechanism around a shock. The model considers a strong shock (i.e. having a high Mach number) propagating through a diffuse medium, such as the shock waves that propagate through the interstellar medium (ISM) ahead of the supersonic shells of supernova remnants. During their propagation, these shocks interact with the ISM particles that are ahead of them, in other words, this ISM particles are accelerated up to high energy. It is often convenient to switch to a frame of reference where the shock front is stationary. In this frame, the upstream gas flows into the shock front at velocity $\upsilon_1 = U$ and exits with a downstream velocity υ_2. The continuity equation requires that mass is conserved through the shock, hence

$$\rho_1 \upsilon_1 = \rho_2 \upsilon_2 \,. \tag{1.11}$$

If the shock is strong enough the matter density ratio in the two sides of the shock can be expressed as,

$$\frac{\upsilon_1}{\upsilon_2} = \frac{\rho_2}{\rho_1} = \frac{\gamma+1}{\gamma-1}, \tag{1.12}$$

where $\gamma = 5/3$ for monoatomic gas, which gives $\rho_2/\rho_1 = 4$ and so $\upsilon_1/\upsilon_2 = 4$ (using the mass conservation law). Now, let us consider those high-energy particles which are ahead of the shock. Through random scattering, the particle distribution becomes isotropic within the frame of reference where the gas is stationary. The shock propagates through the medium at velocity U, while the gas behind the shock moves at a velocity of $(3/4)U$ relative to the upstream gas. In other words, the particle in the upstream will see the downstream moving towards it with a velocity of $(3/4)U$ which indicates a head-on collision. When a high-energy particle crosses the shock front, it gains a small increase in energy $\Delta E \sim U/c$. Subsequently, the particles are scattered in the region behind the shock front, causing their velocity distributions to become isotropic with respect to that flow.

Consider the reverse process where a particle moves from behind the shock to the upstream region in front of the shock. Behind the shock, the particle distribution is isotropic, and upon crossing the shock front, the particle encounters gas moving towards the shock front at the same velocity $(3/4)U$. Similar to the previous case the downstream particle will see the upstream coming towards it with a velocity of $(3/4)U$ which indicates again a head-on collision. In other words, the particle undergoes exactly the same process of receiving a small increase in energy ΔE on crossing the shock from the downstream to the upstream flow as it did in traveling from upstream to downstream. Each time the particle crosses the shock front, it gains energy, there are no instances where the particle loses energy and the energy increment is identical in both directions. This is a significant improvement from Fermi's original mechanism where there were both head-on and following collisions, however, in the case of acceleration at shock front, the collisions are always head-on collision.

The gas on the downstream side approaches the particle at a velocity $V = (3/4)U$. If the particle has energy E in the local rest frame before shock crossing, the energy in the frame of

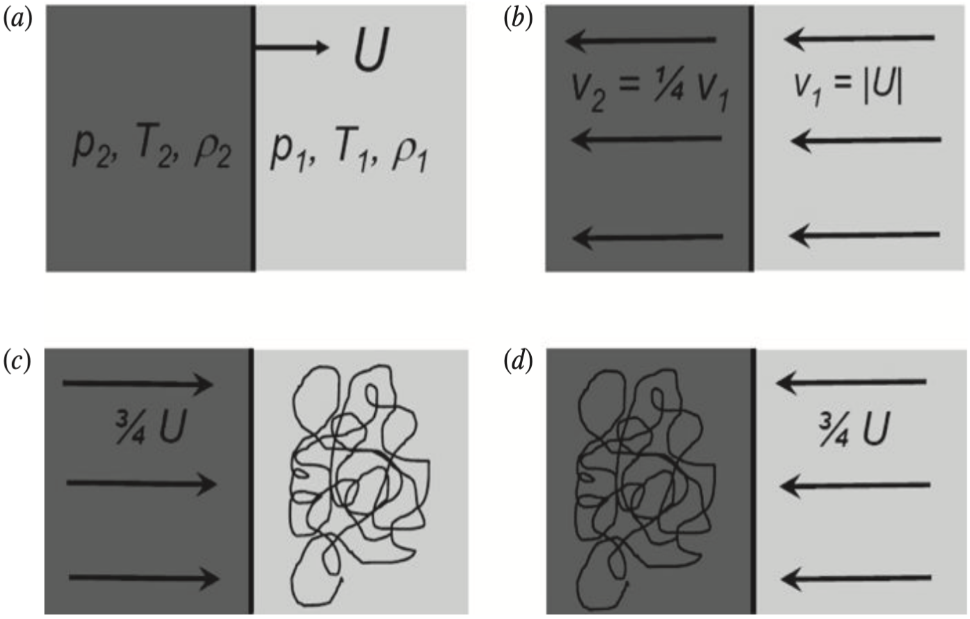

Fig. 1.6 Back-and-forth scattering of particles around a shock. (a) A strong shock wave propagating at a supersonic velocity U through stationary interstellar gas. The upstream density ρ_1, pressure p_1, and temperature T_1. The density, pressure, and temperature downstream are ρ_2, p_2, and T_2, respectively, (b) The flow of interstellar gas in the vicinity of the shock front in the reference frame in which the shock front is at rest, (c)The flow of gas as observed in the frame of reference in which the upstream gas is stationary, (d) The flow of gas as observed in the frame of reference in which the downstream gas is stationary (Longair, 1992).

the medium encountered after shock crossing is,

$$E' = \gamma_V (E + V p_x)\,, \tag{1.13}$$

where p_x is the x-component of the momentum and the x-axis is chosen to be along V. Note that, γ_V is close to unity, if the shock is non-relativistic, as the SN shocks usually are. Since $p_x = p\cos\theta = E\cos\theta/c$, the energy gain in each shock crossing is,

$$\Delta E = E' - E = E\left(\frac{V}{c}\right)\cos\theta\,. \tag{1.14}$$

Suppose the fractional change in the energy at each crossing is η. Note, that this is an improvement over the second-order acceleration where the energy gain was proportional to $(V/c)^2$. After n crossings, a particle with initial energy E_0 will have energy $E = E_0(1+\eta)^n$. The particles will not continue to cross the shock indefinitely. The net momentum flux of the shocked gas (downstream) will carry them away in due course. Suppose the probability of remaining in the shock-crossing region after each crossing is P. Then after n crossings, there will be $N = N_0 P^n$ of the original N_0 particles left. Eliminating n we have,

$$\frac{ln(N/N_0)}{ln(E/E_0} = \frac{lnP}{ln(1+\eta)} \Rightarrow \frac{N}{N_0} = \left(\frac{E}{E_0}\right)^{\frac{lnP}{(1+\eta)}}\,. \tag{1.15}$$

For each crossing, the energy gain is $\Delta E/E = (V/c)\cos\theta$. If the flux of particles arriving at angle θ is proportional to $(c\cos\theta)(\sin\theta\, d\theta)$, then one can find a flux-weighted fractional energy gain per shock crossing as,

$$\left\langle\frac{\Delta E}{E}\right\rangle = \frac{V}{c}\frac{\int_0^{\pi/2}\cos^2\theta\sin\theta\, d\theta}{\int_0^{\pi/2}\cos\theta\sin\theta\, d\theta} = \frac{2V}{3c}\,. \tag{1.16}$$

Therefore the energy gain per cycle of crossing back and forth is

$$\eta = \left\langle\frac{\Delta E}{E}\right\rangle_{\text{cycle}} = \frac{4V}{3c}\,. \tag{1.17}$$

Since $V << c$,

$$\ln(1+\eta) = \ln\left(1+\frac{4V}{3c}\right) \sim \frac{4V}{3c} = \frac{U}{c}\,. \tag{1.18}$$

Not all particles that cross into the downstream (shocked) region will come back upstream since the downstream (shocked) medium is moving away from the shock front at a speed $\upsilon_2 = U/4$. Since the average speed of the particles is close to c, the flux of particles crossing into the downstream region is,

$$\frac{1}{2}\int_0^1 d\mu\, n c \mu = \frac{nc}{4}, \tag{1.19}$$

where n is the number density of particles and $\mu = \cos\theta$. In the downstream region, the particles are carried away from the shock front with a flux $n\upsilon_2$. So the probability of a particle escaping the acceleration zone in a cycle is,

$$P_{\text{esc}} = \frac{n\upsilon_2}{nc/4} = \frac{U}{c} \tag{1.20}$$

In other words, the probability of remaining in the shocked region is,

$$P = 1 - P_{\text{esc}} = 1 - \frac{U}{c} \Rightarrow \ln P \sim -\frac{U}{c}. \tag{1.21}$$

Therefore we can write $\frac{\ln P}{\ln(1+\eta)} = -1$. This gives the power law index of CR energy as -2. If we take the differential form of equation 1.5 we can write,

$$N(E, E+dE) = \text{Constant} \times E^{-1+\frac{\ln P}{(1+\eta)}} \propto E^{-2} \tag{1.22}$$

A quick estimate supports this idea of particle acceleration around SNR shocks: the total energy density of CRs in the ISM amounts to about 1 eV cm^{-3}. The total kinetic energy in an SN shock wave is $\sim 10^{51}$ erg. Typically we have about an SN going off in half a century in the Milky Way (Diehl et al., 2006). If we take a typical lifetime of an SNR as $\sim 10^4$ yr, at any time about 200 SN remnants are accelerating CRs. And the efficiency of CR acceleration is about 10%. And the relevant volume is that of a cylinder with 10 kpc radius and 100 pc height, so 10^{65} cc. Hence, if we divide the total energy in CRs by the total volume of our Galaxy we get an estimation of CR energy density in our Galaxy. This gives an energy density that is similar to that of observed CRs of 1 eV/cc. This simple benchmark estimate supports the idea of DSA around shocks.

1.2.3 Maximum energy gain in cosmic ray acceleration in SNR shocks

We have already observed in the previous section that particles undergo acceleration around a supernova shock. As a particle completes successive cycles around the shock, it accumulates energy, with significant gains occurring after numerous crossings. The Larmor radius of an accelerated particle increases proportionally with its energy; in other words, higher particle energies result in larger Larmor radii. When a particle reaches an energy level where its corresponding Larmor radius exceeds the confinement of the acceleration region, it exits and travels through the interstellar medium (ISM). This concept termed the *'confinement criterion'*, provides insight into the maximum attainable energy for accelerated particles around a strong shock. The Hillas criterion (Hillas, 1984) is formulated based on this confinement criterion: $E_{\max} = ZeBR$ (B is the magnetic field, R is the shock radius, Ze charge of the particle), i.e. particles with Larmor radii larger than the size of the accelerating region escape. This is the least stringent constraint one can put on the maximum energy and it does not give any clue about the underlying acceleration mechanism. As particles are accelerated in electric fields (or equivalently the motion of scattering centers), considering a specific acceleration mechanism introduces a factor u/c in the above estimate, where u is some characteristic velocity specific to the acceleration mechanism under investigation (for acceleration at shock u is the velocity of the SNR shock). The maximum energy is then achieved in the electric potential $\phi = BRu/c$ such that $E_{\max} = zeBRu/c$.

Another criterion for maximum energy gain can be determined based on the available particle acceleration time in SNR shocks. This is a more stringent condition for the maximum energy of particle acceleration especially for the SNR shock. When a shock remains strong for the initial time period and with time it becomes weaker (such as SNR shocks), in this scenario, calculating the maximum energy gain using the available acceleration time is more favorable. Lagage & Cesarsky (1983a) describes in detail this process which can limit the acceleration process. The fundamental issue lies in the fact that the diffusion acceleration mechanism remains a relatively slow process. Particles must undergo numerous crossings back and forth across the shock wave. In this context of supernova remnant shells, if we take a typical shock speed of $V = 3000$ km/s, the particle energy increases $\Delta E/E \sim V/c$, which is approximately one part in 100 (because $V/c = 3 \times 10^6/3 \times 10^8 = 0.01$). Once the remnant has gathered roughly its own mass of interstellar gas, the supernova blast wave undergoes deceleration, transitioning into the Sedov phase of evolution. While the acceleration mechanism persists throughout the lifespan of a supernova remnant until its integration into the interstellar medium, typically occurring over about $10^5 - 10^6$ years, the majority of particle acceleration takes place during the un-decelerated blast wave phase when the shock remains strong (i.e the Mach number of the shock is high). This phase typically lasts less than approximately 10^3 years, as demonstrated by the calculations conducted by (Lagage & Cesarsky, 1983a).

If the diffusion coefficient of the particles is D_i (i=1,2 for upstream and downstream of the shock, respectively), the gas velocity in the shock frame is u_i (i=1,2 for upstream and downstream of the shock, respectively), and the particle velocity is υ, the average time taken by the particles to cycle through the shock is,

$$T_{\text{cycle}} = \frac{4}{\upsilon}\left(\frac{D_1}{u_1} + \frac{D_2}{u_2}\right). \tag{1.23}$$

This is derived by solving the cosmic ray transport equation or using the solution of the analogous random walk problem. Then the momentum gain by the particles can be approximated as (Lagage & Cesarsky, 1983a),

$$\frac{dp}{dt} \sim \frac{\Delta p}{T_{\rm cycle}} = \frac{u_1 - u_2}{3} \frac{p}{\frac{D_1}{u_1} + \frac{D_2}{u_2}} . \tag{1.24}$$

This solution is obtained by solving the transport equation with cosmic ray particle distribution function (for details, please see equation 3 in Lagage & Cesarsky 1983a). Integrating the above equation one can get p as a function of time (t). It is easy to integrate equation 1.24, one obtains the momentum change at the end of the blast phase,

$$p(t) = 10^5 \, \frac{ZB_{-6}E_{51}}{\frac{n_e}{3\times 10^3\,{\rm cm}^{-3}} M_{\rm ej}} \, {\rm Gev/c} . \tag{1.25}$$

Where Z is the proton number of the cosmic rap nuclei, B_{-6} is the magnetic field in the unit of μG, $M_{\rm ej}$ is the mass of the SNR ejecta in the unit of solar mass, E_{51} is the energy of explosion in the unit of 10^{51} erg/s. The maximum energy attained at the need of the blast phase is (for details see Lagage & Cesarsky (1983a), section IV),

$$E_{\rm max} = cp_{\rm max} \sim 10^5 ZB_{-6} \ {\rm GeV} . \tag{1.26}$$

This maximum energy that can be accelerated in strong SNR shocks is well below the highest energy particles detected on earth which is $\sim 10^{11-12}$ GeV.

1.2.4 Observation of SNRs as particle accelerators

In previous sections, theoretically, we have seen how the SNR shocks can act as particle accelerators, However, this idea needs to be supported by observational evidence. Observations of supernova remnants through radio and gamma-ray channels offer compelling proof that they serve as origins for high-energy particles.

Radio observations: The shell-like remnants of various supernovae have been observed in the radio, optical, and X-ray wavebands. The X-ray emissions result from the bremsstrahlung radiation which is produced by the supernova blast wave heating interstellar material to extremely high temperatures, whereas the optical and infrared emissions observed from the supernova remnants originate from hot gas and dust. On the other hand, radio emission, which exhibits a power-law energy spectrum, is caused by synchrotron radiation originating from ultra-relativistic electrons accelerated within the shock waves linked to the blast waves. These

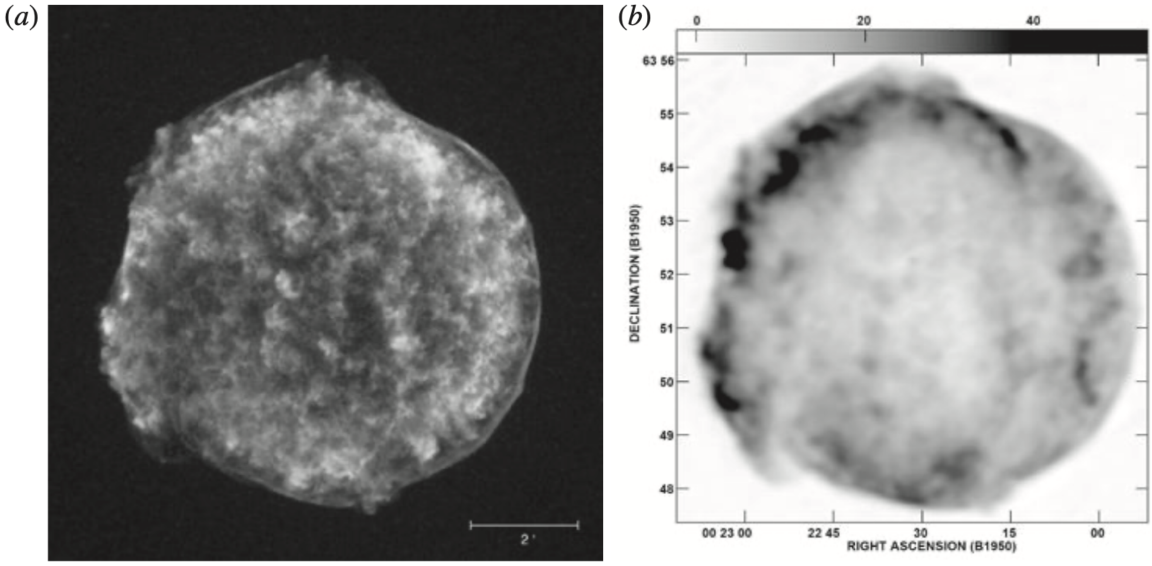

Fig. 1.7 (a) A composite image of Tycho Brahe's 1572 supernova, created from observations by the Calar Alto telescope, the Chandra X-ray Observatory, and the Spitzer Space Infrared Observatory (courtesy of NASA and the Space Telescope Science Institute). (b) A radio image of Tycho Brahe's supernova at 1.4 GHz, captured by the VLA (Katz-Stone et al., 2000).

features are illustrated by the spectacular high-resolution images of the supernova remnant Tycho's supernova in the optical, infrared, X-ray, and radio wavebands (shown in figure 1.7).

The notable aspect is the close alignment between the relativistic particles and magnetic fields accountable for radio emission and the characteristics observed in the optical, infrared, and X-ray wavelengths. This alignment is linked to the existence of powerful shocks, which compress the gas, dust, and magnetic fields and simultaneously facilitate the primary acceleration of energetic electrons to high energies. Another instance of a young shell-like supernova is the Cassiopeia A supernova, which also exhibits a shell-like structure with a distinct, nearly circular perimeter. Again there's a notable alignment between the thermal material (X-ray emission) and the synchrotron radio emission produced by ultra-relativistic electrons. Regarding the aged supernova remnant, the Cygnus Loop, approximately 5000 years old, there is a strong correlation between areas exhibiting heightened radio emissivity and the existence of optical emission lines. Hence, radio emission indicates accelerated electrons, and those SNRs that are bright in radio, we identify as leptonic accelerators.

γ-ray observations: γ-rays are the most important indirect probe of high energy CR particles. Substantial proof of particles with CR energies within supernova remnants has been furnished through the impressive γ-ray image captured by imaging atmospheric Cherenkov γ-ray telescopes like the HESS array. A few examples of recent SNR observations by HESS in γ-rays have been shown in figure 1.8, where the close correlation of X-ray emission and γ-ray emission can be found. The γ-rays can be produced from the interaction of high-energy protons with the ISM particles and the inverse Compton effect of high-energy electrons. In their work, Aharonian et al. (2007) extensively examine the γ-ray emission from RX J0852.0–4622, proposing potential sources such as inverse Compton scattering of background photons by high-energy electrons, or the decay of neutral pions generated from p-p interactions involving high-energy protons and the thermal matter within the supernova shell. The X-ray emission originates from hot plasma downstream of the strong forward shock i.e. around the shell of the remnant. Observationally the γ-ray has been detected from a similar region of X-ray emission which indicates that the particle acceleration is also happening at the same place i.e around the shocks. Hence, in figure 1.8, the close correlation of γ-ray observations with the X-ray observation from remnant shells indicates that particles (mainly protons) are getting accelerated around the shocks and we identify these SNRs as hadronic accelerators. The observed γ -rays spectrum for these two remnants extends to energies greater than 100 TeV, providing direct evidence for the presence of high-energy particles with at least this energy in these objects. These observations align entirely with the dominant perspective, suggesting that high-energy particles, reaching energies of 100 TeV, can undergo first-order Fermi acceleration when encountering powerful shock waves (as discussed in section 1.2.3).

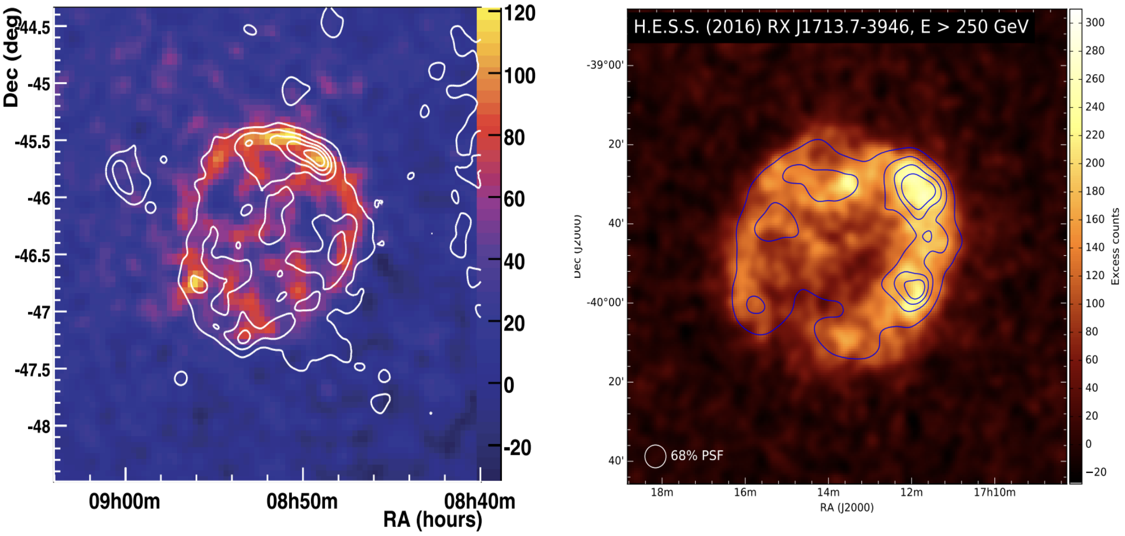

Fig. 1.8 Left: H.E.S.S. observations of the ultra-high energy γ-rays from the shell-type supernova remnant RX J0852.0-4622. Superimposed on the γ-ray image are contours of the X-ray emission at energies $E \geq 1.3$ keV from the ROSAT All-Sky Survey (Aharonian et al., 2007); Right: H.E.S.S. γ-ray excess image of RX J1713.7-3946 with overlaid XMM-Newton contours $(1-10$ keV) (H. E. S. S. Collaboration et al., 2018b).

1.2.5 Gamma rays as an indirect probe of cosmic rays

As mentioned at the beginning, approximately 98% of CRs consist predominantly of protons and heavier nuclei, highlighting the paramount importance of detecting these particles. Observations of γ-rays from potential CR accelerators can provide valuable insights into these particles. After getting accelerated in the source CRs propagate through ISM. During their propagation, CR particles interact with ISM particles and create pions ($\pi^{\pm}, \pi^0$), and each π^0 decays into two γ-rays. This channel of γ-ray production is called the hadronic. The corresponding reaction can be expressed as follows,

$$p + p \to p + p + \pi^0, \quad \pi^0 \to \gamma + \gamma. \tag{1.27}$$

Therefore, the observation of γ-ray photons provides insights into the spatial distribution of CR protons. Approximately 0.17% of a proton's kinetic energy is transferred to pions. At high energies, the γ-ray spectrum mimics the CR spectrum, with an approximate relation of $E_\gamma \approx \frac{E_{\rm CR}}{10}$. Using the methodology described in Dermer's model (Dermer 1986; Pfrommer & Enßlin 2004), one can estimate the γ-ray luminosity resulting from hadronic interactions (i.e., interactions between CR protons and interstellar medium protons). This model provides the luminosity between the energies $E_{\gamma 1}$ and $E_{\gamma 2}$:

$$L_\gamma^H = \int_V dV \int_{E_{\gamma 1}}^{E_{\gamma 2}} dE_\gamma E_\gamma \, q_\gamma(n_N, e_{\rm cr}, E_\gamma) \tag{1.28}$$

Here, $q_\gamma = dN/(dt\, dV\, dE_\gamma)$ is the number of γ-ray photons emitted per unit volume per unit time per unit energy, which is proportional to the number density of target nucleon (n_N) and the CR energy density ($e_{\rm cr}$). One can obtain the γ-ray luminosity in $(0.1 - 100)$ GeV band (Gupta et al., 2020):

$$L_\gamma^H = 10^{-16} \left(\frac{\Delta V}{\rm cm^3}\right) \left(\frac{n_N}{\rm cm^{-3}}\right) \left(\frac{e_{\rm cr}}{\rm erg\, cm^{-3}}\right) \ {\rm erg\, s^{-1}}. \tag{1.29}$$

Clearly, γ-rays luminosity due to hadronic origin (L_γ^H) is proportional to the target nucleon (n_N), the volume of the emitting region (ΔV), and the CR energy density ($e_{\rm cr}$). γ-rays can also be produced due to inverse Compton scattering of background stellar photons or CMB photons by CR electrons. In other words, γ-rays can also be of leptonic origin. In this case, a photon with relatively low energy can attain very high energy after scattering with relativistic electrons. The emitted photon has an energy of $E_{\rm emitted} \sim \Gamma^2 E_{\rm incident}$, where Γ is the Lorentz factor of the electron which takes part in the scattering process. This process can upscatter a photon having an energy in the range of far-infrared or ultraviolet (0.01 – 100 eV) to the energy range of γ-rays (0.1 – 100 GeV). Note that, the radio emission (as discussed in the previous section)

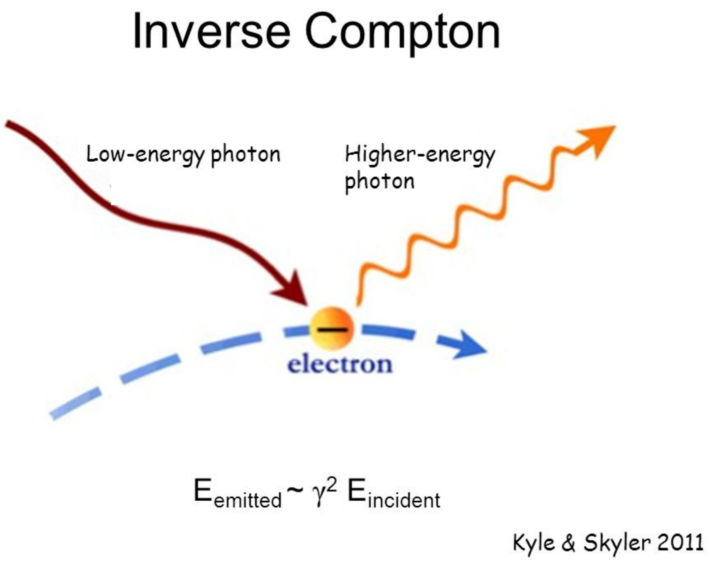

Fig. 1.9 Inverse Compton scattering of low energy photons to high energy in the presence of relativistic electrons.

indicates accelerated electrons where as the γ-rays can be originated from both protons and very high energetic electrons.

The power due to the inverse Compton effect for a single electron having Lorentz factor Γ in a background photon energy density e_{ph} can be written as (Rybicki & Lightman, 1979),

$$P_{\mathrm{IC}} = \frac{dE_{\mathrm{IC}}}{dt} = \frac{4}{3}\sigma_T\, c\,\Gamma^2\,\beta^2\, e_{\mathrm{ph}}\,. \tag{1.30}$$

Here, σ_T is the interaction crosssection, β is the ratio v/c and c is the speed of light. This is the Larmor formula that describes the power radiated by an accelerating charged particle due to electromagnetic radiation. For a relativistic charged particle, this result has been achieved by extending the classical Larmor formula to account for relativistic effects. From the above equation, one can compute the total Compton power, per unit volume, from a distribution of relativistic electrons. If we consider $n(\Gamma)\,d\Gamma$ is the number of electrons per unit volume with Γ in the range Γ to $\Gamma + d\Gamma$, then the power per unit volume can be written as

$$P_{\mathrm{tot}} = \int P_{\mathrm{IC}}\, n(\Gamma)\, d\Gamma \quad \mathrm{erg\,s^{-1}\,cm^{-3}}\,. \tag{1.31}$$

Assuming the distribution of CR electrons with Lorentz factor to be $n(\Gamma) = \kappa_1 \Gamma^{-p}$, and assuming $\beta \sim 1$, we obtain after doing the above integration,

$$P_{\text{tot}} = \frac{4}{3}\,\sigma_T\, c\, e_{\text{ph}}\, \kappa_1\, \frac{\Gamma_{\text{max}}^{3-p} - \Gamma_{\text{min}}^{3-p}}{3-p} \quad \text{erg}\,\text{s}^{-1}\,\text{cm}^{-3}. \tag{1.32}$$

Finally, the total inverse Compton luminosity can be calculated by integrating equation 1.32 over the volume and is given by Rybicki & Lightman 1979, eqn 7.21,

$$L_\gamma^{\text{IC}} = \int_V dV \left[\frac{4}{3}\sigma_T\, c\, e_{\text{ph}}\, \kappa_1\, \frac{\Gamma_{\text{max}}^{3-p} - \Gamma_{\text{min}}^{3-p}}{3-p}\right] \quad \text{erg}\,\text{s}^{-1}, \tag{1.33}$$

where e_{ph} is the background photon energy density (i.e. stellar photons or CMB photons), σ_T is the Thomson scattering cross-section, κ_1 is the normalization constant. Therefore, γ-ray observations (see figure 1.10) are always linked to high-energy particles, i.e. CRs, whether they are electrons or nuclei.

For the highest energy photons, quantum effects become important for Inverse Compton scattering. This is known as the Klein-Nishina effect (Heitler, 1954). The principal effect is to reduce the cross-section from its classical value as the photon energy becomes large compared to the rest mass energy of the electrons. However, since the number density of CR electrons decreases rapidly with energy the contribution of Klein-Nishina effect is expected to be small and is neglected here.

1.2.6 All particle cosmic ray spectra & the need for alternative Galactic cosmic ray sources

As outlined in section 1.2.1, SNR shocks are considered the primary location for the acceleration of CRs. In section 1.2.2, it was also shown that these SNRs can accelerate particles up to 10^{5-6} GeV (Lagage & Cesarsky, 1983a; Axford, 1994). However, observations of CRs indicate the presence of particles up to several times 10^{11} GeV which is at least five orders of magnitude above the maximum accelerated energy in SNR shocks (see fig 1.1). Therefore some other sources must exist that can accelerate particles in this energy range beyond PeV (10^6 GeV). At the very highest energies $E > 10^9$ GeV, protons with rigidities $R > 10^9$ GV have gyroradii at least 10 times greater than the half-thickness of the disc. It is, therefore, impossible to confine them to the plane of the Galaxy. It is generally assumed that the very highest energy particles above $\sim 10^9$ GeV are of extragalactic origin. These can be γ-ray bursts, active galactic nuclei, jets from black holes and radio jets, etc. Theoretically, for a typical Galactic magnetic field strength of 3 μG, CRs with an energy of $Z \times 10^8$ GeV have a Larmor radius of $\sim$ 36 pc, which

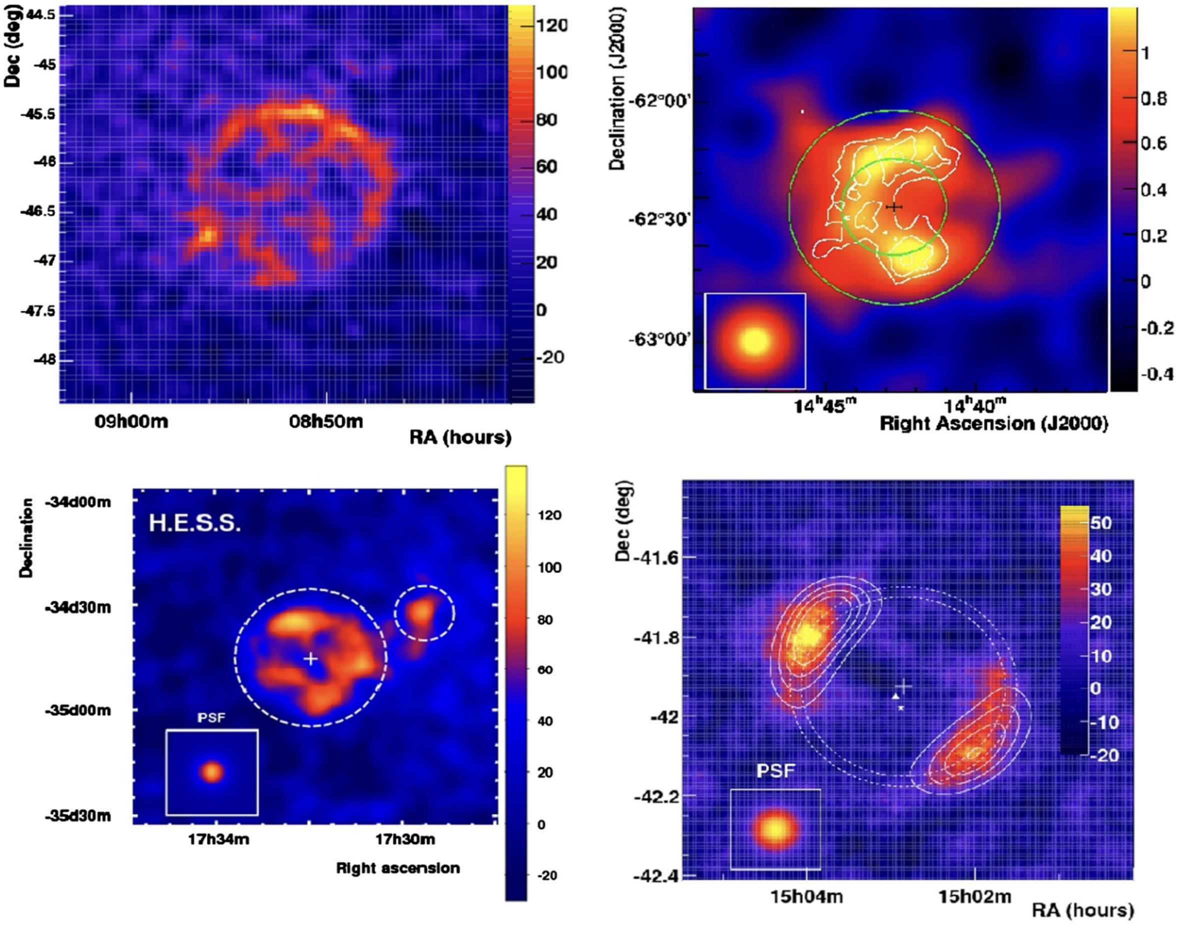

Fig. 1.10 H.E.S.S. γ-ray image of Vela Junior SNR (top left, linear color scale is in units of excess counts per bin), RCW 86 SNR (top right, the linear color scale is in units of excess counts per arcmin^2), HESS J1731–347 SNR (bottom left, the linear color scale is in units of excess counts per bin), and SN 1006 SNR (bottom right, linear color scale is in units of excess counts per bin) Hewitt & Lemoine-Goumard (2015).

is much smaller than the size of the Galaxy's diffusion halo—generally estimated to be a few kpc in cosmic-ray propagation studies. This means CRs with up to $\sim 10^9$ GeV energy remain confined within the Galaxy. However, there still remains uncertainty regarding the sources of these CRs with energies ranging from a few times 10^6 GeV to 10^9 GeV, which are believed to originate within our Galaxy. Moreover, these CRs cannot be accelerated by supernova remnant shocks. Hence, there must be some other Galactic sources that can accelerate particles beyond the SNR limit up to $\sim 10^9$ GeV. However, the standard scenario of acceleration around SNR shocks is known to bear several problems (Gabici et al., 2019), and additional/complementary sources of CRs have been sought in the literature. One such problem concerns the abundance ratios of certain isotopes which are different from solar abundances and yet not secondary products. For example, the observed ratio of ^{22}Ne to ^{20}Ne in Galactic CRs (GCRs) is 5.3 ± 0.3 times the solar value (Maeder & Meynet, 1993) and it cannot be satisfactorily explained by SNe shocks in the ISM.

Several alternative hypotheses have been proposed to explain the CR spectrum in the range of $1 - 100$ PeV. These include collective effects in superbubbles (Bykov & Toptygin, 2001; Bykov et al., 2018) or young massive stars (Biermann & Cassinelli, 1993), the re-acceleration of CR particles by the galactic wind termination shock (GWTS; Jokipii & Morfill 1987; Zirakashvili & Völk 2006; Merten et al. 2018), and young stellar clusters emitting a collective wind (Aharonian et al., 2019; Vieu et al., 2022). Interest in the latter has surged recently due to the discovery that these sources are efficient gamma-ray emitters up to hundreds of TeV (Aharonian et al., 2019; Abeysekara et al., 2021; Aharonian et al., 2022). It has been observed that massive stars are often found in clusters (Higdon & Lingenfelter, 2005), where they produce stellar winds driven by radiation pressure from escaping photons. This continuous wind outflow from young massive stars creates a 'superbubble' within the parent molecular cloud (Weaver et al., 1977). These environments are expected to induce highly turbulent plasma, which traps particles and generates shocks that compress the medium and accelerate the particles, allowing a significant fraction of the stellar energy to be efficiently converted into CRs. Thus, particle acceleration in these environments is expected to be effective, facilitated by either the stellar winds (Cesarsky & Montmerle, 1983), turbulence (Montmerle, 1979; Bykov & Toptygin, 2001), or supernova explosions within superbubbles (Parizot, 2014; Ferrand & Marcowith, 2010; Vieu et al., 2022).

Several arguments support the superbubble origin of CRs. Notably, the enrichment of the accelerated medium by the winds of massive stars has been shown to address the ^{22}Ne / ^{20}Ne anomaly observed in galactic CRs (Higdon & Lingenfelter, 2003; Gupta et al., 2020). Additionally, the plasma composition around massive star clusters or OB associations is expected to differ from that of the standard interstellar medium due to enrichment by the winds of Wolf-Rayet (WR) stars. This may account for several composition anomalies observed in the local CR flux. Tatischeff et al. (2021) show that the volatile components of CRs (N, Ne, Ar) predominantly originate from plasma with a temperature of 2 million Kelvin, which is typical of the intense environments within Galactic superbubbles created by the energetic processes of massive star winds and supernova explosions. Parizot & Drury (1999) argued that a superbubble model for the origin of Galactic CRs can also explain the evolution of light elements Li, Be, and B through spallative production. Therefore, the dynamics of interstellar bubbles (ISBs), and the possible effects of CRs on them, deserve to be studied in detail.

1.3 Star clusters as alternative cosmic ray sources

Recent detections of γ-rays around young star clusters (shown in figure 1.11) have strengthened the possibility of these young star clusters as potential sites for CR acceleration (Aharonian et al., 2019). Several sources have been detected up to hundreds of TeV energy (Ackermann et al., 2011; Abramowski et al., 2012; Abeysekara et al., 2020; Abeysekara et al., 2021). Notably, many of these observations are linked to massive star clusters or OB associations originating from star-forming regions. The LHAASO observatory has reported the detection of a PeV photon coincident with the Cygnus region (Cao et al., 2021), which is an OB association born within star-forming regions, implying CRs having tens of PeV energy are produced therein (Note that in section 1.2.4 we have already discussed that at high energies a CR proton of energy E_p gives a γ-ray photon with energy $E_\gamma \approx 0.1 E_p$). The maximum energy of CRs produced within star clusters, OB associations, or superbubbles is expected to increase compared to the case of an isolated SNR because the stellar outflows should in principle be able to excite a strong turbulent magnetic field, which is needed to confine the particles. We will discuss the details of superbubble morphology, and acceleration process in detail in the following sections.

1.3.1 Stellar wind and formation of stellar bubble

Observations of the spectra from extremely luminous hot stars, which ionize diffuse nebulae, indicate a continuous loss of material from their surfaces. This ongoing loss of mass is commonly referred to as a stellar wind. The factors influencing stellar winds, including their causes, ejection rates, and velocities, vary depending on the mass of the star. In cooler, lower-mass stars like the Sun, the stellar wind originates from the exceptionally high temperature (measured in millions of degrees Kelvin) of the corona. This high temperature is believed to result from interactions between magnetic fields at the star's surface, providing the coronal gas

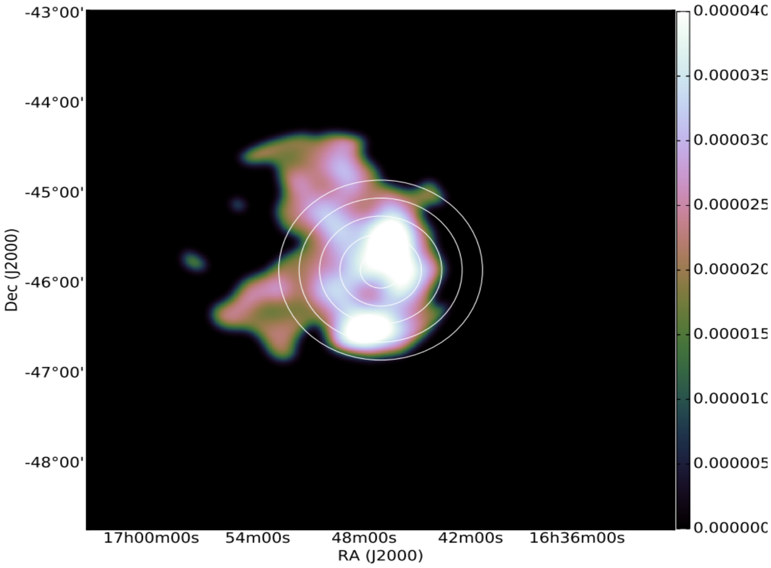

Fig. 1.11 The HESS VHE excess map for Westerlund 1 region, which is a young compact star cluster. The map was produced using the public data on the H.E.S.S website. The white circles represent the regions used for the extraction of the radial distribution of γ-ray emissivities (Aharonian et al., 2019).

with enough energy to overcome the star's gravitational pull and escape as a wind. Stars of this category typically release only a minuscule fraction of their mass annually through stellar winds. In contrast, hot, massive stars can generate stellar winds billions of times more potent than those of low-mass stars. Throughout their relatively short lifespans, these stars can expel vast amounts of material in the form of winds. These stellar winds are primarily propelled by the radiation pressure exerted by photons escaping from the star. For our study, we consider the wind from massive OB stars inside compact massive star clusters.

The stellar wind initially pushes the interstellar gas at highly supersonic velocities. Acting like a piston, the wind generates a shock wave in the interstellar gas. As this shock wave moves outward, it accumulates mass from the surrounding interstellar medium (ISM). The accumulated matter forms a shell that acts as an obstacle or piston within the wind's flow. The wind advances supersonically towards this piston, or conversely, the piston progresses supersonically into the wind when viewed from a different frame of reference. Consequently, a reverse shock naturally forms. This interaction naturally results in the formation of a reverse shock. Unlike the shock wave within the interstellar gas, this reverse shock is directed toward the star. This reverse shock is referred to as the wind termination shock (hereafter, WTS), which will be discussed in more detail in the following section. This flow pattern creates a cavity-like structure around stars.

1.3.2 Star cluster population in the Galaxy

A star cluster is defined as an association of stars over a scale under a few tens of pc, which is not necessarily gravitationally bounded. These clusters can be divided into several categories.

Massive star clusters: A Massive Star Cluster (MSC) is defined by the presence of progenitors of supernovae (SNe), specifically stars with zero-age main-sequence (ZAMS) masses greater than approximately 8 $M_\odot$ (Poelarends et al., 2008; Smartt et al., 2009). Note that, this definition automatically rules out clusters older than roughly 40 Myr, as all supernova progenitors are anticipated to undergo explosions within this timeframe. We leave aside the possibility of thermonuclear supernovae in clusters which is still unclear (Shara & Hurley, 2002).

Young massive star clusters: A Young Massive Star Cluster (YMSC) is characterized by the presence of stars that are expected to enter the Wolf-Rayet (WR) phase towards the end of their life cycle. It is generally assumed that stars with zero-age main-sequence (ZAMS) masses exceeding roughly 20 $M_\odot$ will evolve into WR stars (Sander et al., 2012). Consequently, young clusters are typically defined as those that are less than approximately 10 million years old, assuming uniform star formation.

Evolved massive star cluster: Unlike Young Massive Star Clusters (YMSCs), Evolved Massive Star Clusters (EMSCs) are defined by the absence of Wolf-Rayet (WR) stars, indicating an age greater than 10 million years. As a result, their wind mechanical power is significantly reduced compared to YMSCs, with a large portion of their energy budget being derived from supernova (SN) explosions (Vieu et al., 2022).

Compact massive star cluster: Depending on the morphology MSC will be called compact if the massive stars are distributed inside a very compact region of the order of a few pc at the center of the cluster.

Extended massive star clusters: The distribution of massive stars can extend beyond tens of parsec.

Young massive compact star cluster or the wind-blowing cluster: If a Young Massive Star Cluster (YMSC) is sufficiently compact, the powerful winds from the massive young embedded early-type stars are anticipated to merge into a collective outflow. We have focused on this specific type of cluster in our study due to the presence of a global WTS that is strong enough to accelerate particles to very high energies.

Loose clusters: In contrast to wind-blowing clusters, we define loose MSCs as the MSCs that are unable to power a collective outflow, which includes both extended and evolved clusters.

1.3.3 Structure of stellar superbubble

Here we discuss the morphology of young massive compact stellar clusters (YMSCs) which form within dense molecular clouds. As discussed in the previous section, the stellar feedback from massive stars heats the surrounding medium which inflates a cavity around the stars (Weaver et al., 1977). If a significant concentration of OB-type massive stars is located at the core of a compact star cluster, they will collectively form a sizable bubble encompassing the star cluster, rather than distinct individual stellar bubbles. This phenomenon can be understood as the cumulative impact of numerous massive stars within a confined area. The cavity keeps expanding during the whole cluster lifetime. After several Myr, it reaches a size of about 100 pc and is commonly referred to as a superbubble. Figure 1.12 shows the simple schematic diagram of a stellar wind-driven bubble. There are four distinct regions in the plot: (1) the innermost portion which is the core of the cluster and contains the massive stars that have continuous high-velocity mass outflow, and (2) the free-wind region where the wind originating from the source expands adiabatically. After this region, the wind enters the WTS which converts part of the energy of this wind into thermal energy. (3) the extended shocked stellar wind gas region that contains slightly more dense and hot gas. since the Mach number of this WTS is very high (because the free wind velocity is much higher than the adiabatic sound velocity), this shock is very strong. (4) the outermost thin shell containing the swept-up ambient gas. This is a shell of interstellar gas that has passed through the outer shock. The shocked interstellar medium (ISM) and shocked wind regions are separated by a contact discontinuity (CD). This implies that there is no mass flow across this surface. However, across this surface, the temperature, density, and other physical properties of the gas change abruptly.

The dynamics and the structure of a stellar wind bubble are usually understood by the momentum and energy conservation equations (Weaver et al., 1977):

$$\frac{d}{dt}(M\dot{R}) = 4\pi R^2 \mathscr{P} \tag{1.34}$$

$$\frac{d}{dt}\left(\frac{4}{3}\pi R^3 \frac{\mathscr{P}}{\gamma-1}\right) = L_w - 4\pi R^2 \dot{R} \mathscr{P} \tag{1.35}$$

Where $\mathscr{P}$ is the pressure inside the bubble, R is the position of the swept-up shell of ISM. The equation 1.34 considers the conservation of momentum of the shell and the equation 1.35 considers the conservation of energy of the shocked stellar wind. The shell is assumed to be very thin because radiative cooling is very effective in the shell region and this cooling drastically increases the compression. A single radius, R, can be applied both to the radius of the thin shell and to the outer radius of the bubble of hot, shocked wind gas. Additionally, since the shocked wind region is thick, we will assume that the shocked wind gas occupies the

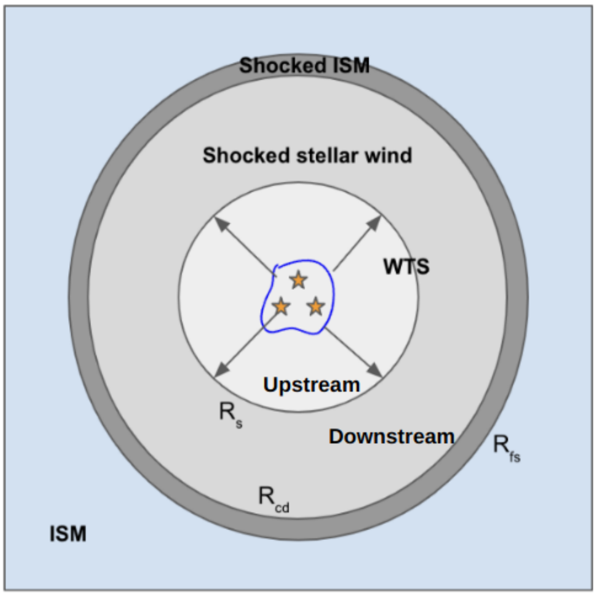

Fig. 1.12 Schematic diagram of a stellar wind bubble. The position of termination shock is R_s; R_{cd} and R_{fs} are contact discontinuity and forward shock positions, respectively.

majority of the volume within the shock surface of radius R. Since the interstellar gas is at rest, $\dot{R}(=dR/dt)$ represents both the shock velocity relative to the interstellar gas and the expansion velocity of the bubble. M is the swept-up ambient mass. L_w is the wind power (which is sometimes referred to as kinetic luminosity). The term on the left-hand side of equation 1.34 represents the rate at which the momentum of the thin shell changes, while the term on the right-hand side represents the force exerted on it. Equation 1.35 indicates that the change in thermal energy in the shocked wind region over time is equal to the energy input from gas entering the WTS, minus the energy expended by the hot gas doing work on the surrounding medium. Let us also assume the ambient density with a general form of,

$$\rho(r) = \rho_c \left(\frac{r_c}{r}\right)^s . \tag{1.36}$$

We assume that R is given by an expression of the form,

$$R \propto t^{\alpha} , \tag{1.37}$$

and substituting $\mathscr{P}$ from equation 1.34 to equation 1.35 one can obtain (Gupta et al., 2018a),

$$R = C_1 L_w^{1/(5-s)} \left(\rho_c r_c^s\right)^{-1/(5-s)} t^{3/(5-s)} \tag{1.38}$$

$$\mathscr{P} = C_2 L_w^{(2-s)/(5-s)} \left(\rho_c r_c^s\right)^{3/(5-s)} t^{-(4+s)/(5-s)} \tag{1.39}$$

where,

$$C_1 = \left[\frac{(\gamma - 1)\,(5-s)^3\,(3-s)}{4\pi(63-18s)\gamma + s(2s+1) - 28}\right] \tag{1.40}$$

$$C_2 = \left[\frac{(21-6s)}{(5-s)^2\,(3-s)}\right] C_1^{(2-s)}\,. \tag{1.41}$$

If we put $s = 0$, the solution for the constant ambient medium can be obtained (Weaver et al., 1977). Consider a star cluster where the majority of massive stars ($M_\star > 8M_\odot$) are concentrated within a core radius R_c. The total mechanical power emitted by these massive stars from a spherical region of radius R_c can be expressed as $L_w = \dot{M}\upsilon_w^2/2$, where υ_w represents the wind velocity and $\dot{M}$ is the total mass of out-flowing wind per unit time. Near the core of this bubble, the wind undergoes adiabatic expansion, resulting in a mass density of $\rho_w = \dot{M}/(4\pi r^2\,\upsilon_w)$. The WTS forms at the point where the wind ram pressure ($P_{\rm ram} = \rho_w \upsilon_w^2$) balances the pressure of the hot gas pressure ($\mathscr{P}$) within the bubble. Consequently, the radius of the WTS with respect to the center of the star cluster is determined by:

$$R_{\rm ts} \approx \left(\frac{L_w}{2\pi\,\upsilon_w\,\mathscr{P}}\right)^{1/2}\,. \tag{1.42}$$

This suggests that if a cluster is compact enough (i.e., $R_c << R_{\rm ts}$) then a global WTS can form. For a uniform ambient medium, the position of the reverse shock is given (by substituting $\mathscr{P}$ from equation 1.39 into equation 1.42),

$$R_{\rm ts} = 2.45\,\rho_2^{-3/10}\,\dot{M}_{-4}^{1/2}\,L_{39}^{-1/5}\,\upsilon_3^{1/2}\,t_6^{2/5}\ \text{pc}\,. \tag{1.43}$$

Here, density $\rho_2 = \rho/(10^2\,{\rm m_H\,cm^{-3}})$, mass loss rate $\dot{M}_{-4} = \dot{M}/(10^{-4}\,{\rm M_\odot yr^{-1}})$, kinetic luminosity $L_{39} = L_w/(10^{39}\,{\rm erg\,s^{-1}})$, velocity of wind $\upsilon_3 = \upsilon_w/(10^3\,{\rm km\,s^{-1}})$ and age of the bubble $t_6 = t/(1\,{\rm Myr})$. If the radiation loss is important due to cooling of the shell hence the term L_w in the previous equations can be replaced by ηL_w, where $\eta \leq 1$ can be thought as the energy efficiency parameter.

1.3.4 Different sites of cosmic ray acceleration in star clusters

For this thesis, I will consider young massive compact star clusters (YMSC) because these types of clusters create a superbubble and a strong global WTS which can accelerate particles up to very high energy. Particles can be accelerated in different regions inside a star cluster such as in the free wind region, at the WTS, and at the forward shock.

Particle acceleration at the superbubble forward shock: SBs are delimited by a forward shock, whose size and velocity are readily given by Eq. 1.38. Thus shocks, while propagating through the ISM can accelerate ISM particles according to the diffusive shock acceleration mechanism. Even assuming optimistic values for the mechanical power ($\mathscr{P} = 10^{39}$ erg/s) and ambient ISM density $n_0 = 1\,\mathrm{cm}^{-3}$ the forward shock rapidly becomes weak. e.g. $\dot{R} = 65$ km/s at $t = 1$ Myr. The forward shock is decelerated once the remnant has swept up enough mass and becomes weak with time. In the case of a weak shock, the maximum energy achieved by the particles via DSA is generally limited by the available acceleration time.

Particle acceleration at Wind termination shock (WTS): The winds emanating from the cluster's center intersect the WTS at speeds reaching several thousand kilometers per second. The distance of the WTS from the center can be approximated by the equation 1.42. Shifting the reference frame to that of the WTS, one can visualize the WTS advancing towards the wind region with equivalent velocity. This scenario is analogous to Diffusive Shock Acceleration (DSA) occurring at the forward shock of Supernova Remnants (SNRs). However, a key difference is in the material being accelerated: while ambient interstellar medium (ISM) particles are accelerated at the SNR shock, the WTS accelerates particles within the winds of massive stars. Also, the WTS remains as a strong shock for a very long time compared to the isolated SNR forward shocks.

SNRs inside the cluster: Supernova remnants (SNRs) that explode in the central regions of young compact clusters are not initially launched into the low-density superbubble (SB) cavity. The fate of SNR shocks expanding deeply within the cluster remains uncertain. It is likely that such shocks, with pressures and sizes comparable to the stellar outflows from the most massive stars, will be disrupted before they exit the cluster. This disruption is expected to increase turbulence and magnetic field strength in the cluster's core. In contrast, SNRs located near the core radius initiate shocks in the free wind region. These shocks, as they propagate through the free wind, can accelerate particles from the wind material similar to what occurs in isolated SNRs. The SNR shocks follow a self-similar solution of the form $R \propto t^{7/8}$ (Gaggero et al., 2018). Particles are accelerated around the SNR shocks in the upstream region of the WTS (Gupta et al., 2020). The maximum energy achieved is constrained by the size or age of the shock.

1.3.5 Maximum energy gain of cosmic rays in massive star clusters

The WTS is a strong shock that can accelerate particles according to the diffusive shock acceleration mechanism (discussed in section 1.2.1). Particles can also be accelerated in the free wind region as well as in the forward shock of the expanding bubble. The maximum achieved energy can be calculated using the Hillas criterion (Hillas, 1984), which is commonly invoked to set an upper bound on the maximum energy of the particles accelerated in a given source as $E_{\max} \leq ZeBRu/c$, where u, B, R are respectively the typical wind velocity, magnetic field and radius of the shock where the particles accelerate. This criteria also has been discussed in section 1.2.2 in detail.

The maximum CR energy depends on the extent of the accelerating region, in the case of a superbubble, the width of the shocked wind region, that separates the WTS and contact discontinuity (Gupta et al., 2020). Assuming typical values of these parameters like $B = 10\mu$G the magnetic field inside SBs, $R \sim 50$ pc the size of the shocked wind region, and $u = 5000$ km/s the typical velocity of stellar winds, one obtains $E_{\rm max} \sim 4Z$ PeV, which is higher than the case for an isolated SNR. This simple estimate has long motivated the possibility of SBs as a source of super PeV protons.

As mentioned in the previous section, particles can be accelerated in different locations inside a superbubble. The forward shock can have a large radius of $\sim$ 100 pc (Weaver et al., 1977), however, it is too slow (velocity of a few tens of km/s) to accelerate PeV protons. Inside superbubbles, there are mainly two types of strong shocks: the SNR shock which expands through the free wind region after the explosion of massive stars at the edge of the central core, and the global WTS which surrounds the central core and the free wind region. The size of the WTS depends on the mechanical power of the stellar cluster and is typically of the order of 10 pc (Weaver et al., 1977). In both of these cases, the maximum energy of a few PeV can be achieved by the protons (Gupta et al., 2020; Vieu et al., 2022; Morlino et al., 2021), which is higher than the case of isolated SNR. However, a potentially advantageous scenario, combining both WTS and SNRs, could involve the expansion of an SNR within a wind profile near a compact cluster. A young massive compact cluster has the potential to transform a significant portion of its mechanical energy into turbulence, leading to the enhancement of magnetic fields to levels reaching hundreds of μG in its nearby region. This phenomenon enables particles to undergo acceleration to energies as high as 10 PeV by a powerful SNR moving through the wind, even without further amplification of the magnetic field. Exploring a comparable situation involving the interaction between SNR shock and cluster wind with effective turbulence production, Bykov et al. (2015) discovered that proton energies of up to 40 PeV could be attained under the condition of fast shocks with velocity $\sim 10^4$ km/s. This value is more than one order magnitude higher than the case of the acceleration in an isolated SNR.

1.4 Propagation and associated microphysics of cosmic rays

After getting accelerated from various astrophysical sources the CRs escape the source and propagate through the ISM. The escaping particles diffuse in the ISM magnetic field (MF) and join the CR background at a distance where their density drops below the average CR Galactic density.

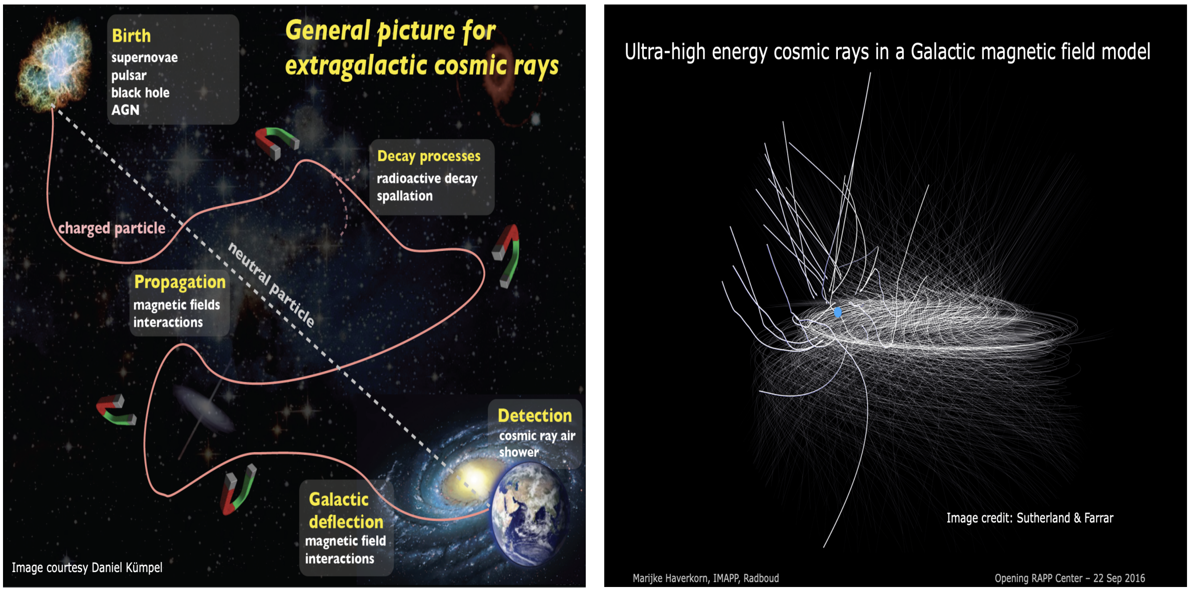

Fig. 1.13 *Left:* Cosmic ray propagation from source to earth through the ISM. The particles follow the ISM magnetic field during their propagation. *Right:* The pictorial representation of the Galactic magnetic field and the propagation of cosmic rays along those field lines.

1.4.1 Confinement of cosmic rays around source & their escape

In the vicinity of a shock, the level of turbulence is anticipated to be much above that of an average region of the interstellar medium. Upstream of the shock, the flux of CRs interacting with the shock is highly anisotropic and thus very unstable to the generation of hydromagnetic waves. The waves are amplified by the shock so that the downstream region will also be very turbulent. The rate of wave generation increases with the CR flux and thus depends on the rate of injection of CR particles in the acceleration mechanism. Due to this, turbulent magnetic fields around the shock can be tangled and modified which can act as magnetic field fluctiations and irregularities and the particles will repeatedly scatter in those. Note that, during the DSA mechanism we discussed the scattering of particles from magnetic fluctuations (i.e. magnetic mirror) which plays an important role in the back-and-forth motion of the particles around shocks. These magnetic fluctuations generated due to the turbulence in the medium act as the scattering centers.

With the increase in energy, the Larmor radius of the particles increases. When the Larmor radius of accelerated particles exceeds the extent of the acceleration region, these particles escape the source region and begin to propagate through the interstellar medium (ISM). Upon leaving the source, the initial CR transport in the Galaxy is primarily governed by diffusion parallel to the local magnetic field lines (see fig 1.13). This configuration of transport has been shown to trigger the onset of resonant streaming instability, subsequently reducing the diffusion coefficient and confining CRs in the vicinity of the source for a considerable duration. Furthermore, the streaming motions give rise to the generation of magnetic fluctuations via Alfven and hydromagnetic waves, which amplify in amplitude over time. This process generates magnetic irregularities even in the absence of initial fluctuations, due to the streaming of high-energy particles. Consequently, CR diffusion near the shock region proceeds at a sluggish pace, resembling the 'confinement' of CRs around the shock.

1.4.2 Propagation from the source and the effect of propagation on the observed cosmic ray spectra

The discussions in Section 1.4.1 indicate that, owing to random scattering caused by magnetic field irregularities, which may be produced from field fluctuations or the development of instabilities induced by particle streaming motions, high-energy charged particles diffuse from their sources across the interstellar medium. Hence, a diffusion coefficient, denoted as D, can be employed to characterize their movement. Various additional phenomena can arise during this propagation, including energy loss resulting from radiation emitted by charged particles (i.e., cooling-induced energy loss), and particle fragmentation due to interactions between CR particles and interstellar medium particles (spallation). An effective approach to studying these phenomena on the particle spectrum involves employing a partial differential equation. This equation describes the energy spectrum at various locations within the interstellar medium, considering both energy losses and the ongoing influx of new particles from sources.

The diffusion-loss equation describing the propagation of high-energy nuclei through interstellar gas, accounting for fragmentation gains and losses of a particular species i can be expressed as (Longair, 1992),

$$\frac{\partial N_i}{\partial t} = D(E)\nabla^2 N_i + \frac{\partial}{\partial E}[b(E)N_i] + Q_i - \frac{N_i}{\tau_i} + \sum_{j>i} \frac{P_{ji}}{\tau_j} N_j \,. \tag{1.44}$$

Where N_i is the number density of CR nuclei of species i and is a function of energy E, the first term in the RHS $D(E)\nabla^2 N_i$ is the diffusion term with $D(E)$ is the diffusion coefficient, $\partial/\partial E\,[b(E)N_i]$ considers the energy loss of the particles with $b(E) = -(dE/dt)$, and Q_i is the injection term of particles of species i per unit volume. The last two terms describe the loss and gain respectively due to spallation. τ_i and τ_j are the spallation lifetimes of particles of species i and j. The spallation products of all species with $j > i$ provide contributions to N_i, as indicated by the sum in the last term of equation 1.44. P_{ji} is the probability that, in an inelastic collision involving the destruction of the nucleus j, the species i is created.

The radiative energy loss term is mainly important for CR electrons. For protons and other nuclei, one can neglect the loss term due to their large cooling time. To understand the effect of diffusion on the spectra of CR nuclei observed at Earth (or any other location), let us assume a very simple scenario where the energy loss is negligible, a steady state under the continuous injection of particles from sources, and also neglect the spallation term. We also assume there is an infinite, uniform distribution of sources, each injecting high energy electrons with an injection spectrum $Q(E) = \kappa E^{-p}$, where p is the index of accelerated particles at the shock and κ is the normalization constant. Under these assumptions equation 1.44 can be expressed as,

$$D(E)\nabla^2 N = \kappa E^{-p} \;\Rightarrow N \propto \frac{\kappa E^{-p}}{D(E)}. \tag{1.45}$$

The diffusion coefficient depends on the particle energy (E) and a generally adopted form is $D(E) \propto E^{\delta}$. Using this in the above equation one gets the CR number density,

$$N \propto \kappa E^{-p-\delta}. \tag{1.46}$$

In general, the parameter δ typically ranges from 0.3 to 0.6, depending on the selected models for CR propagation, while the value of p is approximately 2. Understanding this is essential because, although particles are initially accelerated at the source with an index of 2, the observed spectra at different locations in the universe are modified by an additional factor of δ, solely due to the energy-dependent diffusion of particles during propagation.

1.4.3 Energy loss of cosmic ray electrons during their propagation

High-energy electrons undergo various energy loss processes (this is called *radiative cooling*) that result in distortions of their injection energy spectra as they traverse the interstellar medium from their sources. The mechanisms of loss entail interactions with matter, magnetic fields, and radiation. To see the effect of cooling during propagation on the CR electron spectra let us again consider the previous assumptions but in this case, we need to include the cooling term. For simplicity, we neglect diffusion in this calculation. Hence, under these assumptions equation 1.44 will take the form,

$$\frac{\partial}{\partial E}[b(E)N] = -\kappa E^{-p} \tag{1.47}$$

Assuming $N(E) \rightarrow 0$ as $E \rightarrow \infty$, 1.47 can be integrated to give,

$$N(E) \propto \frac{\kappa E^{-(p-1)}}{(p-1)b(E)}. \tag{1.48}$$

The form of $b(E)$ will be dependent on the various cooling processes such as ionization losses, adiabatic losses, synchrotron radiation, inverse Compton scattering, Bremsstrahlung emission, etc. This can be expressed as,

$$b(E) = -\frac{dE}{dt} = A_1\left(ln\frac{E}{m_ec^2}+19.8\right)+A_2E+A_3E^2 . \tag{1.49}$$

The first term on the right-hand side, A_1, represents the ionization losses; the second term, A_2, accounts for bremsstrahlung losses and adiabatic losses if applicable (these losses are proportional to particle energy); and the last term, A_3, describes inverse Compton and synchrotron losses (these losses are proportional to square of the energy, Longair 1992). Therefore from equation 1.48, (i) if ionization losses are the dominant factor, $N(E) \propto E^{-(p-1)}$, making the energy spectrum flatter by one power of E; (ii) if bremsstrahlung or adiabatic losses dominate $N(E) \propto E^{-p}$, resulting in no change to the spectrum compared to the injection spectrum; (iii) if inverse Compton or synchrotron losses dominate $N(E) \propto E^{-(p+1)}$, causing the spectrum to become steeper by one power of E. Additionally, if we consider the diffusion term, the modification of δ (as previously discussed for CR nuclei) also applies to electrons.

1.4.4 Confinement time of cosmic rays in the Galaxy

After their acceleration and departure from their sources, CRs travel through the Milky Way. Typically, high-energy particles encounter about 50 kg m^{-2} of material during their propagation from the source to the solar system. Using this information one can calculate an escape time (τ_e) for CRs from our Galactic neighborhood by considering a mean density (ρ) of the material they interact with, using the equation $\zeta = \rho v \tau_e$, where ζ is the amount of material traversed during the propagation. With an interstellar gas number density (N) ranging from 10^5 to 10^6 m^{-3} and assuming CR particles travel at the speed of light, their residence time within our vicinity is estimated at approximately $3\times10^6 - 3\times10^7$ years, as indicated by Longair (1992).

The confinement time can be calculated using radioactive secondary comic ray species. Certain secondary CR species generated in spallation reactions are radioactive, enabling their abundances to serve as indicators for dating CR samples observed near Earth. One of the most important of these radioactive isotopes is beryllium ^{10}Be which has a half-life that is similar to the escape time τ_e found above. This ^{10}Be is produced as a spallation product from heavier elements like carbon, and oxygen. The radioactive ^{10}Be eventually undergoes β^- decays into stable ^{10}B nuclei. Thus, the relative ratios of beryllium and boron isotopes provide insight into whether all the ^{10}Be has decayed, thereby providing an estimate of the average age of the CRs detected in our vicinity. To account for the radioactive decay of species i, an additional term must be introduced into the diffusion-loss equation 1.44. If the decay time (i.e. e-folding time) is τ_r, this additional term has the form $-N_i/\tau_r$. If the typical time it takes the CRs to reach the Earth from their sources is less than τ_r, the ratio of $[^{10}Be]/[^{7}Be+^{9}Be+^{10}Be]$ should correspond to the relative production rates of these species, about 10%. Conversely, if the escape time τ_e is much longer than τ_r, this ratio should be very much less than 10%. The isotopic abundance ratio should be of order τ_r/τ_e of the production ratio if $\tau_e >> \tau_r$.

Let us present a simple derivation of the expected abundance of ^{10}Be in a model with a characteristic escape time τ_e for CRs from the Galaxy. For simplicity, we further assume that the steady state is reached, hence $\partial N_i/\partial t = 0$, radiative losses ^{10}Be are not significant, and that all beryllium isotopes are generated only through the spallation of primary elements. The production rate of any isotope i is given by (Longair, 1992):

$$A_i = \sum_{j>i} \frac{P_{ji}}{\tau_j} N_j \,. \tag{1.50}$$

The term P_{ji} denotes the probability of an inelastic collision involving the destruction of the nucleus j, and the creation of species i. Under these simplifications, taking into account that $\tau_{\text{spal}}(i)$ represents the timescale over which isotope i is destroyed by inelastic collisions, the steady-state abundance of a non-radioactive isotope can be obtained from the simplified transfer equation:

$$-\frac{N_i}{\tau_e(i)} + A_i - \frac{N_i}{\tau_{\text{spal}}(i)} = 0 \quad \Rightarrow \quad N_i = \frac{A_i}{\frac{1}{\tau_e(i)} + \frac{1}{\tau_{\text{spal}}(i)}} \,. \tag{1.51}$$

If the isotope j is radioactive, another loss term is added to the transfer equation. If $\tau_r(j)$ is the characteristic decay time, then

$$-\frac{N_j}{\tau_e(j)} + A_j - \frac{N_j}{\tau_{\text{spal}}(j)} - \frac{N_j}{\tau_r(j)} = 0 \quad N_j = \frac{A_j}{\frac{1}{\tau_e(j)} + \frac{1}{\tau_{\text{spal}}(j)} + \frac{1}{\tau_r(j)}} \,. \tag{1.52}$$

Hence, the steady-state ratio of the ^{10}Be and ^{7}Be isotopes can be expressed as,

$$\frac{N(^{10}Be)}{N(^{7}Be)} = \frac{\frac{1}{\tau_e(^{7}Be)} + \frac{1}{\tau_{\text{spal}}(^{7}Be)}}{\frac{1}{\tau_e(^{10}Be)} + \frac{1}{\tau_{\text{spal}}(^{10}Be)} + \frac{1}{\tau_r(^{10}Be)}} \frac{A(^{10}Be)}{A(^{7}Be)} \,. \tag{1.53}$$

If the duration needed for the destruction of beryllium isotopes through spallation greatly exceeds their escape times $\tau_{\text{spal}} >> \tau_e$, a simpler equation can be derived,

$$\frac{N(^{10}Be)}{N(^{7}Be)} = \frac{\frac{1}{\tau_e(^{7}Be)}}{\frac{1}{\tau_e(^{10}Be)} + \frac{1}{\tau_r(^{10}Be)}} \frac{A(^{10}Be)}{A(^{7}Be)} \,. \tag{1.54}$$

In this expression, terms like folding time for beryllium and the production rate of isotopes are known, the ratio of the escape time is known, the ratio $^{10}Be/^{7}Be$ is measured, and only the escape time is an unknown quantity. Experiments conducted by the Chicago group distinguished the isotopes of beryllium, revealing a ratio of $[^{10}Be]/[^{7}Be+^{9}Be+^{10}Be] = 0.028$ (Simpson, 1983). By substituting this value into the previous equation, an escape time of approximately 10^7 years is determined.

1.4.5 The isotropy of cosmic rays at higher energy ($\geq 10^{14}$ eV)

High energy CRs ($\geq 10^{14}$ eV) are mainly detected by detecting the air shower induced by a CR particle in the atmosphere of Earth. In experiments studying CR air showers, the incoming trajectories of CRs are determined, allowing for estimation of their distribution's isotropy in the sky. Isotropy describes properties unaffected by direction, while anisotropy varies with direction. Detecting the arrival direction of CR particles increases anisotropy. However, both CR nuclei and electrons with energies below approximately 10 GeV are significantly affected by solar modulation, leading to a loss of information about their arrival directions in the Solar System. Only high-energy protons and nuclei can reach Earth's vicinity without significant deflection by the interplanetary magnetic field. The deflection experienced by a particle can be quantified by the ratio of its gyroradius in the interplanetary magnetic field to the scale of the Solar System. For relativistic particle, gyroradius can be expressed as $r_g = \gamma m v_{\text{perp}}/qB$, where B is the magnetic field, q is the charge of the particle, v_{perp} is the velocity perpendicular to the magnetic field, m is the mass of the particle and γ is the Lorentz factor. Following this, for relativistic proton, the gyroradius is given by (Longair, 1992),

$$r_g = 3\times 10^9\,\gamma(B/10\,\mu G)\ \text{m}. \tag{1.55}$$

Here, γ represents the Lorentz factor, and B denotes the magnetic flux density. Assuming a typical value local magnetic flux density in the interplanetary medium is $B = 10,\mu$G, relativistic protons with $\gamma = 10^3$, corresponding to energies of 10^3 GeV, have gyroradii of $\sim 3\times 10^{12}$ m, which is equivalent to few tens of astronomical units (AU). This distance is comparable to the extent of the solar system. As a result, particles with these energies or higher are likely to retain information about their arrival directions within the Solar System upon reaching the Earth's atmosphere.

When high-energy protons and nuclei collide with atoms and molecules in the upper atmosphere, they produce pions. These charged pions decay into muons, which have relatively short half-lives, causing them to decay well before reaching the Earth's surface unless they are highly relativistic with $\gamma \geq 20$. This process forms the foundation for studies on the isotropy

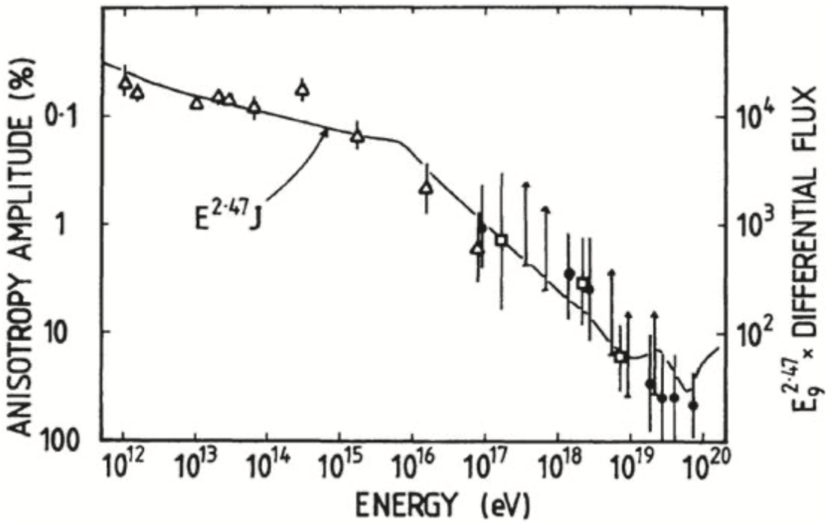

Fig. 1.14 The amplitude of the anisotropy in the distribution of arrival directions of cosmic rays as a function of energy. In each case, a best-fitting sine wave was fitted to the data, and the percentage amplitude of this harmonic was measured. The solid line shows the shape of the differential spectrum of cosmic rays (Hillas, 1984).

of CRs using underground muon detectors, which are designed to detect primary particles entering the atmosphere with energies of 10^3 GeV and higher. The results from these detectors, along with data on even higher-energy particles, are presented in 1.14, as reported in the review by Hillas (1984). It is noteworthy that in the $10^{13} - 10^{14}$ eV range, the distribution of arrival directions for high-energy particles is remarkably uniform, with a very low level of anisotropy detected.

Figure 1.1 illustrates that the CR spectrum overall experiences a steepening around $\sim 10^{15}$ eV. Ginzburg & Syrovatskii (1964) noted that the gyroradius of a proton with an energy of 10^{15} eV is roughly equal to the scale of magnetic irregularities, estimated at $\lambda \sim 0.1$ pc, which is believed to cause CR scattering. Particles with energies exceeding this threshold can travel directly from their sources to Earth, potentially increasing the measured anisotropy, as shown in Figure 1.14. At the very highest energies, $E > 10^{19}$ eV, protons have gyroradii at least 10 times greater than the half-thickness of the Galactic disc, making it impossible to confine them to the plane of the Galaxy. In the Galactic magnetic field, CRs with $E \sim 10^{20}$ eV are barely deflected and thus should travel almost directly from their sources to Earth, resulting in higher anisotropy. However, there are issues resulting from intergalactic magnetic fields, that affect the propagation path of those extragalactic CRs. This may make the interpretation difficult (Ryu et al., 2010).

1.5 Motivation for the thesis

In the previous sections, we have discussed many interesting aspects of CRs. In this thesis, we explore the potential of star clusters as sources of cosmic ray acceleration. For the past 40-50 years, supernova remnants have been identified as particle accelerators. However, recent observations have detected star clusters as gamma-ray sources, suggesting the possibility of particle acceleration within these objects. Several recent studies have also discussed the potential of these clusters as cosmic ray sources. We aim to strengthen these arguments by focusing on the recent gamma-ray observations from the WD1 star cluster, in the context of underlying cosmic ray acceleration. Another unresolved question is the energy range in which these star clusters accelerate particles. We focus on this issue and, based on our theoretical understanding of the morphology of young star clusters, propose the energy range in which particle acceleration occurs in these objects. To fully understand cosmic rays, it's essential to consider their lower energy spectrum, where significant contributions arise from nearby supernova remnants. Hence, we also focus on the lower energy segment of the cosmic ray spectrum (GeV-TeV) and attempt to explain the recently observed spectral features considering the nearby supernova remnants and using our theoretical framework for cosmic ray propagation.

- *Cosmic ray acceleration in star cluster as the origin of observed gamma rays:*

  Recent detections of star clusters as gamma-ray sources have sparked considerable interest among astronomers (Aharonian et al., 2019; Cao et al., 2021; Abeysekara et al., 2020). The origin of these gamma rays can be accelerated particles around those star-forming regions. The detection of the Westerlund 1 cluster in gamma rays by Aharonian et al. (2019) motivates us to study this particular cluster as a high-energy particle accelerator. Our motivation was to theoretically explain the observation considering particle acceleration in different regions of the star cluster and also to explain theoretically the $1/r$ type radial dependency of the CR energy density calculated from observation.

- *Cosmic rays from a distribution of massive star clusters as potential second Galactic CR component:*

  The identification of individual star clusters as CR accelerators has led to the pivotal question: What is the collective contribution of CRs originating from the multitude of star clusters distributed throughout the Galaxy? This question serves as the driving force behind our second project, where we investigate the cumulative impact of CRs from the realistic distribution of star clusters (Bronfman et al., 2000) within the Galaxy. Additionally, we aim to ascertain whether this component originating from star clusters can explain the observed all-particle spectra above the 'knee'. As discussed earlier, supernovae are unable to accelerate particles beyond the ‘knee’, necessitating the existence of other sources to accelerate particles above this energy threshold.

- *The role of the nearby supernova remnants in explaining the observed spectral bump in proton and helium spectra around TeV energy:*

  The presence of nearby discrete CR sources is anticipated to exert significant effects on the observed spectra of CRs. Previous experiments like ATIC (Panov et al., 2006), CREAM (Yoon et al., 2011), and PAMELA (Adriani et al., 2011) have observed a spectral hardening around TeV energies in CR proton and helium spectra. This hardening can be explained by previous models considering nearby CR sources that accelerate particles. This local component can be thought of as an additional component to the existing diffuse background component of CRs. However, recent more accurate measurements by DAMPE (An et al., 2019; Alemanno et al., 2021) and CALET (Adriani et al., 2022a, 2023) measured not only a hardening around TeV and again a softening around hundreds of TeV, which we call a ‘bump’ like feature. This observation motivates us to study the effect of nearby sources in light of the updated age and distances of those sources considering different diffusion scenarios and try to explain the observed spectral bump in proton and helium.

1.6 Structure of the thesis

This thesis is structured as follows:

In **Chapter 2**, we examine the impact of CR (CR) acceleration within the dense compact star cluster Westerlund 1, particularly in light of its recent detection in gamma rays. Considering different injection sites of CRs inside the star cluster we try to explain the observation. We explore theoretically whether this observed profile can aid in distinguishing between two scenarios debated in the literature: (1) continuous CR acceleration within the star cluster's stellar wind-driven shocks, and (2) discrete CR acceleration occurring in multiple supernovae shocks. We also point out the differences between the projected gamma-ray luminosity and the true radial luminosity around the source. We use the idealized hydrodynamic simulation code PLUTO for our analysis.

Chapter 3, is a continuation of the previous chapter, here we consider a distribution of star clusters in the Galaxy, instead of a single star cluster. Considering this realistic distribution, maximum energy estimate inside star clusters and accurate abundances of stellar wind material, we discuss the possibility of massive young star clusters as potential candidates capable of accelerating Galactic CRs (CRs) within the energy range of $10^7 - 10^9$ GeV, situated between the 'knee' and 'ankle' features. We provide an in-depth analysis of CR transportation within the Galaxy, considering diffusion, interaction losses during propagation, and particle re-acceleration by aging supernova remnants. This calculation aims to establish the complete spectrum of all CR particles for the whole energy range from 1 GeV to 10^{11} GeV by combining different components of CRs.

In **Chapter 4**, we turn our attention to a recently observed feature in the CR spectra around TeV energies. These observations have revealed a bump-like new feature in the proton and helium spectra in the energy range of $\sim (1-100)$ TeV. The origin of the feature is not clearly understood. In this study, we try to explain this feature using the CRs produced in the nearby supernovae that are within a 1 kpc distance from the Earth. We use the updated distance and age of the sources and also consider a time-dependent escape of CRs from the sources which are crucial for the study. We study different scenarios of CR diffusion from sources and seek to understand the effect on the observed spectra. Additionally, we do an extensive comparison between our findings regarding the secondary-to-primary ratios anticipated for alternative existing models.

We summarise our findings and conclude in **chapter 5**.

2

Cosmic ray acceleration in star clusters as the origin of observed gamma rays

Based on:

"Cosmic rays from massive star clusters: a close look at Westerlund 1", **Bhadra, S.**, Nath, B., Sharma P., Monthly Notices of the Royal Astronomical Society, **510**, 5579, 2022.

(Bhadra et al., 2022)

We investigate the impact of cosmic rays (CRs) acceleration within the dense stellar cluster Westerlund 1, following its recent detection in γ-rays. Employing 1-D two-fluid hydrodynamical simulations, we model CR energy density profiles, considering potential acceleration scenarios in the central region and/or at the wind termination shock (WTS). Our aim is to align these profiles with the observed projected γ-ray luminosity and CR energy densities. Recent findings indicate a radial $1/r$ distribution of the CR energy density, prompting us to explore whether this distribution can discern between continuous CR acceleration at stellar wind-driven shocks within the cluster and discrete acceleration at multiple supernovae shocks, topics often debated in the literature. Through idealized two-fluid simulations and variations in acceleration sites and diffusion coefficients, we derive CR energy density profiles and luminosities to best fit the γ-ray observations.

Main results

- The key insight from our analysis is that the observed $1/r$ profile of CR energy density may not accurately represent its actual radial profile. Additionally, we have demonstrated that the observed data can support a more gradual CR energy density profile, particularly when considering updated error estimates.
- Although a $1/r$ profile for the CR energy density offers a straightforward explanation, attributing it to a steady-state CR luminosity at the cluster's center, thus presenting an attractive proposition, we have investigated more realistic scenarios. These include variations such as time-varying CR luminosity or CR injection occurring outside the central region (such as at the WTS), and we have illustrated how these scenarios align with observations. None of the CR acceleration sites can be ruled out based solely on these observations.
- Both the continuous stellar wind and the discrete multiple supernova injection scenarios can account for the γ-ray observations given the suitable selection of parameters.

2.1 Introduction

The idea that massive star clusters are potential acceleration sites of CRs has long been discussed in the literature, beginning with energetic arguments (Cesarsky & Montmerle, 1983). CR acceleration in these environments can also solve many problems associated with the isolated supernova paradigm, including proton acceleration up to $\sim$ PeV energies (representing the knee of the Galatic CR spectrum) and the excess of ^{22}Ne/^{20}Ne in CRs compared to the standard ISM composition (Higdon & Lingenfelter, 2003), for a review, see Gabici et al. (2019). Detailed theoretical investigations support these predictions (e.g., (Gupta et al., 2020; Morlino et al., 2021). In this regard, Gupta et al. (2020) have demonstrated that the problem of the large observed ratio of Neon isotopes (^{22}Ne/^{20}Ne) can be solved by invoking CR acceleration in the stellar winds in star clusters. Concurrently, it has been suggested from various phenomenological considerations that most of the observed CR grammage in the Galaxy is accumulated in star clusters, and not while propagating through the interstellar medium (ISM) at large (see, e.g., Cowsik & Madziwa-Nussinov 2016; Eichler 2017; Biermann et al. 2018). Taking this cue, Nath & Eichler (2020) have shown that the γ-rays resulting from star clusters can explain a significant fraction of the observed diffuse Galactic background. These developments prod us to look deeper at the individual and detailed observations of star clusters.

Recently, using the γ-ray observations of Cygnus and Westerlund 1 (hereafter referred to as Wd1) and CO/HI observations, Aharonian et al. (2019) reported that the spatial distribution of CR energy density in these objects follows a $1/r$ profile. They suggested a steady injection (over $\sim$few Myr) of CRs instead of instantaneous injection as normally expected in the case of an isolated supernova. Although such profiles can be derived by solving the steady-state CR transport equation, it is worth mentioning that the steady-state assumption is questionable when the shock-bubble structure continuously evolves. We subject these observations to scrutiny with two-fluid hydro simulation and check if other interpretations (of the actual CR energy density profile and the mode of CR injection) are ruled out and if the observations can be used to infer the relevant physical parameters for CR acceleration.

In this chapter, we have studied different CR injection methods in order to understand the observed γ -ray luminosity, mass, and CR energy density of the Wd1 cluster. We selected Wd1 for our study mainly because it is a compact cluster and can be modeled convincingly using 1-D simulations. Although there are a few other clusters that have been detected in γ-rays such as Cygnus (Bartoli et al., 2014; Abeysekara et al., 2021), those objects are distinctly non-spherical in morphology and have substructures, which make them difficult to compare with 1-D simulations. We begin with analytical estimates of γ-ray luminosity in section 2.2. The numerical simulation setup is described in section 2.3. In section 2.4, we present our results, followed by further discussions in section 2.5, and we summarize in section 2.6.

2.2 Preliminaries

In a couple of massive star clusters (e.g., Wd1 cluster; see Aharonian et al. 2019), the CR energy density in different annuli, as estimated from γ-ray luminosity, has been found to follow a $1/r$ profile. These profiles are often interpreted in terms of a steady injection of CRs (with energy E) from the dense core of a compact star cluster with an energy-dependent CR diffusion (diffusion coefficient $\kappa_{\rm cr}(E)$). This can be shown directly by using the CR diffusion-transport equation:

$$\frac{\partial N(E)}{\partial t} = \kappa_{\rm cr}(E)\nabla^2 N(E) + Q(E), \tag{2.1}$$

where, $N(E)$ is the number density of CRs and $Q(E)$ is their energy injection rate density. The energy moment of this equation can be written as

$$\frac{\partial e_{\rm cr}}{\partial t} = \kappa_{\rm cr}\nabla^2 e_{\rm cr} + \frac{L}{V}, \tag{2.2}$$

where $e_{\rm cr}$ represents CR energy density, $\kappa_{\rm cr}$ is an appropriately averaged diffusion coefficient for CRs, and $\frac{L}{V}$ the CR luminosity density. Let us assume that CR particles are injected in a small central region of radius r_0, which is much smaller in extent than the size of the star cluster. The rest of the volume is assumed to be devoid of CR production sites for simplicity. Therefore, except in the very central region, we need to solve the equation

$$\frac{\partial e_{\rm cr}}{\partial t} = \kappa_{\rm cr}\nabla^2 e_{\rm cr}\,. \tag{2.3}$$

In steady state, it reduces to (in spherical symmetry)

$$\frac{d}{dr}\left(r^2 \frac{d}{dr} e_{\rm cr}\right) = 0\,, \Rightarrow e_{\rm cr} \propto \int \frac{dr}{r^2}\,, \tag{2.4}$$

which has the solution $e_{\rm cr} = \frac{A}{r} + B$, where $B \to 0$ since the CR energy density is zero at infinity, and where A is a constant that depends on the boundary condition at r_0. This is the $1/r$ solution which is taken to be a piece of evidence for steady injection of CR energy in massive clusters(Aharonian et al., 2019).

Clearly, the above estimate neglects some crucial aspects such as (1) advection of CRs, (2) role of CR acceleration sites other than the central region, (3) losses due to radiative cooling of the gas, (4) projection effects, and (5) dominating γ-ray emission regions (which can be different from acceleration site. These considerations are important in the case of massive star clusters. Therefore, time-dependent numerical simulations are essential. Our two-fluid approach allows us to consider the WTS as an acceleration site, as well as to study the effect of time-varying CR/mechanical luminosity of the star cluster, including discrete SNe.

2.2.1 γ-ray luminosity (L_γ)

2.2.1.1 Hadronic contribution

One of the major sources of γ-rays in Wd1 is the hadronic interaction between CR protons and protons in the ambient gas (see below for an estimate of γ-ray flux in the leptonic case, from inverse Compton scattering of stellar photons by CR electrons). The mechanism of production of γ-rays is

$$p+p \rightarrow p+p+\pi^0, \quad \pi^0 \rightarrow \gamma+\gamma. \tag{2.5}$$

Therefore, observations of γ ray photons hold clues to the spatial distribution of CR protons. To estimate γ-ray luminosity due to hadronic interactions, we use the prescription of Dermer's model (Dermer, 1986; Pfrommer & Enßlin, 2004), which yields the luminosity between ($E_{\gamma 1}$ and $E_{\gamma 2}$) energies:

$$L_\gamma^H = \int_V dV \int_{E_{\gamma 1}}^{E_{\gamma 2}} dE_\gamma E_\gamma q_\gamma(n_N, e_{\rm cr}, E_\gamma) = \int_V dV\, n_N(r)\, e_{\rm cr}(r) \left[\int_{E_{\gamma 1}}^{E_{\gamma 2}} dE_\gamma E_\gamma \tilde{q}_\gamma\right]. \tag{2.6}$$

Here, $q_\gamma = dN/(dt\, dV\, dE_\gamma)$ is the number of γ-ray photons emitted per unit volume per unit time per unit energy, which is proportional to the number density of target nucleon (n_N) and the CR energy density ($e_{\rm cr}$). The integration is to be carried over the entire volume of the emission region. The omnidirectional source function $\tilde{q}_\gamma$, used in the second integral, is given as (see Pfrommer & Enßlin 2004; Gupta et al. 2018b; Jana et al. 2020):

$$\tilde{q}_\gamma = \frac{\sigma_{pp} c \left(\frac{E_{\pi^0}}{GeV}\right)^{-\alpha_\gamma} \left[\left(\frac{2E_\gamma}{E_{\pi^0}}\right)^{\delta_\gamma} + \left(\frac{2E_\gamma}{E_{\pi^0}}\right)^{-\delta_\gamma}\right]^{-\frac{\alpha_\gamma}{\delta_\gamma}}}{\xi^{\alpha_\gamma - 2} \left(\frac{3\alpha_\gamma}{4}\right) \left(\frac{E_p}{(2\alpha_p - 2){\rm GeV}}\right) \left(\frac{E_p}{\rm GeV}\right)^{1-\alpha_p} \beta\left(\frac{\alpha_p - 2}{2}, \frac{3-\alpha_p}{2}\right)}. \tag{2.7}$$

The decay of π^0 particles occurs in all directions (i.e. omnidirectional decay). Therefore, the differential γ-ray source function can be determined by assuming that the decay products are distributed isotropically in the π^0 rest frame (for details please see Equations (8), (19)–(21) in Pfrommer & Enßlin 2004). Here, $\xi = 2$ is the multiplicity factor, which denotes two leading pion jets leaving the interaction site, E_p and E_{π^0} are the rest mass energy of proton and pions (π^0) respectively. The spectral indices of the incident CR protons and emitted γ-ray photons are denoted by α_p and α_γ respectively, $\delta_\gamma = 0.14\alpha_\gamma^{-1.6} + 0.44$ is the spectral shape parameter and

$\sigma_{pp} = 32(0.96 + e^{4.4-2.4\alpha_\gamma})$ mbarn (for details see equations (8) and (19)–(21) in Pfrommer & Enßlin 2004). We use $\alpha_\gamma = \alpha_p = 2.3$ following the spectral fit of Ackermann et al. (2015). The integration over the γ-ray photon energy in equation 2.6 for $E_{\gamma 1} = 1$ TeV and $E_{\gamma 2} = 100$ TeV (the contribution at higher energies is very small) gives 1.05×10^{-17} cm^{3}s^{-1}. Thus the γ -ray luminosity above 1 TeV can be written as,

$$L^H_\gamma \sim 10^{-17} \left(\frac{\Delta V}{\mathrm{cm}^3}\right) \left(\frac{n_N}{\mathrm{cm}^{-3}}\right) \left(\frac{e_{\mathrm{cr}}}{\mathrm{erg\,cm}^{-3}}\right) \quad \mathrm{erg\,s}^{-1} . \tag{2.8}$$

We use this equation to calculate the γ-ray luminosity from the relevant region of the cluster. On inverting equation 2.8 we get the CR energy density above 10 TeV,

$$e_{\mathrm{cr}}(> 10\mathrm{TeV}) \approx 1.5 \times 10^{-2} \left(\frac{L^H_\gamma}{10^{34}\,\mathrm{erg\,s}^{-1}}\right) \left(\frac{10^6 M_\odot}{M}\right) \quad \mathrm{eV\,cm}^{-3} . \tag{2.9}$$

where M is the mass and L_γ is the γ-ray luminosity above 1 TeV energy.

2.2.1.2 Leptonic contribution

It is also possible to have a leptonic contribution to the total γ-ray luminosity, from inverse Compton scattering of stellar radiation photons by CR electrons, especially close to the star cluster where stellar photon density is significant. We estimate the leptonic emission as follows.

The energy density of CR electrons is assumed to be 0.01 of the total CR energy density (i.e $e_{\mathrm{cr,e}} \approx 0.01 e_{\mathrm{cr}}$). This value has some uncertainty. From observations in the solar system, at CR energy ~ 10 GeV, where solar modulation effects are low, the ratio of CR electron to proton energy is known to be 1% (Longair 1992 section 15.1, Schlickeiser 2002). Assuming the energy distribution of CR electrons to be $n(\Gamma) = \kappa_1 \Gamma^{-p}$ (in terms of the Lorentz factor Γ), where $p = 2.3$ (same as that of protons). The normalization constant κ_1 is obtained from the energy density of CR electron $e_{\mathrm{cr,e}}$ as,

$$\kappa_1 \approx \frac{e_{\mathrm{cr,e}}}{m_e c^2}(p-2)\left[\frac{1}{\Gamma_L^{p-2}} - \frac{1}{\Gamma_U^{p-2}}\right]^{-1} . \tag{2.10}$$

Here, the upper cutoff to the Lorentz factor can be taken as $\Gamma_U \to \infty$ and the lower cutoff (Γ_L), as unity. The theoretical lower limit of unity represents CR electrons with minimal kinetic energy, while the upper limit, extending to infinity, represents those with the highest possible kinetic energy. This range is set to encompass the full energy spectrum of CR electrons. Then, the total IC luminosity (which provides an upper limit to γ-ray luminosity) is given by (Rybicki

& Lightman 1979, eqn 7.21),

$$L_\gamma^{IC} = \int_V dV \left[\frac{4}{3} \sigma_T \, c \, e_{\rm ph} \, \kappa_1 \, \frac{\Gamma_{\rm max}^{3-p} - \Gamma_{\rm min}^{3-p}}{3-p} \right], \tag{2.11}$$

where, $e_{\rm ph}$ is the photon energy density, which at a distance r from the central core region of star cluster is given by

$$e_{\rm ph} = \frac{L_{\rm rad}}{4\pi r^2 c}. \tag{2.12}$$

Hence one can obtain an upper limit to the leptonic contribution by using equations 2.10, 2.11 & 2.12. Using these equations, one gets a sharply declining profile of L_γ with distance, because of the rapid decline of $e_{\rm ph}$ with radius. This is in contrast with the observed increasing profile of L_γ with projected distance. The observed profile, therefore, works against the leptonic interpretation of the origin of γ-rays.

Since IC scattering boosts the seed photon energy by a factor of Γ^2 (Γ being the electron Lorentz factor), a seed (stellar) photon of ~ 1 eV will require $\Gamma = 10^6$ for it to be scattered into 1 TeV energy. If we take the photons in the waveband 0.01–100 eV (FIR to FUV), then the total radiation luminosity of the cluster is given by $L_{\rm rad} \sim 500 L_w$ (Leitherer et al., 1999), where L_w denotes the mechanical luminosity. In the innermost region considered here, within 9 pc, the photon energy density amounts to ≈ 1125 eV/cc. Therefore, electrons that do not cool within 4.5 Myr have $\Gamma \leq 120$, which require a seed photon energy of ≥ 70 MeV in order to upscatter to 1 TeV. Note that, this incident photon energy is much greater than our assumed seed photon energy (0.01–100 eV). Therefore no photons in this region can be upscattered to above 1 TeV. If we put $\Gamma = 120$ as $\Gamma_{\rm max}$ and $\Gamma_{\rm min} = 1$ in equation 2.11, we get,

$$L_\gamma^{\rm IC} \sim 10^{-18} \left(\frac{L_w}{10^{39} \mathrm{erg\,s^{-1}}} \right) \times \left[\int dV \left(\frac{r}{10\mathrm{pc}} \right)^{-2} e_{\rm cr}(r) \right] \quad \mathrm{erg\,s^{-1}}, \tag{2.13}$$

where dV and $e_{\rm cr}$ are in cgs unit. A comparison with equation 2.8 shows that even *total* IC losses (only a negligible fraction of this is emitted above 1 TeV) are smaller than the hadronic luminosity above 1 TeV.

2.2.2 CR energy density ($e_{\rm cr}$)

Although our simulation can track the CR energy density ($e_{\rm cr}$), observations can only determine it through projection, and that too indirectly using L_γ and the total projected mass in different projected annuli. In order to compare our calculations with observed parameters, we note that Aharonian et al. (2019) have estimated the CR energy density $e_{\rm cr,inf}$ above 10 TeV using the following expression (their equation 7, which is almost identical to our equation 2.9),

$$e_{\mathrm{cr,inf}}(>10\mathrm{TeV}) = 1.8\times10^{-2}\left(\frac{\eta}{1.5}\right)\left(\frac{L_{\gamma}}{10^{34}\mathrm{erg/s}}\right)\left(\frac{10^{6}M_{\odot}}{M}\right)\ \mathrm{eV\,cm^{-3}}, \tag{2.14}$$

where M is the mass and L_{γ} is the γ-ray luminosity above 1 TeV energy. We use the subscript 'inf' to emphasize that this is the *inferred* value of CR energy density, in order to distinguish from the real value, which we get from simulation. η accounts for nuclei heavier than hydrogen in both CRs and ISM. Clearly, the value of η depends on the chemical composition of the ambient gas and CRs. The composition parameter η varies between 1.5 to 2 (Dermer, 1986), and here we have used $\eta = 1.5$. Note that, we mainly consider those CRs which have energy more than 10 TeV in our calculations. Also note that the equations 2.9 and 2.14 are in good agreement.

2.2.3 Distance to Wd1: recent updates and estimation of age

There has been an uncertainty regarding the distance to the Wd1 cluster. Aharonian et al. (2019) have used a distance of 4 kpc. However, the recent Gaia Early Data Release 3 (hereafter 'EDR3') (Aghakhanloo et al., 2021) has provided a more accurate determination of the distance of Wd1, of 2.8 kpc, which is smaller than previously thought. All the distances we use in our simulation, as well as calculations, are based on the Gaia EDR3 (Aghakhanloo et al., 2021). The observed value of projected γ-ray luminosity, as well as projected mass, also have been modified accordingly. In other words, the physical sizes of the bins have been decreased by a factor of $4/2.8 = 1.42$.

As far as the age is concerned, Aghakhanloo et al. (2021) stated that the turnoff mass would be reduced from 40 $M_{\odot}$ to 22 $M_{\odot}$, which would imply an increase in the age. However, Negueruela et al. (2010) found the turn off mass to be ~ 25 $M_{\odot}$, and the age, $4-5$ Myr. Also, one can estimate the age from the relative number of Wolf-Rayet to Red Supergiants irrespective of the distance, and this yields an age of $4.5-5$ Myr. Moreover, the age of the WD1 cluster cannot be more than ~ 5 Myr, since Wolf-Rayet stars cannot last longer than this (although Beasor et al. 2021 has claimed a much larger age of 7.2 Myr). Here, we use an age of 4.5 Myr, and we show our results at this epoch. The physical and simulation parameters for Wd1 are in table 2.1.

Westerlund1			
Observations		**Simulation parameters**	
Extension (pc)	60	$\varepsilon_{\rm cr}/w_{\rm cr}$ **range covered**	$0.1-0.3$
Age of cluster (Myr)	$4-6$	$\kappa_{\rm cr}$ **range covered**	$(5-100)\times 10^{26}$ cm^2 s^{-1}
Kinetic Luminosity L$_{\rm w}$ (erg s^{-1})	10^{39}	**Simulation box size**	250 pc
Distance (kpc)	2.8	**No of grids**	5000
Mass loss rate $\dot{\rm M}$ (M$_\odot$/yr)	7.5×10^{-4}	**Cooling**	Tabulated

Table 2.1 Various physical and simulation parameters of Westerlund 1 used in this work.

2.3 Numerical set up

We use the publicly available magneto-hydrodynamics code, PLUTO (Mignone et al., 2007), our version of which supports CRs as a fluid detailed in Gupta et al. (2021). PLUTO is a finite-volume Godunov code based on Riemann solvers, designed to integrate a system of conservation laws of fluid dynamics that adopts a structured mesh. In this work, the code solves the following set of equations:

$$\frac{\partial \rho}{\partial t} + \nabla \cdot (\rho \vec{v}) = S_\rho \tag{2.15}$$

$$\frac{\partial (\rho \vec{v})}{\partial t} + \nabla \cdot (\rho \vec{v} \otimes \vec{v}) + \nabla (p_{\rm th} + p_{\rm cr}) = \rho \vec{g}, \tag{2.16}$$

$$\frac{\partial (e_{\rm th} + e_k)}{\partial t} + \nabla [(e_{\rm th} + e_k)\vec{v}] + \nabla [\vec{v}(p_{\rm th} + p_{\rm cr})] = p_{\rm cr} \nabla \cdot \vec{v} - \nabla \cdot \vec{F}_{\rm tc} + q_{\rm eff} + S_{\rm th} + \rho \vec{v} \cdot \vec{g}, \tag{2.17}$$

$$\frac{\partial e_{\rm cr}}{\partial t} + \nabla \cdot [e_{\rm cr} \vec{v}] = -p_{\rm cr} \nabla \cdot \vec{v} - \nabla \cdot \vec{F}_{\rm crdiff} + S_{\rm cr}, \tag{2.18}$$

where ρ is the mass density, $\vec{v}$ is the fluid velocity, $p_{\rm th}$ and $p_{\rm cr}$ are thermal pressure and CR pressure respectively, $e_{\rm k}$ is the kinetic energy density, $e_{\rm th} = p_{\rm th}/(\gamma_{\rm th} - 1)$ and $e_{\rm cr} = p_{\rm cr}/(\gamma_{\rm cr} - 1)$ are the thermal energy density and CR energy density, respectively. S_ρ, $S_{\rm th}$ and $S_{\rm cr}$ are the mass and energy source terms per unit time per unit volume. $\vec{F}_{\rm tc}$, $\vec{F}_{\rm crdiff}$ represents thermal conduction flux and CR diffusion flux, respectively, g denotes the gravity and $q_{\rm eff}$ accounts for the radiative energy loss of the thermal gas. We have used HLL Riemann solver, piecewise linear reconstruction and RK2 time stepping. In our simulation, we use a CFL number of 0.4 and 1-D spherical geometry.

2.3.1 Ambient medium

In the section 2.2.1 we show that a major fraction of γ-rays can be produced due to hadronic interactions, and therefore, modeling the gas density of the cloud is crucial. However, the gas density in these environments is largely uncertain. Current observations provide us with the total mass up to a given radius and the projected density profile when the bubble has already evolved. With this limited information, we have explored various density distributions and finally selected a density profile (as briefly discussed below), which not only shows a good match with the total gas mass of WD1 (Aharonian et al., 2019), but also gives a size of the bubble at ~ 4.5 Myr comparable to observations.

We use a combination of self-gravitating isothermal clouds with solar metallicity following section 4.1 in Gupta et al. (2018b). This gives the total mass density at the central region of the cloud $\sim 625\, m_{\rm H}\ {\rm cm}^{-3}$, which drops radially as $\sim 220(5{\rm pc}/r)\, m_{\rm H}\ {\rm cm}^{-3}$; see e.g., their figure 1, giving the mass $\sim 10^6\ M_\odot$ for a cloud of radius ≈ 100 pc. These numbers are consistent with WD1. Note that, as soon as the wind/SNe becomes active, this initial density profile only remains valid outside the bubble. The interior structure evolves depending on the mechanical energy and mass injections from the star cluster, as we discuss in the following sections.

2.3.2 Wind driving region

The main driving engines in star clusters are stellar wind and supernova explosions. While the stellar wind from individual stars can vary with time, the total wind power and mass can be assumed to be constant over time, which are mainly injected by massive stars located in the central regions of compact clusters such as WD1. Mass and energy are deposited in a spherical region of radius $r_{\rm inj} = 1$ pc around the center (the volume of the injection region is $V_{\rm src} = 4/3\, \pi r_{\rm inj}^3$) and the spatial resolution of the runs is $\Delta r = 0.05$ pc. We set this resolution to minimize un-physical cooling losses (see section 4 in Sharma et al. 2014).

The injection region is chosen in such a way that the radiative energy loss rate is less than the energy injection rate (Sharma et al., 2014). In our simulations, we set the mass loss rate $\dot{M} = 7.5 \times 10^{-4}\ {\rm M}_\odot\ {\rm yr}^{-1}$ (Table 1) and kinetic luminosity $L_w = 10^{39}\ {\rm erg\ s}^{-1}$. The mass loss rate $\dot{M}$ in chosen so that the wind velocity $v \sim [2L_w/\dot{M}]^{1/2}$ for Westerlund1 is nearly 2000 km s^{-1} (Chevalier & Clegg, 1985). An injection parameter $\epsilon_{\rm cr}$ (see equation 2.27) is used to specify the fraction of total injected energy given to CRs. The source term $S_{\rm cr}$ in equation 2.18 can be expressed in terms of the kinetic luminosity of the source region,

$$S_{\rm cr} = \frac{\epsilon_{\rm cr} L_w}{V_{\rm src}} \,. \tag{2.19}$$

Similarly S_ρ (in eqn 2.15) and $S_{\rm th}$ (in eqn 2.17) can be expressed as,

$$S_\rho = \frac{\dot{M}}{V_{\rm src}} \quad ; \quad S_{\rm th} = \frac{(1-\varepsilon_{\rm cr})L_w}{V_{\rm src}} \, . \tag{2.20}$$

2.3.3 CR injection

We consider three different methods of CR injection in this work. In the first case, CRs are injected in the wind-driving region, i.e., within $r_{\rm inj}$. In the second case, CRs are injected into the shocked zones. The last case is a combination of both. These injection regions can be seen as possible CR acceleration sites in this object, where the central injection represents unresolved regions, e.g., colliding winds, which can also accelerate CRs (Eichler & Usov, 1993; Bykov, 2014). We use the following three conditions to identify the shocked zones (Pfrommer et al. 2017, Gupta et al. 2021),

$$\nabla \cdot \vec{v} < 0, \tag{2.21}$$

$$\nabla p \cdot \frac{\Delta r}{p} > \delta_{\rm threshold}, \tag{2.22}$$

$$\nabla T \cdot \nabla \rho > 0\,. \tag{2.23}$$

Here, $\vec{v}$, p, ρ, and T are the velocity, pressure, density, and temperature of the fluid, respectively. The first condition selects compressed zones, the second condition sets the pressure jump at the shock, and the third condition avoids the contact discontinuity. In the third injection method, we use the combined injection of CRs in the wind-driving region as well as in the shocked region.

For all these different injection methods, the injection of CRs does not add any additional energy in the computational domain. The injection parameter ($\varepsilon_{\rm cr}$ or $w_{\rm cr}$, see section 2.4.2) just distributes a fraction of the total mechanical energy in the CRs either in the wind driving region or in the shocked regions.

2.3.4 Microphysics

2.3.4.1 CR Diffusion

Our simulations include the effects of CR diffusion. For numerical stability, diffusion typically has a much smaller time step than the CFL time step. To make our runs faster, we chose the super time-stepping method for the diffusion module, which sub-cycles CR diffusion for each hydro time-step. The CR diffusion flux term can be expressed in terms of CR energy density,

$$\vec{F}_{\rm crdiff} = -\kappa_{\rm cr} \vec{\nabla} e_{\rm cr} \, , \tag{2.24}$$

where $\kappa_{\rm cr}$ is the diffusion coefficient and $e_{\rm cr}$ is the CR energy density. Generally, $\kappa_{\rm cr}$ is a function of CR energy, but here we consider a constant value of $\kappa_{\rm cr}$, which can be thought of as its appropriate energy weighted value across the energy distribution function of CRs (equation 7 in Drury & Voelk 1981).

We use a smaller value for the diffusion coefficient ($\kappa_{\rm cr}$) than generally used for the Galactic scales. We set $\kappa_{\rm cr}$ in the range of $(5–100) \times 10^{26}$ cm^2 s^{-1}. This is justified because CRs escaping the acceleration sites are expected to drive turbulence locally, making them diffuse more slowly compared to the ISM at large (Abeysekara et al., 2021).

2.3.4.2 Cooling

Radiative cooling that causes thermal energy loss of the gas is non-negligible in dense clouds. To include this, we use a tabulated cooling function corresponding to collisional equilibrium and solar metallicity (Ferland et al., 1998; Sutherland & Dopita, 1993). A floor value in temperature is set to $10^4 K$ so that cooling is turned off when temperature $T < 10^4$ K, which arises from the photoionization of the regions in the vicinity of the cluster (Gupta et al., 2016), on a spatial scale much larger than considered here. The ionized region around Wd1 is larger than the outer radius of the cluster, thereby justifying the floor temperature value of 10^4 K. If S_* is the number of ionizing photons emitted per unit time by the star cluster, β_2 is the recombination coefficient of hydrogen (Case B approximation), and n_0 is the ambient density. The radius of the Strömgren sphere be R_S which is given by,

$$R_S = \left(\frac{3}{4\pi} \frac{S_*}{n_0^2 \beta_2} \right)^{1/3} . \tag{2.25}$$

If we use $n_0 = 50\,{\rm cm}^{-3}$, $S_* = 2.26 \times 10^{52}$ s^{-1} (since the ionizing photon luminosity is $\approx 500 L_w$), $T = 10^4$ K, and $\beta_2 = 2 \times 10^{-13}$ cm^{3}s^{-1}, one has the radius of Strömgren sphere as ~ 50 pc. Instead of a uniform medium if we take a $1/r$ -type radial ambient medium then the Strömgren radius will be much larger (the forward shock position is only slightly larger). The net heating is given by

$$q_{\rm eff} = -n_i n_e \Lambda_N + {\rm Heating}\,. \tag{2.26}$$

The heating of gas due to Coulomb interactions with CRs is negligible because the heating timescale is larger than Gyr. We do not include heating due to CR streaming in our simulations, although we discuss its implications in section 2.5.4.

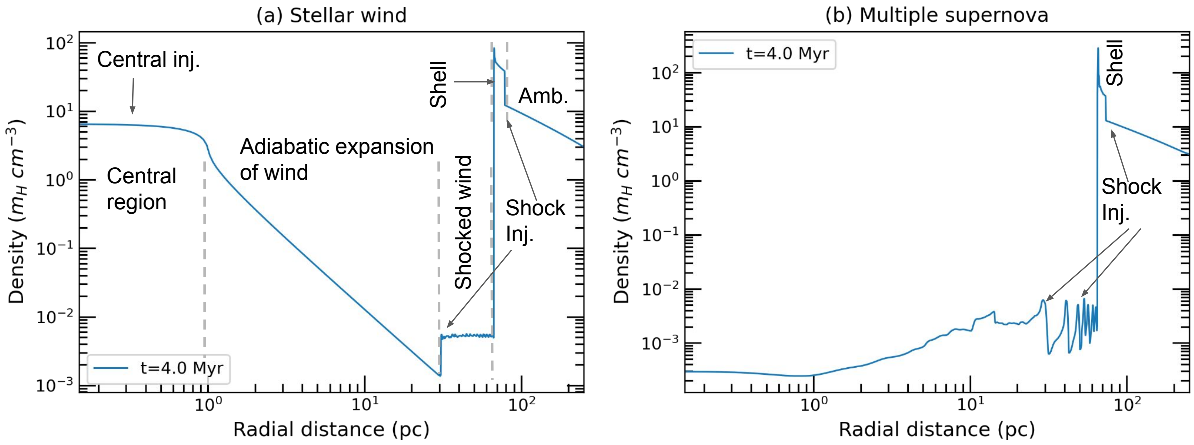

Fig. 2.1 (a) Density profile of a wind-driven bubble at a time $t = 4.0$ Myr. The horizontal axis represents the distance from the center in pc and the y-axis denotes the density in terms of $\mathrm{m_H\,cm^{-3}}$, (b) density profile for multiple supernova injection with SN frequency of 1 SN in each 3×10^4 year. If we increase the Supernova frequency i,e one SN in each 1000 year, then the density profile roughly takes the shape of a continuous shell wind-like structure (shown in blue color in the 1st panel of the lower row in figure 2.3). The label Central inj. in the figure denotes that CRs are injected at the central region and Shock inj. implies CRs are injected at shocks.

2.4 Results

We present our results in this section and then discuss the implications in section 2.5.

2.4.1 Structure of star cluster driven bubble

Star clusters host massive stars as well as supernova explosions, which produce a low-density bubble around them (Weaver et al. 1977; Gupta et al. 2018b). Although the overall size of these bubbles (a few tens of pc) depends mainly on the total mechanical luminosity deposited by the cluster and the ambient density, the interior structure can qualitatively differ depending on whether the energy deposition is dominated by winds or SN explosions (Sharma et al. 2014). We discuss these differences below.

Figure 2.1a shows the density profile of a stellar wind-driven bubble (Weaver et al. 1977) at 4.0 Myr. There are four distinct regions in the plot: (1) the innermost portion contains the source of energy and mass deposition, (2) the free-wind region where the wind originating from the source expands adiabatically, (3) the shocked-wind region contains slightly more dense gas, (4) the outermost shell containing the swept-up ambient gas. The shocked interstellar medium (ISM) and shocked wind regions are separated by a contact discontinuity (CD).

Figure 2.1b shows the corresponding density profile for multiple supernova injections, where 1 supernova occurs every 3×10^4 year. For this small rate, we do not observe any wind-like structure in the density profile, but if we increase the supernova frequency, then the density profile does look similar to the case for continuous stellar wind (Blue curve in the 1st panel of the lower row in figure 2.3), with four distinct regions as mentioned earlier (Sharma et al., 2014).

The size of the bubble, or, to be precise, the distance to the contact discontinuity (CD) is ≈ 80 pc, for an ambient density of $50 m_H$ cm^{-3}. This implies an extended γ-ray emission region of a similar size. Note that 80 pc at a distance of 2.8 kpc subtends an angle of $\approx 98'$. Indeed, the *HESS* excess map (Aharonian et al. 2019, figure 4 in their Supplementary material) shows the γ-ray bright region to have a total extension of $\approx 3^\circ$, consistent with the above estimate for the angular radius. However, we note that roughly half of the last annulus (the fifth) drawn in the same figure by Aharonian et al. (2019) is not γ-ray bright. This makes the γ-ray luminosity of the last projected bin comparable to the fourth bin and not brighter, which it would have been if the γ-ray bright region had filled the last annulus. At the same time, the morphology of the γ-ray bright region shows that it is not spherically symmetric. Thus although there is a rough agreement of the size of the bubble (and, consequently, the γ-ray bright region) from our spherically symmetric simulation with the size of the γ-ray bright region, a bin-by-bin matching of the simulated result with observations may not be possible.

Indeed, from the structure of the stellar wind bubble (Fig 2.1) it is clear that the swept-up shell is much denser than the interior of the bubble. This would result in an enhanced γ-ray luminosity for the outer radial bin, which would, in turn, dominate the projected luminosity in all projected bins.

2.4.2 Different acceleration sites and corresponding observables

As mentioned earlier, we consider three different CR acceleration sites in our simulations: (1) CR energy injection in the central wind region (using $\varepsilon_{\rm cr}$), (2) injection at the shocks (using $w_{\rm cr}$), and (3) combined injection at shocks as well as the central wind region (using both $\varepsilon_{\rm cr}$ and $w_{\rm cr}$). We compare our results with the observations of Aharonian et al. (2019), albeit for a distance of 2.8 kpc to Wd1 as described in section 2.2.3.

2.4.2.1 Central injection

In this scenario, CRs are injected into the source region, after which they diffuse outwards. The kinetic luminosity of the stellar wind is distributed in CRs and thermal energy. We define the injection parameter $\varepsilon_{\rm cr}$ as,

$$\varepsilon_{\rm cr} = \frac{E_{\rm cr}}{E_{\rm IN}}\,, \tag{2.27}$$

where $E_{\rm cr}$ is the energy deposited in CRs and $E_{\rm IN}$ is the total deposited energy into the injection region. We calculated the projected γ-ray luminosity and mass by dividing the cluster region into 5 bins from $0-45$ pc with a width of 9 pc for each bin to compare with the observations of Aharonian et al. (2019). While calculating the projected γ-ray luminosity, we have considered only the hadronic contribution since the leptonic contribution is relatively lower in magnitude than the hadronic contribution.

The fourth column plots the *inferred* CR energy density profile [1] in the same manner that observers would have done, based on the projected luminosity and mass. This has been done in order to bring out the essential difference between the actual radial profile (plotted in the first column of Figure 2.2) and the inferred projected profile of CR energy density, the demonstration of which is the crux of the present work.

Note that Aharonian et al. (2019) calculated the errors in CR density without considering the uncertainty in the mass estimates (which was mentioned as $\sim 50\%$). This has resulted in the underestimation of the errors in the inferred CR energy density. We have, therefore, considered the error in the mass estimates while calculating the final errors in CR energy density. It is found that the revised error bars accommodate a flatter CR energy density profile than expected from a projection of $1/r$ profile. We note that the error mainly arises from the uncertainty in the conversion factor between CO and H_2, and its value at length scales as small as ~ 50 pc remains unknown.

After exploring the parameter space, we have found that for a $1/r$ type radial profile of ambient density with the core density of 625 $m_{\rm H}\,{\rm cm}^{-3}$ as discussed in section 2.3.1, the best-fit parameters are $\kappa_{\rm cr} = 3\times10^{27}$ cm^2 s^{-1} and $\varepsilon_{\rm cr} = 0.1$ (upper row of figure 2.2).

The projected γ-ray luminosity (above 1 TeV) and mass profiles are shown in the 2nd and 3rd column, respectively in figure 2.2, for all three different CR injection sites. It is clear from this figure that with a proper choice of parameters, one can explain the observed values with a $1/r$ -type ambient profile. Note that we calculated the projected profiles for the whole simulation box i.e. 300 pc. If we use a simulation box of 400 pc instead of 300 pc, the γ -ray luminosity changes by $(5-7)\%$.

2.4.2.2 Injection at the shock

Next, we consider the case of CR injection at strong shocks. We mainly consider injection at the WTS as the Mach number of WTS is much larger than the forward shock (hereafter FS);

---

[1] This is the inferred CR energy density at a given projected distance.

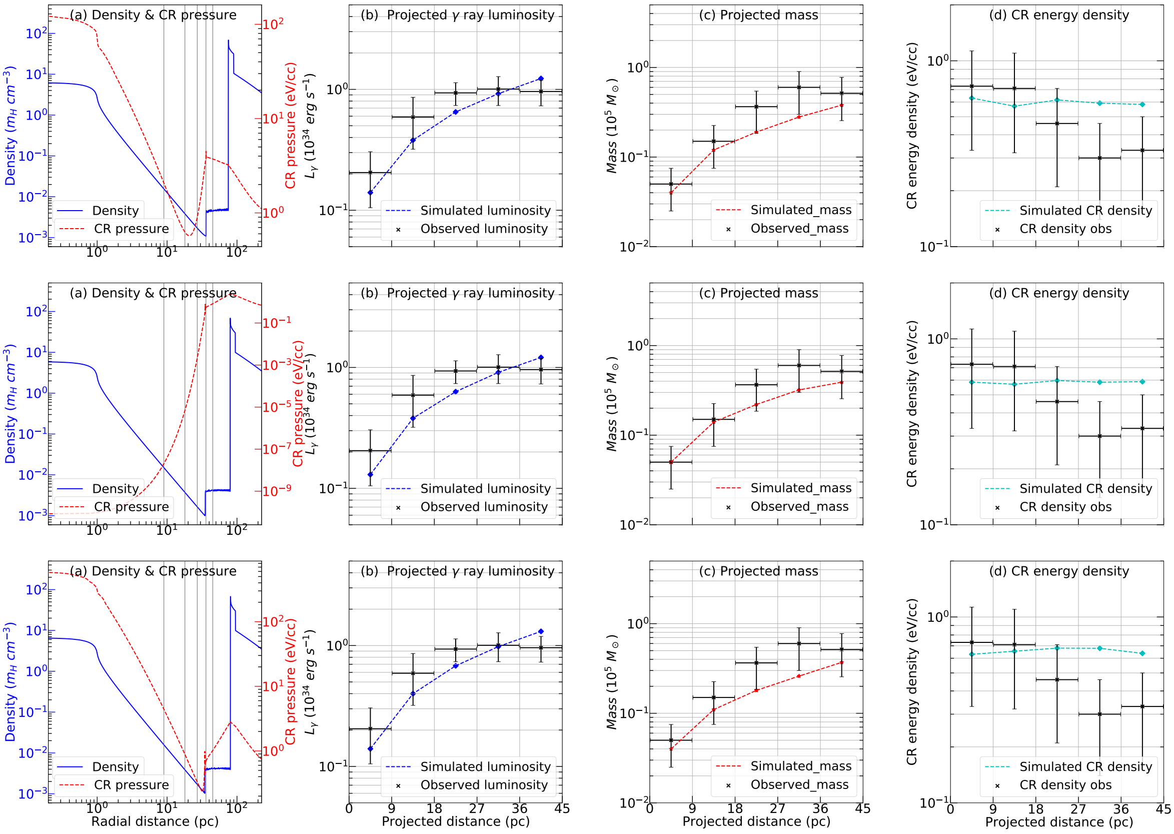

Fig. 2.2 Results of simulations with the $1/r$ ambient density profile and different injection scenarios are displayed. We plot the radial density and CR pressure profiles (a), the projected γ-ray luminosity above 1 TeV (b), projected mass (c), and inferred CR energy density above 10 TeV ($e_{\mathrm{cr,inf}}$) (d) for different injection sites of CRs. Black data points with error bars represent observational data and the blue, red, and cyan dashed lines show the simulation results for luminosity, mass, and CR density, respectively. The vertical lines in panel (a) represent different projection bins. All profiles are shown at 4.5 Myr. The uppermost row shows the case of central injection with $\kappa_{\mathrm{cr}} = 3 \times 10^{27}\mathrm{cm}^2\mathrm{s}^{-1}$ $\varepsilon_{\mathrm{cr}} = 0.1$. The middle row shows the case of shock injection with $\kappa_{\mathrm{cr}} = 10^{27}\mathrm{cm}^2\mathrm{s}^{-1}$, $w_{\mathrm{cr}} = 0.2$. The bottom row shows the case of combined injection of CRs and for $\kappa_{\mathrm{cr}} = 10^{27}\mathrm{cm}^2\mathrm{s}^{-1}$, $\varepsilon_{\mathrm{cr}} = w_{\mathrm{cr}} = 0.2$. The parameters are chosen to match the γ-ray luminosity and mass profiles in different scenarios.

i.e., WTS is stronger than FS. The efficacy of CR injection at the shocks is described by a commonly used parameter (Chevalier, 1983; Bell, 2015),

$$w_{\rm cr} = \frac{p_{\rm cr}}{p_{\rm th} + p_{\rm cr}}\,, \tag{2.28}$$

where $p_{\rm cr}$ and $p_{\rm th}$ are the CR and thermal pressures, respectively. The downstream CR pressure fraction is, therefore, $p_{\rm cr} = w_{\rm cr}\,p_{\rm tot}$ (here, $p_{\rm tot} = p_{\rm cr} + p_{\rm th}$).

After a detailed study of the parameter space, we found that the best-fit parameters that can explain the observational data are $\kappa_{\rm cr} = 10^{27}$ cm^2 s^{-1}, and $w_{\rm cr} = 0.2$ (consistent with ion acceleration efficiency found in kinetic simulations). The middle row of figure 2.2 shows the projected mass and γ-ray luminosity for these parameters. If we compare with the central injection case (uppermost panel), it is clear that shock injection requires a lower value of $\kappa_{\rm cr}$ than central injection in order to explain the observed γ-ray luminosity.

2.4.2.3 Combined injection

We also considered a CR injection scenario where CRs are accelerated in the source region as well as at the shocks. In this case of combined injection, $\varepsilon_{\rm cr}$ parametrizes the fraction of kinetic energy that goes into CRs, and $w_{\rm cr}$ decides how much of the downstream pressure is converted into CR pressure. The best-matched profiles with observations are shown in the bottom row of the figure 2.2. The corresponding value of parameters are $\kappa_{\rm cr} = 10^{27}$ cm^2 s^{-1}, and $w_{\rm cr} = \varepsilon_{\rm cr} = 0.2$. In Table 2, we have mentioned the best-fit values of parameters that can explain the observed γ-ray and mass profile.

2.4.3 Multiple discrete supernova injection

Multiple discrete supernovae (SNe) can also produce stellar wind-like structures if the frequency of supernovae is large (e.g., see Fig. 12 in Yadav et al. 2017), and we have considered this alternative as well. For this, the mechanical luminosity L_w will correspond to a kinetic energy of 10^{51} erg per SNe, multiplied by the frequency of SNe. Aharonian et al. (2019) suggested a supernova rate of 1 SN every 1000 year to support the quasi-continuous injection of CRs in the source region and to explain the observed CR density profile. However, this large rate of SNe is not realistic, because this implies $\approx 3 \times 10^4$ SNe in 30 Myr (corresponding to the main sequence lifetime of a 8 M$_\odot$ star), which would correspond to a total stellar mass of $\geq 3 \times 10^6$ M$_\odot$. Therefore, we performed simulations with a more realistic supernova injection frequency of 0.03 Myr^{-1}, corresponding to the observed cluster stellar mass of 10^5 M$_\odot$.

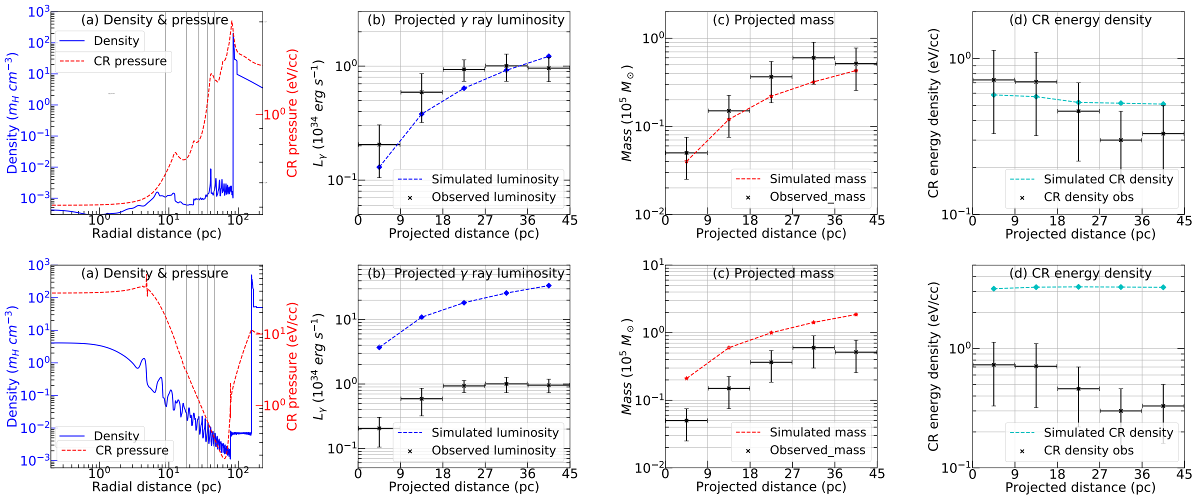

Fig. 2.3 Profiles of the density and CR pressure, projected γ-ray luminosity (> 1 TeV), mass, CR energy density above 10 TeV for the multiple discrete supernova injection scenario. CRs are injected at the shocks detected by our shock detection method. The value of $\kappa_{\rm cr} = 5 \times 10^{27}$ $\rm cm^2\,s^{-1}$ and $\varepsilon_{\rm cr} = 0.1$. Upper row: 1 supernova in every 0.03 Myr, lower row: 1 supernova in every 1000 year. Only the small supernova rate, consistent with the cluster mass, can satisfy the observational constraints. For the lower panel, we have used a uniform density of 50 $\rm m_H\,cm^{-3}$ otherwise, for a $1/r$ type ambient, the forward shock position will be at a very large distance which does not match with the observation.

Figure 2.3 shows the corresponding projected luminosity, mass, and inferred CR energy density profile for multiple supernovae. For the above-mentioned realistic SNe rate, the density profile, shown in the first panel of the upper row of figure 2.3, does not show a stellar wind-like structure (first panel of the lower row of figure 2.3), which is achieved only for a high rate of supernova (*e.g.,* 1 SN in every 1000 yr; see lower row of fig 2.3). Yet, one can get a close enough match with the projected luminosity and mass profiles. The best fit parameters for SNe rate of 0.03 $\rm Myr^{-1}$ are $\kappa_{\rm cr} = 5 \times 10^{27}$ $\rm cm^2\,s^{-1}$, $\varepsilon_{\rm cr} = 0.1$, for an $1/r$ -type ambient density. When the SNe rate is increased, the corresponding luminosity, mass, and inferred CR energy density profile much exceed the observed values. We have included this high rate of supernova just to look at the prediction of Aharonian et al. (2019) assumption. Also, for this high SNe rate, we have used a uniform ambient medium of 50 $\rm m_H\,cm^{-3}$. Instead, if we use a 1/r type ambient medium, the outer shock position will be at a large distance (beyond ~ 220 pc) which does not match the observation.

2.5 Discussion

Our simulated γ-ray luminosity and mass profiles match the observations (panels (b) and (c) of figure 2.2), for the parameter values mentioned in each case of CR injection. We also note that the inferred CR energy density offers a good match with the observed profiles, in light of the revised error bars that include the uncertainty in mass estimation (panel (d) in each row of figure 2.2). It should also be noted that our simulations are based on some simple assumptions e.g., spherical symmetry and constant diffusion coefficient. 3-D simulations can produce more realistic morphology, but those require additional free parameters such as the mass distribution of clouds and the location of stars. It is, therefore, reasonable to say that the present simulations offer a good match with the observations, in light of all the uncertainties mentioned earlier.

There are other circumstantial reasons why a flatter CR energy density profile should be considered. Recently Abeysekara et al. (2021) has shown (in their figure 2b) that for Cygnus cluster, the CR energy density above 10 TeV does not strictly follow a $1/r$ profile, and their observation does not rule out $e_{\mathrm{cr,inf}}$ being uniform, which would make it consistent with our simulation results (panel (d) in each row of figure 2.2). At the same time, the CR energy density profile for 100 GeV does follow $1/r$ profile (Aharonian et al., 2019). Abeysekara et al. (2021) interpreted this absence of a $1/r$ profile for TeV CRs on the basis of a larger diffusion rate for higher energy CRs.

The comparison of L_γ and $e_{\mathrm{cr,inf}}$ from our simulation and observations indicate that the last projected bin is observed to be less luminous than expected from the simulation. There can be a variety of reasons for this discrepancy. One possibility is that the outer shell is fragmented and porous, as in the case of 30 Doradus, for example (which allows the X-ray from the shocked wind region to be seen through the holes in the outer shell). Such a fragmented outer shell may make the γ-ray luminosity in the outer-most bin discrepant from the simulated values.

2.5.1 Time dependence of gamma-ray profiles

Figure 2.4 shows the time dependency of the γ-ray luminosity profile for combined injection of CRs. As time increases, the bubble structure expands. The luminosity in the inner bins increases with time, but the outer bin shows an opposite trend. This is because, as time progresses, the outer shock covers a more extended region, thereby increasing the effective volume of the emitting region, and increasing the luminosity in the inner bins, because of the projection effect. At the same time, the WTS and the shocked wind region gradually move out of the intermediate and outer bins, thereby decreasing the contributions in luminosity in those bins. The difference in the luminosity from 2 to 4 Myr is found to be roughly $\sim 25\%$ and within the observational margin of error.

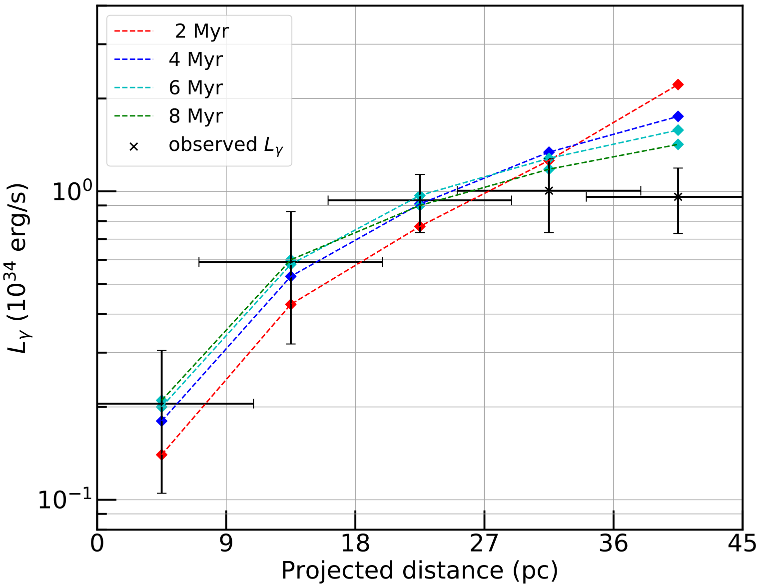

Fig. 2.4 Time evolution of γ-ray luminosity for combined injection with $\kappa_{\rm cr} = 10^{27}$ cm^2 s^{-1}, $w_{\rm cr} = \varepsilon_{\rm cr} = 0.2$. Black points are from observation.

2.5.2 Effect of thermal conduction

We have also studied the effect of thermal conduction on the simulated γ-ray profiles. We assume thermal conduction to have the Spitzer value ($\kappa_{\rm th} = 6 \times 10^{-7} T^{5/2}$ in CGS; Spitzer 1962) and also assume the saturated thermal conduction (section 4.3 of Gupta et al. 2016). For the two-fluid model, thermal conduction does not significantly change the simulated γ-ray profile, and the change in the γ-ray luminosity in each bin is $\leq (5-7)\%$.

2.5.3 Thermal X-rays

We have calculated the resulting X-ray luminosity of the (hot and dense) shocked wind region. We consider the X-ray emission due to thermal bremsstrahlung, which can be calculated using (equation 5.14b of Rybicki & Lightman 1979),

$$L_x = \int_V dV \int_\nu d\nu \left[6.8 \times 10^{-38} Z^2 n_e n_i T^{-1/2} e^{-h\nu/kT} \tilde{g_{\rm ff}} \right] \tag{2.29}$$

We take $n_e \sim n_p = P_{\rm th}/k_B T$ ($P_{\rm th}$ is the thermal pressure), $Z \sim 1$, and $\tilde{g_{\rm ff}} = 1.2$. The X-ray luminosity in $2-8$ keV for both stellar wind and multiple supernova cases is shown in figure 2.5. For the stellar wind scenario, the X-ray luminosity matches the observed value (Muno

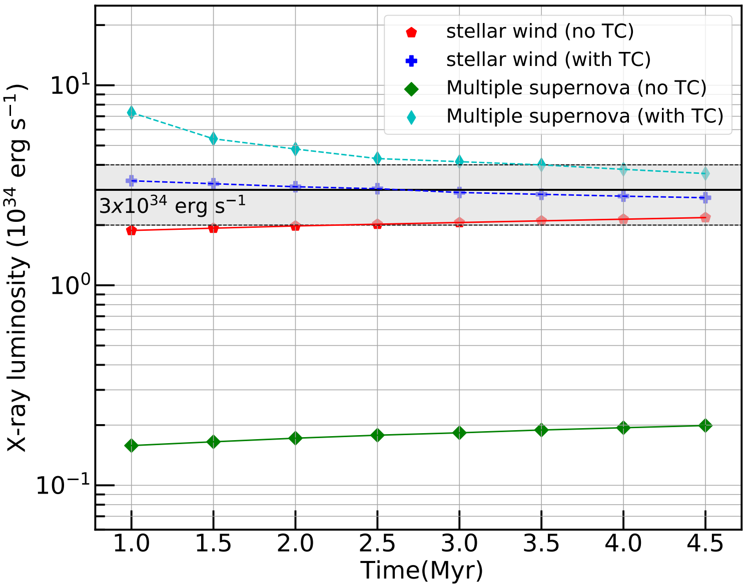

Fig. 2.5 Time evolution of X-ray luminosity ($2-8$ keV) for stellar wind case (red and blue curves) and multiple supernova case (green and cyan lines). The solid black line shows 3×10^{34} erg/s which is the obtained value from observation. The shaded region shows the range of the observed luminosity. Solid and dashed curves correspond to without TC runs and with thermal conduction runs respectively.

et al., 2006) of $(3\pm1)\times10^{34}\mathrm{erg\,s^{-1}}$ (shown by the shaded region) with or without thermal conduction. However, the corresponding X-ray luminosity for the multiple supernova injection scenario is more than one order lower in magnitude than the observed value if we do not include thermal conduction. This is due to the very low density of the gas (see figure:2.1b) inside the bubble, owing to the low SNe rate. (Higher SNe rate would recover the density structure, but overproduce γ-rays, as shown in the bottom panel of figure 2.3.) However, with thermal conduction, the simulated values (cyan curve in the plot) are close to the shaded region for this injection scenario. For this case, we have set an upper limit of the conduction coefficient, which corresponds to 10^{7}K temperature (otherwise, the stability timescale due to thermal conduction is too short). Therefore, both the stellar wind and multiple supernova injection models can explain the observed γ-ray as well as X-ray luminosity.

2.5.4 Heating due to CRs and CR energy loss

CR energy loss, due to Coulomb and hadronic interactions, can indeed be important, as estimated below. Using the expressions for Coulomb and hadronic loss in Guo & Oh (2008), the total CR energy loss rate is,

$$\Gamma_c = 7.6 \times 10^{-16} \left(\frac{n}{\mathrm{cm}^{-3}}\right) \left(\frac{e_{\mathrm{cr}}}{\mathrm{erg\,cm}^{-3}}\right) \mathrm{erg\,s}^{-1}\mathrm{cm}^{-3} \,. \tag{2.30}$$

The heating time for the gas is,

$$t_H \approx \frac{1.5nkT}{(1.65 \times 10^{-16}\, n\, e_{\mathrm{cr}})}\,\mathrm{sec}\,, \tag{2.31}$$

considering only the Coulomb interaction. Using $e_{\mathrm{cr}} \sim 0.45$ eVcm^{-3}, $T = 10^4$ K (corresponds to shell temperature), the heating time scale is $t_H \sim 10^9$ yr. This heating time is much larger than the dynamical time scale of 4.5 Myr, so the effect of this heating is negligible for the thermal gas.

However, the energy loss time scale for CRs is,

$$t_{\mathrm{cr,loss}} \approx 0.4\,\mathrm{Myr} \left(\frac{n}{50\,\mathrm{m_H\,cm}^{-3}}\right)^{-1} . \tag{2.32}$$

We can also estimate the energy loss due to CR streaming heating, for which the heating rate is given by,

$$\Gamma_{\mathrm{streaming}} = -v_A \cdot \nabla p_{\mathrm{cr}}\, \mathrm{erg\,cm}^{-3}\mathrm{s}^{-1} \,. \tag{2.33}$$

Here, p_{cr} is the CR pressure and v_A is the Alfven velocity. If we assume equipartition of magnetic and thermal energy density, then $v_A \approx 1.3 \times 10^8$ cm s^{-1}. In the absence of a measured magnetic field, assuming equipartition between magnetic and thermal energy is motivated because turbulent, dynamic systems often distribute energy equally across different components over time. In such environments, equipartition suggests that magnetic energy density $U_{\mathrm{mag}} = B^2/8\pi$ will be on the order of the thermal energy density U_{thermal}, which can help in estimating the magnetic field strength B. If we consider the region between 20–50 pc in the density plot (panel (a) of the topmost row of figure 2.2, we find that the change of CR pressure (Δp_{cr}) is $\approx 1.8 \times 10^{-11}$ dyne cm^{-2} over a distance (Δr) of 30 pc. This gives us, $\Gamma_{\mathrm{streaming}} \approx 2.6 \times 10^{-23}\,\mathrm{erg\,cm}^{-3}\mathrm{s}^{-1}$. The energy loss timescale for CR is long, but the heating time scale for the gas is ~ 0.2 Myr, (for $n \approx 0.01$ cm^{-3}). Although this may be important, we have not included streaming heating in our simulations because it will involve making assumptions about the uncertain small-scale magnetic fields.

The above discussion, especially regarding the energy loss time scale for CR (equation 2.32), shows that CR energy density in the shocked wind and outer shell can significantly decrease over the considered dynamical time scale. This process would reduce the CR energy density in these regions and consequently decrease L_γ. Therefore, L_γ would be lower than presented here, especially in the outer bins, and make the inferred CR energy density decline with the projected distance. This may result in a better match with the observations.

Our analysis shows that the diffusion coefficient ($\kappa_{\rm cr}$) lies in the range of $(5-30)\times 10^{26}$ $\rm cm^2\,s^{-1}$. Note that CR diffusion is ineffective for a much lower diffusion coefficient, whereas CRs rapidly diffuse out of the bubble without affecting it if $\kappa_{\rm cr}$ is increased (see also Gupta et al. 2018b). A comparison of the simulation results with observation implies that the γ -ray luminosity matches well if CR energy fraction $10-20\%$ of the total input energy, consistent with theoretical expectations from diffuse shock acceleration mechanisms.

Also, note that the γ-ray luminosity is a function of both gas density (n_N) and CR energy density ($e_{\rm cr}$), whereas the mass is only a function of gas density. As $e_{\rm cr}$ depends on $\kappa_{\rm cr}$, the γ-ray luminosity changes significantly with a change in the diffusion coefficient, as shown in the upper left panel of figure 2.7. In contrast, the mass profile does not strongly depend on our choice of parameters. For example, although the size of a stellar wind bubble depends on $\epsilon_{\rm cr}$, the projected mass does not change noticeably like the γ-ray luminosity for different values of $\epsilon_{\rm cr}$.

2.5.5 Comparision of cosmic ray pressure & gas pressure

In figure 2.6 we have shown the CR pressure and the thermal pressure for different injection scenario. For the central and combined injection, the CR pressure has a significant value inside the star cluster, however for the shock injection the CR pressure is very low in the central region of the cluster. This is because for shock injection CR are accelerated in the shock and then diffuse inside from the accelerating region so the CR pressure is high at the shock and then decreases inside of the cluster. On the other hand for central and combined injection CR acceleration is happening in the central region also and from there those particles diffuse outward of the cluster so we get a significant amount of CR pressure in the central region. Although the gas pressure dominates inside the cluster, the CR pressure and thermal pressure are comparable outside of the cluster.

2.5.6 Dependence on various parameters

We have studied the dependence of our results on different parameters, *viz.*, the diffusion coefficient, and the injection parameters.

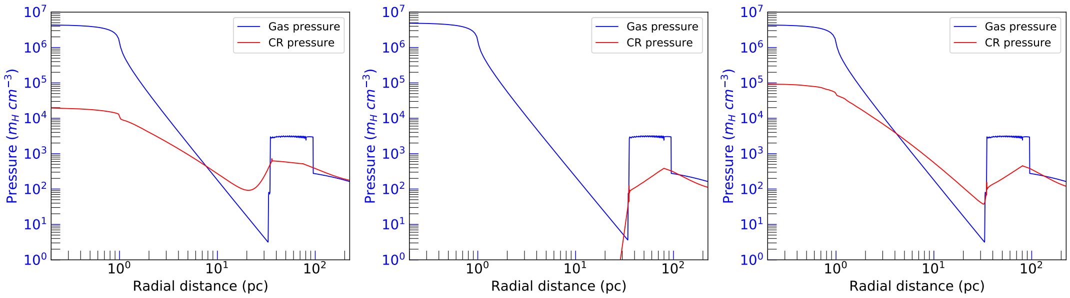

Fig. 2.6 Gas pressure and CR pressure for *left*: central injection, *middle*: shock injection, *right*: combined injection scenario.

2.5.6.1 Diffusion coefficient ($\kappa_{\rm cr}$)

To understand the effect of colorred the diffusion coefficient on the γ-ray profile, we also ran the simulations for different values of the diffusion coefficient, keeping a constant $\epsilon_{\rm cr} = w_{\rm cr} = 0.2$. The upper left and right panel of figure 2.7 respectively show the variation of γ-ray luminosity and CR density with distance for different values of $\kappa_{\rm cr}$. It is clear from the upper left panel of the same figure, that the γ-ray luminosity exceeds the observed values for a lower value of diffusion coefficient. This is because a slower diffusion of CRs implies a higher density of CRs in the vicinity of the cluster, which increases the γ-ray luminosity.

The upper left panel of figure 2.7 shows the corresponding variation of the inferred CR energy density profile with $\kappa_{\rm cr}$. As expected, increasing the diffusion coefficient depletes the injection region of CRs, and the resulting drained CR energy density profile is naturally decreased. However, our exercise selects the range of $\kappa_{\rm cr} \approx (5\text{–}100) \times 10^{26}$ cm^2 s^{-1} as the appropriate one since the observed values are bracketed from both sides in this range, as seen from the upper left and upper right panels of figure 2.7. We note that this range of $\kappa_{\rm cr}$ is consistent with previous estimates from observations of γ-rays in star clusters (Gabici et al. 2010; Giuliani et al. 2010; Li & Chen 2010; Ackermann et al. 2011).

2.5.6.2 Injection parameter ($w_{\rm cr}$ & $\epsilon_{\rm cr}$)

We have also run the simulations for different values of the injection parameter ($w_{\rm cr}$ and $\kappa_{\rm cr}$) keeping a constant diffusion coefficient $\kappa_{\rm cr} = 10^{27}$ cm^2 s^{-1}. The lower-left and right panel of figure 2.7 respectively show the variation of γ-ray luminosity and CR density with distance for different injection parameters. It is clear from the lower-left panel of the figure that an increasing value of $w_{\rm cr}$ or $\epsilon_{\rm cr}$ increases the γ-ray luminosity because a larger injection parameter means a larger fraction of kinetic energy being deposited into CRs which consequently increases

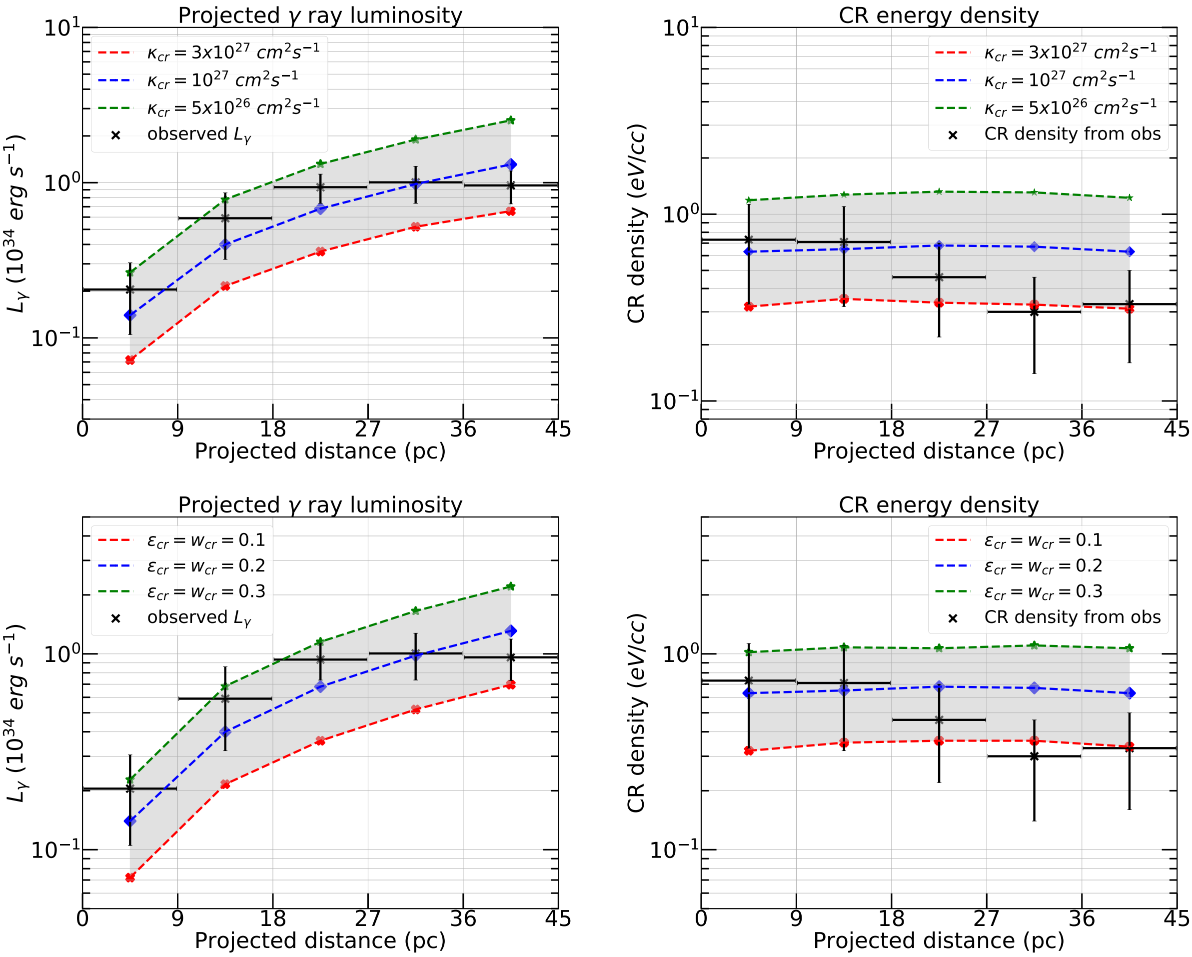

Fig. 2.7 The projected γ-ray luminosity and inferred CR energy density profiles as a function of the projected radius for different injection parameters and diffusion parameters for the case of combined CR injection scenario. In all panels, black points with error bars indicate the observational values. The upper left and right panels show the variation of the γ-ray luminosity and inferred CR energy density for different $\kappa_{\rm cr}$, respectively for a fixed $w_{\rm cr} = \varepsilon_{\rm cr} = 0.2$. The lower left panel shows the variation of the γ-ray profile with varying CR injection parameters and the lower right panel shows the variation of the projected inferred CR energy density profile with varying injection parameters. For the lower two panels the value of $\kappa_{\rm cr} = 10^{27}$ cm^{2}s^{-1}.

the γ-ray luminosity in the close vicinity of the cluster. The corresponding CR density profile is shown in the lower right panel of figure 2.7.

2.6 Conclusions

We have studied the implication of the recently inferred distribution of CR energy density in massive compact star clusters, taking the particular example of Wd1. With 1-D two-fluid hydro-dynamical simulation for stellar wind in star clusters, we have studied the projected γ-ray luminosity, mass, and CR energy density for the Wd1 cluster and their dependence on diffusion coefficient, injection parameter, and ambient density. Our findings are as follows:

1. The most important takeaway from our analysis is that the inferred $1/r$ profile of CR energy density need not reflect its true radial profile. Also, we have shown that even the observed data can accommodate a flatter CR energy density profile, in light of revised error estimates. We have shown that dividing the projected L_γ by the projected mass in different annuli can yield a CR energy density profile that is significantly different from the actual profile. We have also pointed out various uncertainties that would make a straightforward inference difficult, *e.g.*, the lack of morphological symmetry, and the uncertainty in the mass estimate.

2. While a $1/r$ profile for the CR energy density allows a simple explanation in terms of a steady-state CR luminosity at the center of the cluster, which makes it appealing, we have studied the more plausible scenarios, that of a time-varying CR luminosity, or CR being injected outside the central region (in the WTS, for example), and showed how these scenarios are also consistent with observations. We can not rule out any of the CR acceleration sites on the basis of these observations because the observed luminosity and mass profile can be explained by all three CR injection methods, as well as the discrete supernova scenario by appropriate choice of the diffusion coefficient and injection parameters.

3. The parameters for the best match with observations are not ad-hoc, but are supported by independent arguments. For example, a lower value of diffusion coefficient (10^{27} cm^2 s^{-1}) can explain the observation for shock injection case, while for central injection a higher value (3×10^{27} cm^2 s^{-1}) is required. These values for the diffusion coefficient are consistent with previous findings. The same goes for the parameter describing the efficiency of CR energy injection, which is found to be in the range $\epsilon_{\rm cr}/w_{\rm cr} \sim 0.1$–$0.3$, consistent with previous works (Gupta et al., 2018b).

4. The discrete multiple supernova injection scenario can explain the γ-ray observation with the appropriate choice of parameters. On the other hand, the simulated X-ray luminosity (assuming it to be thermal) is close to the observed value only if we include thermal conduction.

3

Cosmic rays from a distribution of star clusters: potential second Galactic cosmic ray component:

Based on:

"Between the Cosmic-Ray 'Knee' and the 'Ankle': Contribution from Star Clusters", **Bhadra, S.**, Thoudam, S., Nath, B., Sharma P., The Astrophysical Journal, **961**, 215, 2024.

(Bhadra et al., 2024)

We demonstrate that massive young star clusters represent potential candidates capable of accelerating Galactic CRs within the range of 10^7 *to* 10^9 *GeV (between the 'knee' and 'ankle' energies). Various plausible scenarios, including acceleration at the wind termination shock (WTS) and supernova shocks within these clusters, have been proposed. However, achieving particle acceleration in the* 10^7 *to* 10^9 *GeV range poses challenges within the standard paradigm of CR acceleration in supernova remnants. To address this, we propose a model for the production of various nuclei in CRs from massive stellar winds, leveraging the observed distribution of young star clusters in the Galactic plane. Additionally, we conduct a comprehensive calculation of CR transport in the Galaxy, accounting for diffusion effects, interaction losses during propagation, and particle re-acceleration by aged supernova remnants, to determine the all-particle CR spectrum. By applying the Hillas criterion to estimate the maximum energy attainable inside a young massive star cluster, we contend that such clusters can accelerate protons up to several tens of PeV.*

Main result

- We propose that the 'second Galactic component of CRs', essential for explaining the observed flux of CRs within the range spanning from the 'knee' to the 'ankle' (from 10^7 GeV to 10^9 GeV), could originate from a distribution of massive star clusters. This component serves to connect the gap between the CRs derived from supernova remnants dominating below approximately 10^7 GeV and the extragalactic component, which prevails above roughly 10^9 GeV.

- Previously, it has been observed that SNR-CRs and CRs stemming from star clusters should not necessarily be viewed as distinct entities. Instead, they may emerge from similar sources, specifically massive star clusters. The less massive clusters may give rise to individual supernova remnants (SNRs) and SNR-CRs, whereas the more massive ones have the potential to accelerate CRs through various strong shocks occurring within the dense cluster environment.

- We have presented the possibility of proton acceleration to energies reaching several tens of PeV, by examining particle acceleration processes occurring at the WTS and through shocks generated by supernova remnants (SNRs) within massive star clusters.

3.1 Introduction

In the previous chapter we showed a particular star cluster WD1 acts as a particle accelerator. In this chapter, we consider a distribution of such clusters in our Galaxy and try to understand their total contribution to the observed all-particle cosmic ray (CR) spectra. As mentioned already, lower energy CRs up to $\sim 10^{5-6}$ GeV are believed to be accelerated by supernova shocks (Lagage & Cesarsky 1983a; Axford 1994). This dominant acceleration mechanism, revealed by both theoretical (Fermi, 1949; Axford et al., 1977; Bell, 1978; Blandford & Ostriker, 1978; Blasi, 2013) and observational studies (Drury et al., 1994; Ackermann et al., 2013; H. E. S. S. Collaboration et al., 2018c), is diffusive shock acceleration (DSA), a first-order Fermi acceleration process in which $\sim 10\%$ of the shock energy is expected to be converted to CRs. Although the acceleration mechanism continues to work throughout the active stage of a supernova remnant (SNR) until it becomes indistinguishable from the ambient interstellar medium after $\sim 10^5 - 10^6$ years, most of the particle acceleration occurs during the un-decelerated blast wave phase, which lasts for $\leq 10^3$ years (Lagage & Cesarsky, 1983a). This limits the maximum CR energy that can be accelerated in SNRs because the acceleration time of CRs cannot be longer than the age of the SNR (Morlino, 2017). Considering nonlinear effects such as the scattering of the CRs by the waves they generate themselves and assuming the magnetic flux density of the interstellar magnetic field to be $\sim \mu$G, Lagage & Cesarsky (1983a) estimated the upper limit of CR energy in supernova remnants to be $\sim 10^5$ GeV per nucleon.

Preliminary observations seem to align with these theoretical concepts. Suzuki et al. (2022) reported cutoff energy of around TeV from γ-ray observations of 15 supernova remnants. Recently, LHAASO (Large High Altitude Air Shower Observatory), and Tibet air shower observations have identified a number of PeVatron candidates (Cao et al. 2021; Tibet ASγ Collaboration et al. 2021), which may include a few SNRs. These theoretical and observational developments suggest cutoff energy in the range $10^5 - 10^6$ GeV for SNRs. At the high-energy end, CRs above $\sim 10^9$ GeV are considered to have an extragalactic origin, possibly originating from galaxy clusters (Kang et al., 1996), radio galaxies (Rachen & Biermann, 1993), AGN jets (Mannheim et al., 2000) or gamma-ray bursts (Waxman, 1995).

There is a gap between the contribution from SNRs and the extragalactic component, which lies in the range of $\sim 10^7 - 10^9$ GeV, the region between the so-called ‘knee’ and ‘ankle’ (also known as the ‘shin’ region). To explain this gap in the all-particle CR spectrum, a few models have been proposed in the literature. Biermann & Cassinelli (1993); Thoudam et al. (2016) have discussed the explosion of Wolf-Rayet stars embedded in the wind material from the same stars as a potential acceleration site of CRs in the range of $\sim 10^7 - 10^9$ GeV. However, there may be some problems with this scenario. A uniform distribution of Wolf-Rayet stars in the Galaxy was assumed, which is unrealistic. Moreover, there are many uncertainties in the crucial parameter of the magnetic field of the Wolf-Rayet stars. For a proton cutoff energy of 1.1×10^8 GeV, the surface magnetic field of a Wolf-Rayet star is required to be $\approx 10^4$ G in this model (Thoudam et al., 2016), while realistic predictions for the same are in the range of a few hundred G (Neiner et al., 2015; Blazère et al., 2015). Although no direct magnetic signature has been detected in any of the Wolf-Rayet stars, using Bayesian statistics, Bagnulo et al. (2020) have estimated their surface magnetic fields to be of the order of a few kiloGauss.

The idea of Galactic WTS to accelerate high-energy CRs also has problems. The effect of Galactic winds on the transport of CRs in the Galaxy has been discussed in detail (Lerche & Schlickeiser 1982; Strong & Moskalenko 1998; Jones et al. 2001; Breitschwerdt et al. 2002). Following these developments, Jokipii & Morfill (1987); Zirakashvili & Völk (2006); Thoudam et al. (2016) introduced these CRs originating from Galactic WTS as the possible candidate for the 'second' (between 'knee' and 'ankle') component of Galactic CRs. The CRs originating from the Galactic wind (GW-CRs) are believed to mostly contribute to the higher energy range. This is due to the increasing effect of advection over diffusion at lower energy, preventing particles from reaching the Galactic disk. Higher energy particles, which diffuse relatively faster, can overcome the advection and reach the disk more effectively. Thoudam et al. (2016) have used a distance of ~ 100 kpc for the Galactic WTS. Bustard et al. (2017) have argued that in order for the CRs to reach 10^8 GeV, either the outflow speed needs to be of order ~ 1000 km s^{-1} or the magnetic field needs to be amplified. However, realistic simulations of outflows from Milky Way-type galaxies do not find signatures of such strong outflows/shocks. Sarkar et al. (2015) showed that the outer shock due to the Galactic wind weakens and continues to propagate as a sound wave through the circum-galactic medium. The termination shock remains confined within $\lesssim 10$s of kpc and disappears after the mechanical power is stopped being injected. Also, the observed nuclear abundances suggest lighter nuclei in contrast to the expectation from the Galactic wind model in the $10^7 - 10^9$ GeV energy range. Thus, this model has been disfavoured. In order to explain the observed all-particle spectrum in the range $10^7 - 10^9$ GeV, an appropriate model of CRs is still required.

Coming back to the DSA mechanism of CR acceleration in supernova shocks, this standard scenario is known to bear several problems (e.g., Gabici et al. 2019). The acceleration scenario cannot explain some of the observed features of CRs like excess of Ne^{22}/Ne^{20} in CRs compared to standard cosmic abundances in ISM (Wiedenbeck et al. 1999), proton acceleration up to greater than PeV (10^6 GeV) energy range, and so on. Various additional CR acceleration sites are reported in the literature to solve these paradigms; young massive star clusters are one of those other possible sources of CRs in our Galaxy (Bykov, 2014; Knödlseder, 2013; Aharonian et al., 2019). Recently, the γ-ray observations by LHAASO, HESS, Fermi-LAT, and

HAWC have provided evidence of CR acceleration up to very high energy in a few massive star clusters like Westerlund1 and Cygnus (Aharonian et al., 2019; Abeysekara et al., 2021). These star-forming regions have been discussed as potential candidates for CR accelerators (e.g. Bykov 2014); these γ-ray observations have strengthened the hypothesis of CR acceleration in these environments. Recently, Gupta et al. (2020) has shown that the excess (^{22}Ne/^{20}Ne) ratio can be explained by considering WTS (WTS) of massive star clusters as CR accelerators. Recently, Tatischeff et al. (2021) showed that the refractory elements of Galactic CRs are produced in super-bubbles. This theoretical and observational evidence prod us to study the total contribution of CRs originating from the distribution of massive star clusters in our Galaxy.

Star clusters, which are the birthplace of massive stars (that ultimately explode as SNe), give rise to continuous mass outflow in the form of stellar wind. These are mainly located in dense molecular clouds and weigh of the order of several thousand solar masses. Star clusters host massive stars as well as supernova explosions, which produce a low-density bubble around them (Weaver et al., 1977; Gupta et al., 2018b). Young star clusters contain sufficient kinetic energy supplied by interacting stellar winds, which can accelerate protons up to $\sim 10^7$ GeV. Considering heavier nuclei, this cosmic ray component originating from star clusters can, therefore, be considered as the second component of Galactic CRs, which can explain the observed all-particle spectrum in the energy range of $10^7 - 10^9$ GeV. Bhadra et al. (2022), using hydrodynamic simulation, showed that the observed distribution of γ-rays can be explained by invoking cosmic ray acceleration in the Westerlund1 cluster.

Following the above discussion, it is clear that: (1) Galactic supernovae can accelerate particles up to a few times 10^6 GeV energy, and (2) extragalactic components can explain the all-particle spectrum above $\sim 10^9$ GeV energy. The gap in the energy range cannot be explained using only these two components, and we require another Galactic component to explain the observed data in the range $10^7 - 10^9$ GeV. Our main focus in this work is the second component of Galactic CRs. In this regard, we propose CR contribution from the population of massive star clusters as a source of the observed all-particle CR spectrum in the range $\sim 10^7 - 10^9$ GeV. This may act as a bridge between the SNR component and the extragalactic component and fill the gap in the desired energy range.

We begin with some basics in Section 3.2. The details of our proposed model are described in Section 3.3. In Section 3.4, we present our results, and in Section 3.5 we compare our model with other models. In Section 3.6, we consider various models for the extragalactic CR component. This is followed by further discussion in Section 3.7 and a conclusion in Section 3.8.

3.2 Existing components of Cosmic rays

3.2.1 First Galactic component: SNR-CRs

As mentioned in the Introduction, SNRs are likely candidates for cosmic-ray acceleration up to $\sim 10^6$ GeV energy (Lagage & Cesarsky, 1983a). The diffusive shock acceleration at strong forward shocks produces a power-law spectrum with an index of ~ -2 (Bell 1978; Blandford & Ostriker 1978; Caprioli et al. 2011). We have adopted the model of Thoudam et al. (2016) for the CR component from Galactic supernova remnants (SNR-CR component). After the acceleration in the strong shock of supernova remnants, CR particles escape the remnants and propagate through the interstellar medium via diffusion. Initially, this shock moves with a very high velocity so that the match number of the shock remains high in that period. We focus on the forward shock in SNR because most of the discussion in cosmic ray literature deals with the forward shock although some papers have discussed the contribution of reverse shock in this regard (Pohl et al., 2011). The CR particles can be re-accelerated repetitively by expanding supernova remnant shock waves already existing in the interstellar medium during their propagation. These shocks are mainly produced by older remnants and are relatively weak.

We use the same contribution of the SNR-CR component as presented in Thoudam et al. (2016). Their calculation assumes an exponential cutoff for the proton source spectrum at $E_c = 2.5 \times 10^6$ GeV. This value has been chosen by fitting the observed all-particle spectrum. The maximum energy of SNR-CRs corresponds to the cutoff energy of iron nuclei, which is $26 \times E_c = 6.5 \times 10^7$ GeV. This result shows that SNR-CRs can contribute only $\sim 30\%$ of the total observed intensity above $\sim 2 \times 10^7$ GeV (Thoudam et al., 2016). Therefore, additional components are required to explain the all-particle spectrum in the $\gtrsim 10^7$ GeV range.

3.2.2 Extragalactic component

Various previous works have already pointed out that the 'ankle'-like feature of the CR spectrum at $\gtrsim 10^9$ GeV can be explained if we consider the propagation effects of the extragalactic component (mainly proton) in the evolving microwave background (Hillas, 1967; Berezinsky et al., 2006; Aloisio et al., 2012). We consider two different models for the extragalactic component: the 'UFA model' (Unger et al., 2015) and a combination of minimal (di Matteo 2015), and PCS model (Rachen 2015; Thoudam et al. 2016). We refer to this combined model as the 'MPCS' model. These different models will be explained in greater depth in the below sections.

Unger et al. (2015) considers acceleration of energetic nuclei at the shocks associated with gamma-ray bursts or tidal disruption events, and photo-disintegration of these particles in the photon background present inside the source region. In this model, only the highest energy particles having an escape time shorter than the photo-disintegration time can escape the source region leading to a strong proton component in the energy region below the ankle. We call this the 'UFA' model of the extragalactic component. In addition to the all-particle CR spectrum, data of the primary composition in the ultra-high energy range have become available in the last few years.

The 'minimal model' has been derived from CR composition measured by the Pierre Auger Observatory (di Matteo 2015) and assumes uniformly distributed sources in a comoving volume that produce a power-law cosmic ray spectrum with some cutoff at a particular rigidity R_c (rigidity is defined as Apc/Ze, where A/Z is nuclear mass/charge and p is momentum, e the charge of the electron, and c is the speed of light in vacuum). Above $\sim 3\times10^{10}$ GeV, the spectrum exhibits a steep cut-off that is mainly due to the intrinsic cut-off in the injection spectrum (di Matteo, 2015), and not due to the GZK absorption (Zatsepin & Kuz'min, 1966) during the propagation.

The PCS (primordial cluster shock) model is based on the universal scaling argument. It takes into account the acceleration of primordial proton and helium mixture by primordial cluster shocks, which are mainly the accretion shocks expected from clusters of galaxies during the structure formation. In this scenario, the acceleration of CR particles is limited by losses due to pair production in the CMB. This component is not expected to reach ultra-high energies. Consequently, the minimal model plus the "primordial cluster component" was introduced by Rachen (2015), where the acceleration of heavy nuclei at shocks of gamma-ray bursts or in tidal disruption events are considered.

3.3 Second Galactic component: cosmic rays from star clusters

The all-particle cosmic ray spectrum has two main features: a steepening of the spectral index from -2.7 to -3.1 at about 3 PeV, commonly known as the 'knee', and a flattening back to -2.7 at about 4×10^9 GeV, generally known as the 'ankle'. Therefore, we need to assume a cut-off in the Galactic component immediately below the 'ankle' to explain the observed spectrum. This is a 'second knee' feature in the CR spectrum. For a typical magnetic field of 3 μG in the Galaxy, CRs with energy Z $\times10^8$ GeV have a Larmor radius of $36/Z$ pc, which is much smaller than the extent of the diffusion halo of the Galaxy. This implies that CRs with the energy around the second knee remain confined within the Galaxy for some time before escaping the Galaxy. This also suggests the observed cut-off at this energy is due to some CR accelerators different from SNRs, as the latter accelerate particles only up to a few 10^6 GeV.

In the following, we discuss one potential scenario of another Galactic component of CRs: the acceleration of CRs by the young massive star clusters, which we briefly mentioned in Section 3.1. It has especially been speculated that the winds of massive stars may be a suitable location for the acceleration of CRs (Cesarsky & Montmerle 1983; Webb et al. 1985; Gupta et al. 2018b; Bykov et al. 2020). CRs can be accelerated in the fast stellar wind of star clusters, and in particular, two scenarios can be important. Firstly, CR acceleration in the WTS (WTS) (Gupta et al., 2018b), and secondly, acceleration by supernova shocks embedded in the stellar winds (Vieu et al., 2022). Those CRs accelerated in young star clusters with age ≤ 10 Myr can contribute significantly to the observed total flux of CRs (Gupta et al., 2020). Recently LHAASO has observed γ-rays in the PeV energy range from young massive star clusters (Cao et al., 2021), which can be associated with cosmic ray acceleration in those clusters.

Figure 1.12 shows a schematic diagram of a stellar wind bubble around a compact star cluster. There are several distinct regions inside the bubble, such as (a) the free wind region, where the stellar wind originating from the source expands adiabatically, (b) the wind termination shock (WTS), (c) the shocked wind region containing slightly denser gas, and (d) the outermost dense shell containing the swept-up ambient gas. CRs can be accelerated in the central region as well as in the shocks of the cluster. After getting accelerated to very high energy, CRs will diffuse outward from the source into the ISM.

3.3.1 Distribution of star clusters in Galactic plane

Star clusters are distributed all over the Galactic plane, and each star cluster creates a superbubble-like structure around itself (Weaver et al., 1977; Gupta et al., 2018b). Bronfman et al. (2000) observed 748 OB associations across the Galactic disk and found their distribution to peak at $R_p = 0.55\,R_0$, ($R_0 = 8.5$ kpc is the solar distance from the Galactic center). We find that their inferred (differential) star cluster distribution can be roughly fitted by

$$dN_c(r) = \Sigma_0\, e^{\frac{-(r-R_p)^2}{\sigma^2}}\, 2\pi r\, dr, \tag{3.1}$$

where r is the Galactocentric distance and $\sigma = 3$ kpc and Σ_0 is the normalization constant in the unit of kpc^{-2}. This denotes the number of star clusters in an annular ring of radius r to $r+dr$. The surface density of the clusters can be obtained by dividing this number by the surface area of the annular ring $(2\pi r\,dr)$, as

$$\nu(r) = \Sigma_0\, e^{\frac{-(r-R_p)^2}{\sigma^2}} \tag{3.2}$$

where, $\Sigma_0 \sim 14$ kpc^{-2} (Nath & Eichler, 2020). We have used a minimum number of 10 and a maximum number of 1000 OB stars in a cluster (these are somewhat arbitrary, and we later discuss the impact of these choices). In this distribution, we miss the sources of the central molecular zone. One should note that the primary CRs observed at the Earth are accelerated from sources located within a short distance which is of the order of the vertical halo height H (Taillet & Maurin, 2003; Thoudam, 2008). Hence, the CRs from the Central Molecular Zone (CMZ) of the Milky Way likely have very limited influence at Earth's location. Although the CMZ produces high-energy CRs due to active star formation, supernovae, and strong magnetic fields, the majority of these particles lose energy or are deflected by magnetic fields as they travel through the Galaxy. By the time they reach the solar neighborhood, their intensity is substantially reduced. The dominant CRs observed at Earth are instead thought to come from more nearby sources.

The actual distribution of cosmic ray sources is expected to follow the distribution of young stars and dense gas in the form of a spiral structure, for instance, as traced by the FIR luminosity (Bronfman et al., 2000), or the Ly-α radiation (Higdon & Lingenfelter, 2013), which show a bit of asymmetry and trace the spiral arms to some extent. We emphasize that although we assume an axisymmetric source distribution with smooth radial distribution, this assumption yields a spectrum for cosmic-ray protons/nuclei that closely resembles that derived from the spiral-arm feature of the source distribution (e.g., Werner et al., 2015). Beyond ~ 10 GeV, Werner et al. (2015) show that the spectrum's shape remains largely unchanged and flux varies by less than 2% when spiral-arm features are introduced. However, it is worth noting that the presence of nearby star clusters associated with spiral arms can introduce noticeable effects on cosmic-ray anisotropy at Earth. This is an important topic for future investigation but beyond the scope of this work.

3.3.2 Transport of CRs originating from star clusters in the Galaxy

After getting accelerated in SNR and star cluster shocks, CRs propagate through the Galaxy. This propagation is mainly dominated by diffusion and energy loss due to interaction with ISM material. Some fraction of the propagating CRs can be re-accelerated up to higher energy by the interaction with existing weaker shocks that have been generated from older supernova remnants in the ISM. This process has been discussed in detail in Thoudam & Hörandel (2014).

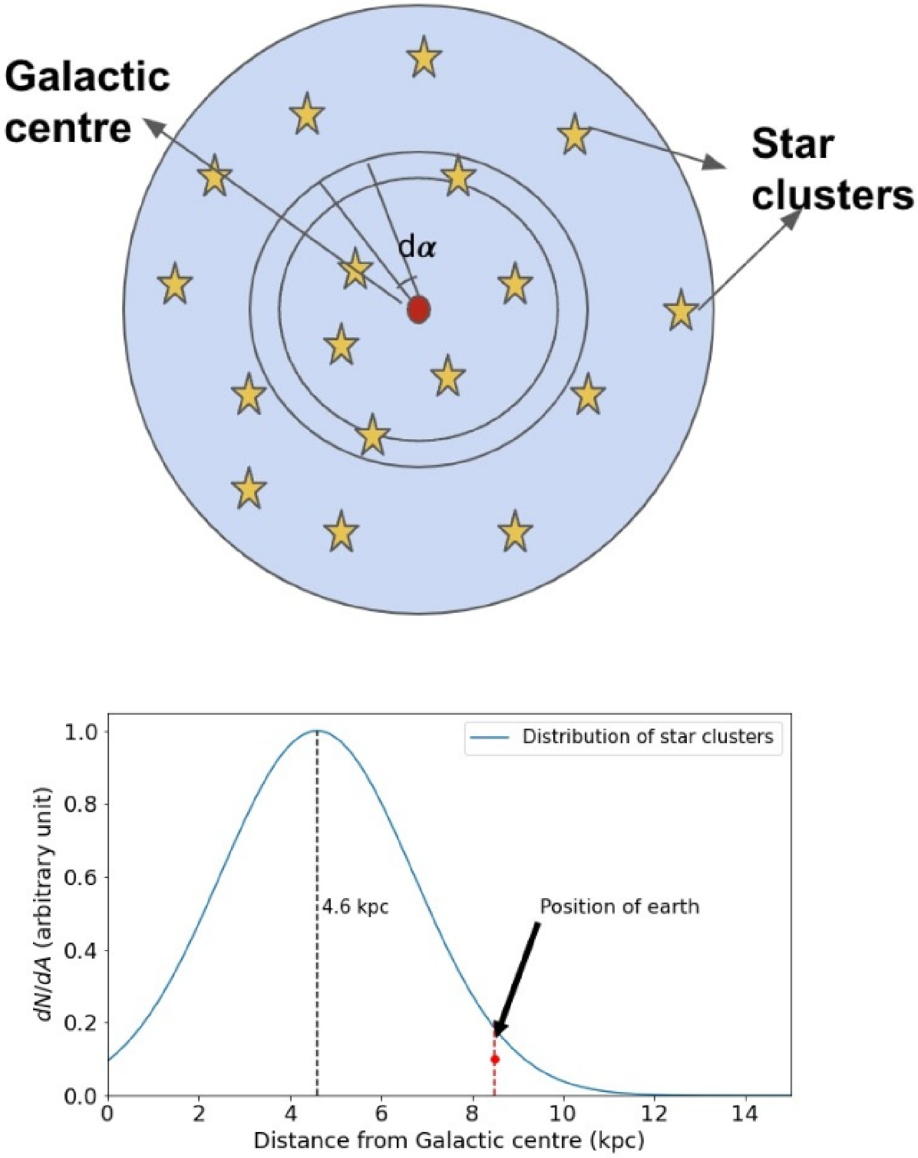

Fig. 3.1 Top: Schematic distribution of star clusters in the Galactic plane (face-on view), each star indicates a star cluster on the plane; bottom: the surface density (number per area) of star clusters (Σ; see Eq. 3.2) as a function of distance from the Galactic center.

The transport equation for cosmic ray nuclei in a steady state can be written as

$$\nabla \cdot (D\nabla N) - [nv\sigma + \zeta]\delta(z)N + \left[\zeta s p^{-s} \int_{p_0}^{p} du N(u)\, u^{s-1}\right]\delta(z) = -Q(r,p)\delta(z). \tag{3.3}$$

Here we include spatial diffusion (first term on the left-hand side), re-acceleration (terms with coefficient ζ), and interaction losses ($\propto \sigma$, the loss cross-section) of the CR particles, as mentioned above. The diffusion coefficient $D(p)$ depends on the momentum of CR particles. Here n represents the averaged surface density (number density per unit area) of interstellar atoms in the Galaxy, $v(p)$ is the CR particle velocity, $\sigma(p)$ is the cross-section of inelastic collision, N is the differential number density (number per unit volume per momentum) and ζ is the rate of re-acceleration. The third term involving the momentum integral represents the generation of higher energy particles via the re-acceleration of lower energy particles by the weak shocks of older SNRs. It actually represents the gain in the number of particles due to re-acceleration from lower energies. It has been assumed that a CR population is instantaneously re-accelerated to form a power-law distribution with an index s. As weaker shocks generate a softer particle spectrum, the resulting re-accelerated component will have a spectrum steeper than the initial cosmic-ray source spectrum produced by strong shocks. We assume an index of $s \sim 4.5$ in line with Thoudam & Hörandel (2014). We consider a cylindrical geometry for the diffusion halo denoted by the radial coordinate r and vertical direction z. The diffusive halo has upper and lower boundaries at $z = \pm H$ and a radial boundary at 20 kpc. A significant fraction of CRs that reach the earth is produced from those sources located within a distance $\sim$ 5 kpc (Taillet & Maurin, 2003).

The term on the right side, $Q(r,p)\delta(z)$, represents the injection rate of CRs per unit volume in the momentum bin $[p, p+dp]$ by the sources. The $\delta(z)$ term denotes that all sources are confined to the Galactic plane $z = 0$. Similarly, re-acceleration and loss regions are confined within the Galactic mid-plane.

The injection term $Q(r,p)$ can be written as a combination of a space-dependent part and a momentum-dependent part, i.e.,

$$Q(r,p) = \nu(r)\, H[R-r]\, H[p-p_0]\, Q(p), \tag{3.4}$$

where $\nu(r)$ (see equation 2) represents the number of star clusters per unit surface area on the Galactic disk (see section 3.3.1 for details), $H[t] = 1(0)$ for $t > 0(<0)$ is the Heaviside step function, and p_0 (which is the lower limit in the integral in Equation 3.3) is the low-momentum cutoff introduced to approximate the ionization losses. Wandel et al. (1987) showed that the ionization effects could be taken into account if we truncate the particle distribution below $\sim$ 100 MeV/nucleon. In our calculation, we introduce a low-energy cutoff of 100 MeV/nucleon.

Our assumed distribution of star clusters, motivated by observations, has a peak at ~ 4.6 kpc ($0.55R_0$, where R_0 is the distance of the Earth from the Galactic center ~ 8.5 kpc) and then decreases rapidly at large distances.

The expression for surface density of star clusters ν has been calculated in section 3.3.1, and the power-law source spectrum is described in section 3.3.3. The energy-dependent diffusion coefficient as a function of particle rigidity follows

$$D(\rho) = D_0 \beta (\rho/\rho_0)^{\delta}, \tag{3.5}$$

where D_0 is the diffusion constant, $\rho = Apc/Ze$ is the particle rigidity, $\beta = v(p)/c$ where $v(p)$ is the CR particle velocity and c is the speed of light, $\delta = 0.33$ is the diffusion index, and $\rho_0 = 3$ GV is a normalisation constant.

In this injection-diffusion-reacceleration[1] model, the rate of reacceleration depends on the rate of supernova explosions and the fractional volume occupied by SNRs in the Galaxy. The reacceleration parameter ζ can be expressed as, $\zeta = \eta V \nu_{SN}$, where $V = 4\pi\mathfrak{R}^3/3$ is the volume occupied by each SNR of radius $\mathfrak{R}$ re-accelerating the CRs. Here, η is a correction factor that takes care of the actual unknown size of the remnants, and ν_{SN} is the rate of supernova explosions per unit surface area in the Galactic disk. The values of $\mathfrak{R}$ and ν_{SN} have been taken as 100 pc and 25 SNe $\mathrm{Myr}^{-1}\mathrm{kpc}^{-2}$ respectively (Thoudam & Hörandel, 2014).

The solution of equation 3.3 can be obtained by invoking the Green's function method and by considering the two separate transport equations for the regions below and above the Galactic disk ($z < 0$ and $z > 0$ respectively), and by connecting the two solutions at Galactic plane, i.e., $z = 0$, via a jump condition. Following this procedure one can get the Green's function $G(r, r', z, p, p')$ (equation A.20 of Thoudam & Hörandel 2014). After convolving the obtained Green's function with the assumed source distribution and integrating it over the Galactic plane, one can get the final solution (see equation 6 of the same paper) for the CR density $N(r, z, p)$. Following the procedure described in Thoudam & Hörandel (2014), we get the solution of the transport equation 3.3 as

$$N(r,z,p) = 2\pi \int_0^{\infty} dp' \int_0^{\infty} r'dr'\, G(r,r',z,p,p')\, Q(r',p'). \tag{3.6}$$

Substituting the obtained $G(r, r', z, p, p')$ (Thoudam & Hörandel, 2014) and the assumed source distribution in the above equation, the cosmic ray density at the Earth ($r = 8.5$ kpc) can be calculated by evaluating the above solution at $z = 0$ since our Solar system lies close to the Galactic plane. More explicitly, the differential number density measured at the location of

---

[1] For typical parameters, reacceleration only affects the CR spectrum below 10^5 GeV (Thoudam & Hörandel, 2014) and so is irrelevant for the energy range considered in this work.

Earth is

$$\begin{aligned} N(r,p) &= \int_{r'=0}^{R}\int_{k=0}^{\infty}\Sigma_0\frac{J_0[k(r-r')]}{L(p)}k\,dk\,e^{\frac{-(r'-R_p)^2}{\sigma^2}}\,r'\,dr' \\ &\quad \Big[Q(p)+\zeta s p^{-s}\int_{p_0}^{p}p'^{s}\,dp'\,Q(p')A(p') \\ &\quad \times\exp\left(\zeta s\int_{p'}^{p}A(u)du\right)\Big], \end{aligned} \tag{3.7}$$

where $R = 20$ kpc is the radial boundary of the Galaxy, Σ_0 is the number density of star clusters, J_0 is the Bessel function of order zero. Here the term $J_0[k(r-r')]$ is associated with the distance $(r-r')$ between sources and the earth, the term $\Sigma_0\,e^{\frac{-(r'-R_p)^2}{\sigma^2}}$ corresponds to the distribution of star clusters, the functions $Q(p)$ denotes the source spectra and the last term inside the third bracket correspond to the re-acceleration in weaker shocks. The solution was derived using the Green's function method. This involved performing a Fourier transform from real space to wave vector (k) space. The final solution is then obtained by transforming back to real space, which introduces the need for integration over k (For a detailed explanation of the steps involved in the solutions, please refer to Appendix A of Thoudam & Hörandel 2014). The functions $A(p)$ and $L(p)$ are given by,

$$L(p) = 2D(\rho)k\coth(kH) + nv\sigma(p) + \zeta\,, \tag{3.8}$$

$$A(p) = \frac{1}{pL(P)}. \tag{3.9}$$

Equation 3.7 gives the differential number density, i.e., number per unit volume per unit momentum of cosmic ray particles measured at earth. All the necessary terms needed to solve equation 3.7 are discussed in the previous sections.

3.3.3 Injection spectra of cosmic ray nuclei

The cosmic ray source spectrum $Q(p)$ from star clusters is assumed to follow a power-law in total momentum Ap, where A is the mass number of the nucleus, with an exponential cut-off. We write the differential number of CR particles with nucleon number A, having momentum per nucleon in the range $(p\,,p+dp)$, as,

$$Q(p) = Q_0(Ap)^{-q}\exp\left(-\frac{Ap}{Zp_{\max}}\right). \tag{3.10}$$

Here Q_0 is a normalization constant that is proportional to the fraction of total wind kinetic energy f channeled into CRs by a single star cluster. In writing Eq. 3.10, we assume that the maximum total momentum (or energy) for a cosmic-ray nuclei produced by a supernova remnant is Z times that of the protons. We call this 'injection fraction', which is a free parameter and can be estimated by comparing the model result with observations. Also, q is the spectral index, $p_{\rm max}$ is the cutoff momentum (for a single proton), and Ap is the total momentum of a particle with the mass number A and the atomic number Z.

3.3.4 Maximum energy estimate of accelerated particles

For the estimation of the maximum accelerated energy of cosmic ray particles, we consider two different acceleration scenarios inside a young star cluster: acceleration at WTS and acceleration of particles around SNR shock inside a star cluster.

3.3.4.1 Acceleration at wind termination shock (WTS):

In equation 3.10, $p_{\rm max}$, which represents the maximum momentum of accelerated CRs, depends on the extension of the accelerating region for a stellar wind bubble of the cluster. Typically this accelerating region can be taken as the distance to the WTS ($R_{\rm WTS}$) from the center of the cluster. The maximum energy is achieved when the diffusion length becomes comparable to the size of the shock (in this case the WTS). For beyond this limit, the particles escape out of the accelerating region. In the case of Bohm diffusion, $\kappa = pc^2/(\zeta qB)$, the maximum energy is then (Vieu et al., 2022):

$$E_{\rm max} \sim \zeta\, q B_{\rm WTS} R_{\rm WTS} \frac{V_w}{c}\,. \tag{3.11}$$

Here $R_{\rm WTS}$ is the radius of WTS. In the above equation, V_w is the velocity of stellar wind, $B_{\rm WTS}$ is the value of the magnetic field at the WTS position, $\zeta = 3r_g/\lambda$, with λ the mean free path due to the magnetic field. The Bohm diffusion, which is the most optimistic scenario, corresponds to the limit $\zeta = 3$. Bohm diffusion considers that the Larmor radius is equal to the mean free path (i.e., the distance between two scattering centers) of the particle. In this assumption, the underlying idea is that the particles experience one scattering while completing a Larmor radius. Due to the high rate of repeated scattering the diffusion coefficient is low for Bohm limit. This is valid for lower-energy particles. With increase in energy, the Larmor radius increases and it becomes larger than the mean free path. So the frequency of scattering decreases and the diffusion process becomes much more faster than the bohm limit. So a larger diffusion coefficient is expected in real astrophysical scenarios. Hence, considering Bohm diffusion we can get a conservative value of maximum energy.

We follow the arguments advocated by Vieu et al. (2022) to estimate the magnetic field in the cluster core. The magnetic field is amplified by the creation of large-scale magnetohydrodynamic (MHD) turbulence, which arises from the decay of primary outflows, such as stellar winds and supernova remnants (SNRs), within the cluster. It is expected that a portion of the mechanical power of the cluster is converted into MHD turbulence within the compact cluster. Assuming that the magnetic and hydrodynamic energies are in equipartition, we can write,

$$\frac{B^2}{8\pi} = \left(\frac{\rho^{1/2} S}{k_0}\right)^{2/3} . \tag{3.12}$$

Here, ρ is the matter density, $S = (\eta_T/V)P$ is the source of the turbulence at the largest scale $2\pi/k_0$ with mechanical power $P = 10^{36} N_{\rm OB}$ erg s^{-1}, V is the volume V and efficiency of generation of turbulence η_T, and B is the magnetic field. Assume that the stars are uniformly distributed within a sphere of radius R_c, representing the cluster's core radius. This distribution suggests that turbulence within the cluster is likely homogeneous. The characteristic turbulence scale is defined as the average distance between stars can be expressed as $L = (2/3)^{1/3} R_c N_{\rm OB}^{-1/3}$. Under all this consideration the magnetic field can be expressed from equation 3.12 as (Vieu et al., 2022),

$$B_c \sim 150 \left(\frac{n_{\rm c}}{10\,{\rm cm}^{-3}}\right)^{1/6} \left(\frac{\eta_T}{0.1}\right)^{1/3} \left(\frac{N_{\rm OB}}{100}\right)^{2/9} \left(\frac{R_c}{1{\rm pc}}\right)^{-2/3} \mu G . \tag{3.13}$$

Here, $n_{\rm c}$ is the core density, η_T is the efficiency of generation of turbulence, $N_{\rm OB}$ is the number of OB stars in the cluster (which determines the total mechanical power), R_c is the core radius of the cluster. The magnetic field advected into the free wind region has a $1/r$ radial profile. Therefore, the magnetic field at the position of the WTS and cluster core can be related using $B_c R_c = B_{\rm WTS} R_{\rm WTS}$. Therefore, equation 3.11 can be expressed as,

$$E_{\rm max} \sim \zeta\, q B_c R_c \frac{V_w}{c} . \tag{3.14}$$

If we substitute the expression of B_c from equation 3.13 in equation 3.16, this leads to a maximum estimate:

$$E_{\rm max} \sim 6 \left(\frac{\zeta}{3}\right) \left(\frac{n_{\rm c}}{10\,{\rm cm}^{-3}}\right)^{1/6} \left(\frac{\eta_T}{0.2}\right)^{1/3} \left(\frac{N_{\rm OB}}{1000}\right)^{2/9} \left(\frac{R_c}{1\ {\rm pc}}\right)^{1/3} \left(\frac{v_w}{2000\,{\rm km\,s}^{-1}}\right) {\rm PeV} . \tag{3.15}$$

Equation 3.15 gives a conservative estimate of $\mathrm{E_{max}} = 6\,\mathrm{PeV}$ (6×10^6 GeV) for the maximum attainable energy of protons. Note that this value is a few times higher than the maximum accelerated energy for the SNR-CR scenario.

However, in the realistic scenario, the magnetic field may be amplified in the accelerating region due to the existence of turbulence, and due to instabilities driven by cosmic ray streaming in the upstream region of WTS, which can therefore increase the estimated value of maximum accelerated energy. There are other uncertainties as well (e.g., in η_T, wind velocity v_w) that can conceivably increase the maximum energy by a factor of a few.

3.3.4.2 Acceleration at SNR shock inside star clusters:

Another potential scenario for CR acceleration inside the young star cluster is the SNR shocks propagating in the free wind region of the cluster. CR particles can be accelerated up to 10^8 GeV if the SNR shocks advance through fast and highly magnetized stellar winds (Voelk & Biermann, 1988; Biermann & Cassinelli, 1993). Non-linear effects in the acceleration process (Bell & Lucek, 2001) also contribute to this high-energy acceleration. Bell (2013); Schure & Bell (2013) highlight that the outer shocks of SNR can accelerate CR beyond the 'knee' if the shock propagates into a magnetic field much larger than a typical interstellar field, that can be present inside a star cluster. Particles will be accelerated during the expansion of the SNR shock upstream of the WTS. This idea has been studied extensively by Vieu et al. (2022). In the $1/r^2$ wind profile, the ejecta-dominated SNR shock exhibits self-similar evolution, following the relation, $R \propto t^m$, with m=7/8 (Finke & Dermer, 2012; Gaggero et al., 2018). The maximum energy is constrained either by the shock's size or its age. The size constraint is expressed as,

$$E_{\mathrm{max,size}} \sim \zeta\, q B_c R_c \frac{V}{c}\,. \tag{3.16}$$

Here V is the velocity of the SNR shock inside the free wind region, which decreases with time. Conversely, the time constraint on the maximum momentum is determined by analyzing the acceleration rate for a strong shock (compression ratio $r = 4$) and considering a diffusion coefficient κ. The acceleration rate can be expressed as (Lagage & Cesarsky, 1983b):

$$\frac{dP}{dt} \sim \frac{V^2 p}{k} \frac{r-1}{3r(r+1)}\,. \tag{3.17}$$

Assuming bohm diffusion and integrating the above equation with time with keeping in mind that $R \propto t^m$ we get,

$$E_{\mathrm{max,time}} \sim \frac{\zeta}{5}\frac{V_c}{c} q B_c R_c \frac{m}{1-m}\left[1-\left(\frac{R}{R_c}\right)^{(m-1)/m}\right]. \tag{3.18}$$

Here, V_c is the velocity of SNR shock at $R = R_c$. The maximum energy is attained when both criteria 3.16 and 3.18 are equal (i.e., when the SNR is neither too young nor too slow), which occurs when the SNR shock reaches a radius of:

$$R_\star = R_c\left(\frac{m}{5-4m}\right)^{m/(m-1)}. \tag{3.19}$$

However, for $m = 7/8$, the value of $R_\star$ is expected to surpass the radius of the WTS. Therefore, the maximum energy is achieved when the SNR collides with the WTS, and this can be calculated by setting $R = R_{\mathrm{WTS}}$ in equation 3.18. Hence, the maximum energy has been estimated as follows (Vieu et al., 2022):

$$E_{\mathrm{max}} \sim 21\left(\frac{V_c}{5000\,\mathrm{km\,s^{-1}}}\right)\left(\frac{\zeta}{3}\right)\left(\frac{R_c}{1\,\mathrm{pc}}\right)\left(\frac{N_{\mathrm{OB}}}{1000}\right)^{2/9}\left(\frac{n_{\mathrm{c}}}{10\,\mathrm{cm^{-3}}}\right)^{1/6} \\ \left(\frac{\eta_T}{0.2}\right)^{1/3}\left[1-\left(\frac{R_c}{R_{\mathrm{WTS}}}\right)^{1/7}\right]\ \mathrm{PeV}\,. \tag{3.20}$$

For a typical young cluster $R_{\mathrm{WTS}}/R_c \sim 5-30$, which gives $\left(1-(R_c/R_{\mathrm{WTS}})^{1/7}\right) \sim 0.2-0.4$ (Vieu et al., 2022). This estimate can give a maximum energy of a few PeV for protons. However, if a supernova launches a very fast shock in the free wind region of a compact cluster with velocity $\geq 2\times10^4$ km s^{-1}, it can accelerate protons up to a few tens of PeV energy. Note that, this high velocity of SNR shock inside a clumpy star cluster may efficiently drive MHD turbulence to generate a high value of the magnetic field, which will likely result in a higher value of maximum energy.

The recent detection of γ-rays above PeV by *LHAASO* from some sources indeed indicates these sources can accelerate particles up to at least a few tens of PeV because, at high energy, the γ-ray energy can be approximated as $E_{\mathrm{cr}} \approx 10E_\gamma$. Some of those sources possibly are young massive clusters (see extended table 2 of (Cao et al., 2021). The γ-ray photons from the LHAASO J2032+4102 source have the highest energy of 1.4 PeV, which corresponds to tens of PeV for cosmic ray protons.

3.3.5 Elemental abundances in star cluster winds

We consider a simple stellar population formed at time $t = 0$ with an initial mass function (IMF) $\frac{dn}{dm} \propto m^{-2.35}$ (Salpeter, 1955). We can calculate the elemental abundances in the wind material following the procedure described in Roy et al. (2021). Now,

$$M_w(X,m,t) = \int_0^t \dot{m}_w(X,m,t')\,dt' \tag{3.21}$$

is the cumulative mass of element X ejected in winds by a star of initial mass m up to age t where,

$$\dot{m}_w(X,m,t') = \text{mass fraction}(X,m,t') \times \dot{m}(m,t') = f(X,m,t') \times \frac{dm_{\text{star}}}{dt'}.$$

We use the mass loss rate for each nucleus $\dot{m}(X,m,t')$ using models for nucleosynthesis in massive stars and their return to the ISM via winds (A. Roy, private communication). Hence the elemental abundance of a particular element X can be calculated using the following equation,

$$f(X,m) = \frac{M_w(X,m,t)}{M_{w,\text{tot}}(m,t)} = \frac{\int_0^t \dot{m}_w(X,m,t')\,dt'}{\int_0^t \dot{m}(m,t')\,dt'}. \tag{3.22}$$

We have taken into account evolution until the core carbon burning time, which implies the maximum time of the evolution of a star with mass m as the upper limit of the integration. The mass-weighted elemental abundance of element X can be calculated using the following expression invoking the Salpeter mass function,

$$\langle f(X)\rangle = \frac{\int_0^m f(X,m)Am^{-2.35}dm}{\int_0^m Am^{-2.35}dm} \tag{3.23}$$

Using this method, we have calculated the mass-weighted mean individual elemental abundance in the ejected stellar wind material. We have used the results of a state-of-the-art evolutionary model. The elemental abundances have been calculated considering the rotation-driven instabilities inside the star, the correct abundances of elements, and the mass loss rate from the stellar surface.

3.3.6 Average kinetic luminosity of clusters:

Our assumption requires a certain fraction of the total wind kinetic energy to go into CRs. Therefore, we need the value of the average kinetic luminosity of a cluster using a distribution of OB associations over the luminosity range. Oey & Clarke (1997) assume that the mechanical luminosity function of OB association is given by $\phi(L) \propto L^{-2}$. We use this distribution to calculate the average luminosity of clusters with kinetic luminosity in the range $L_{\rm min} = 10^{37}$ erg s^{-1} (corresponds to $N_{\rm OB} = 10$) to $L_{\rm max} = 10^{39}$ erg s^{-1} (corresponds to $N_{\rm OB} = 1000$) as following,

$$\langle L_w \rangle = \frac{\int_{L_{\rm min}}^{L_{\rm max}} \phi(L)\, L\, dL}{\int_{L_{\rm min}}^{L_{\rm max}} \phi(L)\, dL} \sim 4.5 \times 10^{37}\ {\rm erg\, s^{-1}}. \tag{3.24}$$

Note, we adopt a minimum 10 number of OB stars for the production of CRs, and the largest OB association in our Galaxy has 1000 OB stars. The dependence of $\langle L_w \rangle$ on $L_{\rm max}$ is weak, but there is a sensitive dependence on $L_{\rm min}$, the implications of which we discuss later.

3.4 Model prediction for the second component of galactic cosmic rays

The values of cosmic ray propagation parameters (D_0, δ; the normalization of the diffusion coefficient and its power-law dependence on momentum) and re-acceleration parameters (η ,s; the SNR filling factor and reacceleration power-law index) have been calculated by comparing the observed Boron to Carbon abundance ratio with the value obtained by the adopted model. The best fit values are $D_0 = 9 \times 10^{28}$ cm^{2}s^{-1}, $\eta = 1.02$, $s = 4.5$, and $\delta = 0.33$ (Thoudam & Hörandel, 2014). We have also used these values in our model. For the interstellar matter density (n), the averaged density in the Galactic disk within a radius equal to the size of the diffusion halo H was considered. We choose $H = 5$ kpc (Thoudam et al., 2016), which gives an averaged surface density of atomic hydrogen of $n = 7.24 \times 10^{20}$ atoms cm^{-2} (Thoudam & Hörandel, 2014). To account for the helium abundance in the interstellar medium, we add an extra 10% to n. The radial extent of the source distribution is taken as $R = 20$ kpc. The inelastic cross-section for proton ($\sigma(p)$) is taken from Kelner et al. (2006).

Since we are interested in the acceleration of CRs in WTS, as well as around SNR shocks inside the free wind region of the star cluster, the relevant abundances correspond to that in the stellar wind for massive stars. For this purpose, we use the stellar wind abundances for massive stars beginning with the Zero Age Main Sequence (ZAMS) phase. We have used the surface abundance of massive stars as a function of time, calculated after properly taking into account the effect of stellar rotation. The spectral indices for different elements are given in Table 3.1. The fitting of elemental cosmic ray spectra requires different spectral indices for different elements. However, this remains an open problem in cosmic ray literature. Previous works such as Wiebel-Sooth et al. 1998; Ave et al. 2008; Ahn et al. 2009; Thoudam & Hörandel 2014; Thoudam et al. 2016 etc use different spectral index for different elements to fit the

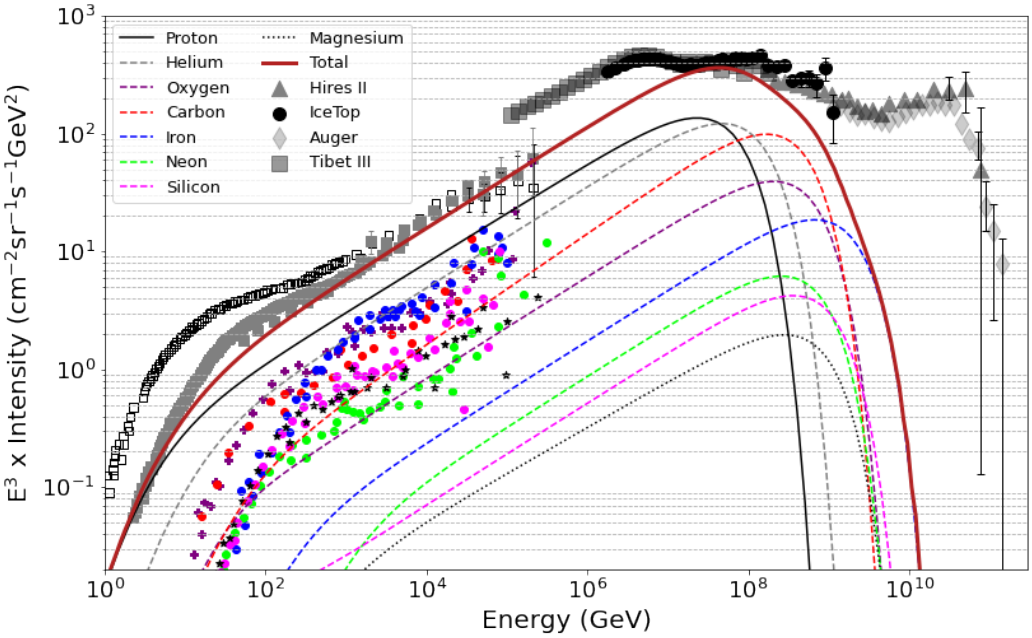

Fig. 3.2 Model prediction for the star cluster model as a second galactic component considering an injection fraction $\sim 5\%$. The thick solid maroon line represents the total contribution from Galactic star clusters. Thin dashed lines represent the flux of individual elements. For the CRs generated from star clusters, an exponential energy cut-off for protons at $E_c = 5 \times 10^7$ GeV (50 PeV) is assumed. High-energy data: IceTop (Aartsen et al., 2013), Tibet III (Amenomori et al., 2008), the Pierre Auger Observatory (The Pierre Auger Collaboration et al., 2013), and HiRes II (High Resolution Fly'S Eye Collaboration et al., 2009). Low energy data have been taken from CREAM (Ahn et al., 2009; Yoon et al., 2011), ATIC-2 (Panov et al., 2007), AMS-02 (Aguilar et al., 2015), PAMELA (Adriani et al., 2011), CRN (Mueller et al., 1991), HEAO (Engelmann et al., 1990), TRACER (Obermeier et al., 2011), KASCADE (Antoni et al., 2005), DAMPE (An et al., 2019). We have only shown the high-energy data points with different symbols in the figure. Low data points: Proton (black square), Helium (grey square), Oxygen (purple solid plus), Carbon (red circle), Iron (blue circle), Neon (green circle), Silicon (magenta circle), Magnesium (black stars). The lower energy data from various experiments are represented together by one symbol. The error bars for proton and helium have been shown and the rest are not shown in the figure.

Elements	q	**Fractional abundances in winds**
Proton	2.25	0.86
Helium	2.23	0.13
Carbon	2.20	3.32×10^{-3}
Oxygen	2.24	8.51×10^{-4}
Neon	2.24	8.83×10^{-5}
Magnesium	2.28	3.62×10^{-5}
Silicon	2.24	3.42×10^{-5}
Iron	2.24	3.72×10^{-5}

Table 3.1 Source spectral indices q and fractional abundances of different elements in the wind material. The elemental abundances are calculated following Roy et al. (2021).

observed data well. In particular, the differential energy spectra for different nuclei (protons, helium, carbon, iron etc) can be significantly different, reflecting the varying acceleration and propagation conditions for each species. Note that the values mentioned in Table 3.1 are slightly different from the spectral indices assumed in Thoudam et al. (2016) for the SNR-CR component. Also, the stellar wind elemental abundances are mentioned in Table 3.1, which are calculated using the method described in Roy et al. (2021) (provided to us by A. Roy, private communication). We have then averaged the abundances over time and mass distribution of stars in the cluster, as described in section 3.3.4. Using these values of various parameters, we calculate the particle spectra for different cosmic ray elements (proton, helium, carbon, oxygen, neon, magnesium, silicon, and iron). The CR spectral indices (q) of source spectra for the individual elements are very similar to each other and are chosen to match the observed individual nuclear abundances in CRs closely.

Figure 3.2 shows the star cluster contribution to CRs using different parameters mentioned earlier. We have used the maximum energy for the proton as 5×10^7 GeV (50 PeV) and the injection fraction of $\sim 5\%$. These values of the parameters are chosen to match the observed spectra with our theoretical model. It is important to mention that, in section 3.3.4 we have estimated the maximum accelerated energy considering different scenarios in a star cluster. The maximum energy can go up to a few tens of PeV (especially for the SNR shock inside the star cluster scenario), although our used value is admittedly on the higher side. Also, recently Vieu & Reville (2023) have shown that the SNR shocks inside a star cluster scenario can explain the all-particle cosmic ray spectrum in the region between ‘knee’ and ‘ankle’. Therefore, star clusters are likely a possible candidate for cosmic ray acceleration between a few times 10^6 and 10^9 GeV.

Also, if one uses a higher lower limit of $N_{\rm OB} = 30$ instead of 10, then the injection fraction will need to be decrease to match the observed spectrum. Figure 3.3 shows how the injection

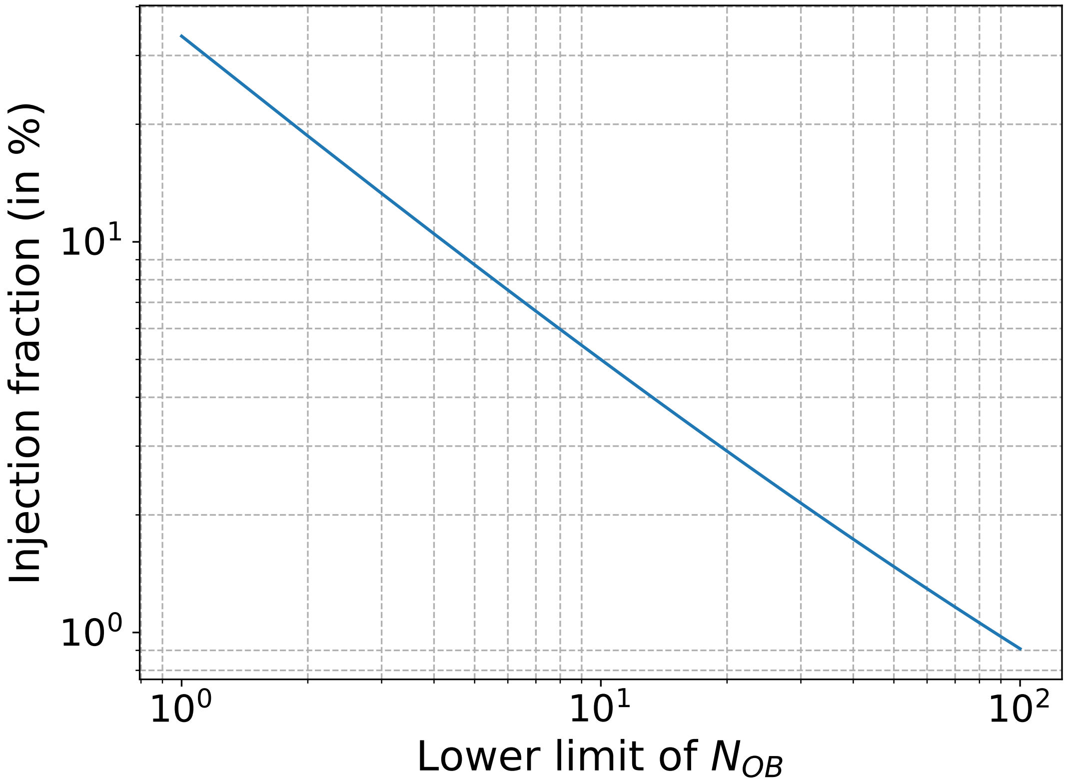

Fig. 3.3 Injection fraction as a function of lower limit of N_{OB}.

fraction will decrease with an increase in the lower limit of N_{OB}. The data points correspond to different measurements. For lower energy ranges, the individual spectra are fitted to the observed elemental spectra. We consider 8 elements: proton, helium, carbon, oxygen, neon, magnesium, silicon, and iron for our calculations, and the total contribution (solid brown curve in the figure 3.2) is a combination of these 8 elements.

3.5 All-particle spectrum of cosmic rays

Figure 3.4 combines all three CR components to get the total all-particle spectrum of CRs and compares it with various observations. The SNR-CR component shown in this figure is calculated following the procedure mentioned in Thoudam et al. (2016), assuming a uniform distribution of SNRs in the Galactic plane and a proton spectrum cut-off of $\sim 2.5 \times 10^6$ GeV. For the extragalactic component, we have adopted the *UFA* model (Unger et al., 2015), which considers a significant contribution of extragalactic CRs below the ankle to reproduce the observed CR energy spectrum as well as $X_{\max}$ (the depth of the shower maximum) and the variance of $X_{\max}$ above the ankle observed at the Pierre Auger Observatory (di Matteo, 2015). With these two models (SNR & extragalactic), we have combined our proposed star cluster model with a proton spectrum cut-off at 5×10^7 GeV (50 PeV).

The total contributions from all these three components can explain the observed features in the all-particle spectrum. Also, the spectra of the individual elements can be explained well with the model. The flux of different elements has been measured well in the lower energy region, but in the higher energy range, i.e., above 10^{5-6} GeV, the observation data for individual elements are not available. Observed data points for all-particle CR spectra have been taken from various experiments like TIBET III (Amenomori et al., 2008), IceTop (Aartsen et al., 2013), Auger (The Pierre Auger Collaboration et al., 2013), HiRes II (High Resolution Fly'S Eye Collaboration et al., 2009), etc.

Several ground-based experiments such as KASCADE, TUNKA, LOFAR, and the Pierre Auger Observatory have provided measurements of the composition of CRs at energies above $\sim 10^6$ GeV. Heavier nuclei interact at a higher altitude in the atmosphere, which results in smaller values of $X_{\max}$ as compared to lighter nuclei. For comparison with the theoretical predictions, $\langle \ln A \rangle$, the mean logarithmic mass of the measured CRs, is of utmost importance. This can be obtained from the measured $X_{\max}$ values using the following relation mentioned in Hörandel (2003),

$$\ln A_i = \left(\frac{X^i_{\max} - X^{\mathrm{p}}_{\max}}{X^{\mathrm{Fe}}_{\max} - X^{\mathrm{p}}_{\max}} \right) \times \ln A_{Fe}. \tag{3.25}$$

Here $X^{\mathrm{p}}_{\max}$ and $X^{\mathrm{Fe}}_{\max}$ represent the average maximum depths of the shower for protons and iron nuclei, respectively, and $\mathrm{A_{Fe}}$ is the mass number of iron nuclei. In figure 3.5, we have also shown the obtained mean logarithmic mass using our model and compared it with the observational data.

We calculate the mean mass in the following way,

$$\langle \ln A \rangle = \frac{\sum_i \ln A_i \times \mathrm{Flux_i}}{\sum_i \mathrm{Flux_i}} \tag{3.26}$$

where A_i denotes the mass number of an element i (we have considered 8 elements: proton, helium, carbon, oxygen, neon, magnesium, silicon, and iron), and $\mathrm{Flux_i}$ is the obtained flux of element i using our model. Figure 3.5 shows that the results obtained using our star cluster model (green curve) follow the observed trend for the mean logarithmic mass in the total energy range from 10^8 GeV to 10^{11} GeV when combined with the UFA model for the extragalactic CRs. In the energy range of about 2×10^7 and 10^8 GeV, our prediction shows some deviation from the observed trend but still lies within limits presented in Kampert & Unger (2012).

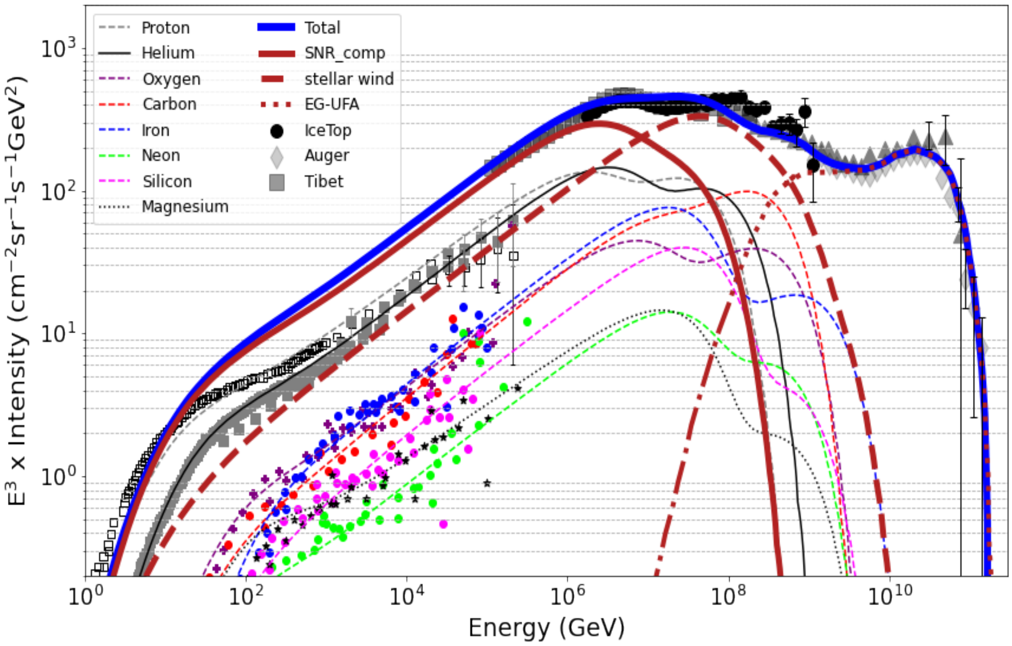

Fig. 3.4 Model prediction for the all-particle spectrum using the Galactic star cluster CR model as the second galactic component. For the star cluster component, the considered injection fraction is $\sim 5\%$, and the cutoff is at $5 \times 10^7 Z$ GeV. The thick solid maroon line represents the total SNR-CRs, the thick dashed maroon line represents star cluster CRs, and the thick maroon dotted line represents the UFA model of extragalactic CR component (EG-UFA) taken from Unger et al. (2015), and the thick solid blue line represents the total all-particle spectrum. The thin lines represent the total spectra for the individual elements i.e., a combination of both SNR-CR and the CRs originating from star clusters. The figure shows the E^3 times the cosmic ray flux $I(E) = (c/4\pi)N(E)$ at the position of the earth measured by different experiments as a function of cosmic ray energy, where $N(E)$ is the differential number density of cosmic ray particles. High energy and low energy data are the same as figure 3.2.

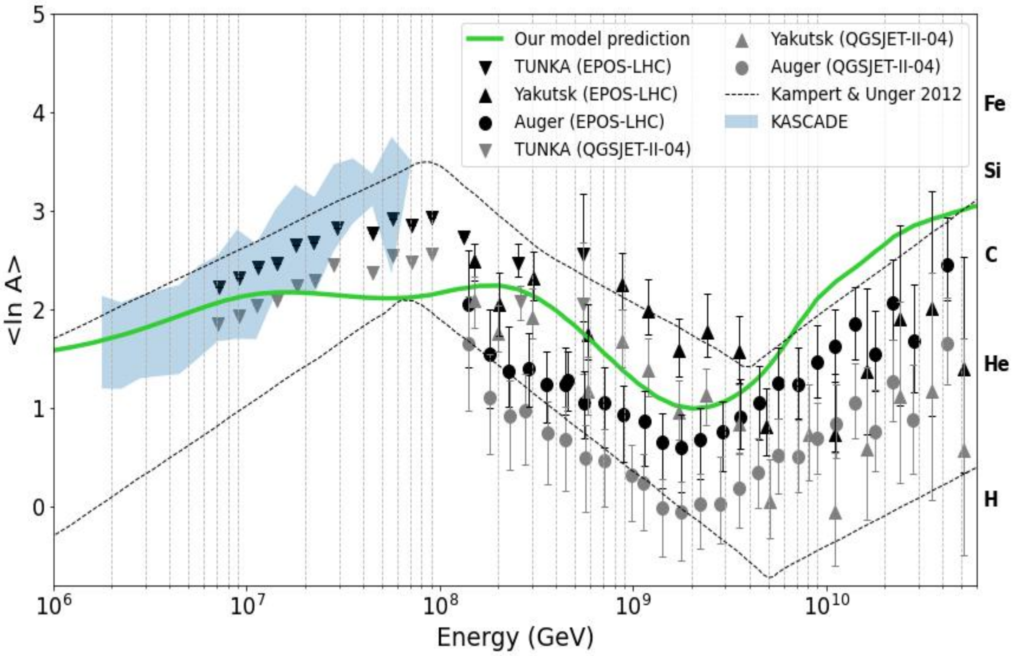

Fig. 3.5 Mean logarithmic mass $\langle \ln A \rangle$ of CRs as a function of energy, predicted using the combination of SNR-CR, CRs from star clusters (these two are Galactic components), and EG-UFA model (extragalactic component, Unger et al. 2015). Data: KASCADE (Antoni et al. 2005), TUNKA (Berezhnev 2015), Yakutsk (Knurenko & Sabourov 2011), the *Pierre Auger* observatory (The Pierre Auger Collaboration et al. 2015) and the different optical measurement compiled in Kampert & Unger 2012. The two different colored (black and grey) sets of data points correspond to two models EPOS-LHC and QGSJET-II-04, respectively, which have been used to convert $X_{\max}$ values to $\langle \ln A \rangle$ (see equation 3.25).

To reiterate, the primary focus of this work has been to present a model incorporating stellar wind shocks that can explain the observed all-particle CR spectrum, especially in the energy range between 10^7 and 10^9 GeV. The discussion so far shows that we can indeed explain the observed data in this energy range using a CR component originating from massive star clusters. The required CR injection fraction for this component of $\sim 5\%$ and an energy cutoff of $5 \times 10^7 Z$ GeV (50 PeV), as suggested by the fitting of the all-particle CR spectrum with our proposed stellar wind model, are entirely reasonable, and therefore lend support to the idea that CR from massive star clusters can fill the CR spectrum gap between the 'knee' and the 'ankle'.

3.6 Varying the extragalactic component

As mentioned in 3.2.2, we consider two different models of extragalactic CRs: UFA model (Unger et al., 2015) and a combination of PCS and Minimal model (MPCS model) (Rachen, 2015; Thoudam et al., 2016). Depending on the chosen extragalactic component, the value of injection fraction and maximum cutoff energy can slightly change. The UFA and MPCS models predict a significant contribution of extra-galactic CRs below the 'ankle'. All these different extragalactic models can explain the observations when combined with the SNR-CR component and the CR component from star clusters, although the UFA model somehow shows a smooth transition (Figure 3.4) between the Galactic and extragalactic components. The sharp increase near 10^9 GeV in the MPCS model (top panel, figure 3.6) is due to the dip in the proton spectrum. It results from the intersection of the minimal model and the components from galaxy clusters. Below 10^9 GeV, both the UFA and MPCS models give similar results and can explain the observed spectra.

We have also shown the mean logarithmic mass plot for a combination of each different extragalactic model with the two different Galactic components (bottom panel of figure 3.6). It is clear from the plot that all these different models for the extragalactic component, in combination with the Galactic components, follow the observed trend of mean logarithmic mass for the whole energy range.

3.7 Discussion

Our study demonstrates that the CRs originating from spatially distributed young massive star clusters in the Galactic plane fit well the all-particle CR spectrum, particularly in the $10^7 - 10^9$ GeV energy range, and therefore this can be a potential candidate for the 'second Galactic component' of CRs. We also show that the observed all-particle spectrum, as well as the cosmic ray composition at high energies, can be explained with the following two types of Galactic

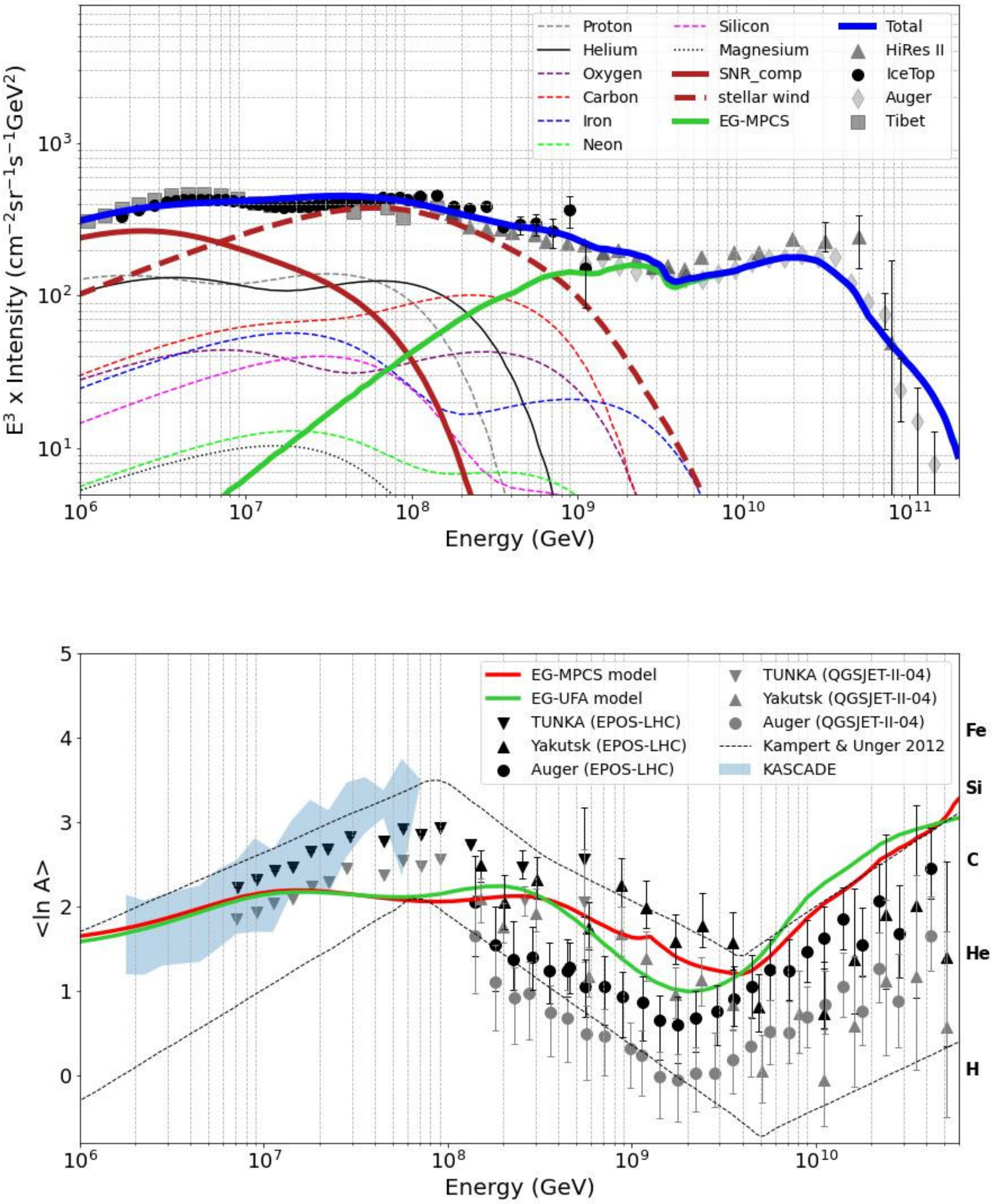

Fig. 3.6 *Top panel:* All-particle CR spectrum when combined with SNR-CRs and EG-MPCS model (Rachen 2015) for the extragalactic CRs. *Bottom panel:* Mean logarithmic mass when combined with the EG-MPCS (red curve) and the EG-UFA (green curve, same as 3.5) models. Data are the same as in Figure 3.5.

sources: (i) SNR-CRs, dominating the spectrum up to $\sim 10^7$ GeV, and (ii) star cluster CRs, which dominate in the range $10^7 - 10^9$ GeV.

The SNR-CR component can only contribute up to maximum energy, corresponding to a proton cut-off energy of 2.5×10^6 GeV (Thoudam et al., 2016). Such a high value of energy cannot be achieved if we consider the DSA mechanism with typical values of the magnetic field in the ISM. However, some numerical simulations have indicated that supernova shocks can amplify the magnetic field near them several times larger than the value in the ISM (Bell & Lucek, 2001; Reville & Bell, 2012). Such a strong magnetic field can accelerate CR protons up to the cut-off energy used in this study. Also, recently detected γ-rays from a few SNRs have also identified a few SNRs as cosmic ray PeVatrons that can accelerate particles up to a few times $\sim 10^6$ GeV energy.

Maximum CR energy in star clusters: According to our model, the component of CRs that is plausibly generated in star clusters can contribute significantly towards the total CR flux, especially in the $10^7 - 10^9$ GeV range, if one considers that the protons can be accelerated up to 5×10^7 GeV energy. For other elements with atomic number Z, the maximum energy is 5×10^7 Z GeV in these young compact star clusters, and a cosmic ray injection fraction of $\sim 5\%$. Note that this value of maximum energy required for proton is slightly on the higher side, but can be justified under the assumption of the very high initial shock velocity of SNRs inside compact clusters, faster wind velocity, and possible amplification of magnetic field inside the cluster. Our maximum CR energy from Hillas criterion may be an overestimate, but we should point out that the requirement of $E_{\max} = 50$ PeV (5×10^7 GeV) depends on the assumption of elemental abundance ratios in the wind material, an aspect that remains uncertain at present. A higher abundance of heavy elements would increase $E_{\max}$, as required to fit the observed spectrum. Also note that the recently detected γ-ray photons by *LHAASO* in PeV range from 12 objects, some of which are associated with massive star clusters, have indicated that these clusters can accelerate particles at least up to a few tens of PeV (Cao et al., 2021), consistent with our estimates.

CR anisotropy: The total CR anisotropy Δ can be calculated from our model using the diffusion approximation given by Mao & Shen (1972),

$$\Delta = \frac{3D}{c}\frac{|\nabla N|}{N} \,, \tag{3.27}$$

where N is the CR number density, D is the diffusion coefficient and c is the velocity of light. From our model, we get $\Delta \sim 0.04 - 0.2$ in the range $1 - 100$ TeV. However, it is noteworthy that our calculated estimates exhibit higher values compared to the measured anisotropy, which is approximately in the range of $(0.5 - 1) \times 10^{-3}$ for the same energy spectrum. Notably, our findings align with the earlier estimates proposed by Thoudam & Hörandel (2012b), although, like the case of previous calculations, they are larger than the observed anisotropy in the same energy range. The anisotropy calculated in previous studies, such as Blasi & Amato (2012); Thoudam & Hörandel (2012c) , is consistently larger than the observed limits reported by various experiments, particularly in the 10^5–10^6 GeV energy range. These observed values carry significant uncertainties, as discussed in Blasi & Amato (2012). None of the theoretical models to date, including those exploring different parameters, source distributions, or geometries, have been able to account for the low levels of observed anisotropy. This remains an open problem in the field of cosmic ray research.

Inside an OB association, individual SNR shocks, as well as colliding shocks, can accelerate particles on a time scale below 1000 years. An OB association may enter the evolutionary stage of multiple SN explosions on a time scale larger than a few hundred thousand years. It can create large bubbles of ~ 50 pc size, and the injected mechanical power can reach $\sim 10^{38}$ erg s^{-1} over 10 Myr—the lifetime of a superbubble. This process is supplemented by the formation of multiple shocks, large-scale flows, and broad spectra of MHD fluctuations in a tenuous plasma with frozen-in magnetic fields. The collective effect of multiple SNRs and strong winds of young massive stars in a superbubble is likely to energize CR particles up to hundreds of PeV in energy (see Montmerle 1979; Cesarsky & Montmerle 1983; Axford 1994; Higdon et al. 1998; Bykov & Toptygin 2001; Marcowith et al. 2006; Ferrand & Marcowith 2010) and even to extend the spectrum of accelerated particles to energies well beyond the 'knee' (Bykov & Toptygin, 2001).

Gupta et al. (2020) pointed out the advantage of considering CRs accelerated in massive star clusters in explaining several phenomena (e.g., Neon isotope ratio) that are left unexplained by the paradigm of CR production in SNRs. They also proposed that this component need not be considered entirely independent and separate from the SNR component since massive stars (which are the progenitors of SNRs) always form in clusters. Therefore, the two components (SNR-CR and star cluster CRs) arise from similar sources, with some differences. The SNR-CRs can be thought of as CRs produced in individual SNRs, which arise from very small clusters with one or two massive stars, whereas the second component can be thought of as arising from different shocks that occur in the environment of massive star clusters. The cluster luminosity function (Williams & McKee, 1997) is observed to be $dN/dN_{\rm OB} \propto N_{\rm OB}^{-2}$, where $N_{\rm OB}$ is the number of OB stars in a cluster. This implies that roughly half the clusters would produce an apparently isolated (core collapse) SNR (Gupta et al., 2020). Hence, the two components can be put on the same platform, and the combined scenario offers a fuller, more complete picture of the phenomenon of CR acceleration in the Galaxy.

3.7.1 Caveats of our model

Finally, we discuss some caveats of our model.

The injection fraction, a free parameter in our analysis whose value is obtained by fitting the all-particle CR spectrum, ultimately depends on many other factors, such as diffusion coefficient, the assumed lower limit of the number of OB stars in a cluster, and so on. With a higher value of diffusion coefficient, the required injection fraction should be increased in order to match our results with observations. A larger diffusion coefficient implies that particles would diffuse out of the source more rapidly, which will decrease the particle density in the vicinity of clusters. This is why one needs a larger injection fraction to explain the observational data. On the other hand, the total number of OB associations depends on the lower cut-off in the distribution of cluster masses. For, the number of OB associations which has a minimum of 30 OB stars is lower than the number of OB associations with a minimum of 10 OB stars. For the second case, the required injection fraction will be lower (since the number of OB associations is higher). Also, the location of the peak of the cluster spatial distribution has a significant effect on the observed flux and may introduce some uncertainty to the value of the injection fraction parameter.

The efficiency is likely independent of the number of OB stars inside a single-star cluster. Considering the gamma-ray luminosity of massive star clusters, observations indicate the gamma-ray luminosity is $\sim 10^{-3} \times L_w$ (where L_w the wind kinetic energy), irrespective of the total stellar number (e.g., Ackermann et al. 2013), as we have assumed here (see also Gupta et al. 2018b). However, the required cosmic ray injection fraction to explain the observed data depends on the total number of star clusters in the Galaxy. For the current study, we have considered the spatial distribution of OB stars but we did not classify them according to their age and mass. According to the recent GAIA survey, $\sim 20\%$ of the total clusters are compact young, and massive (Vieu et al., 2022). However, we have assumed all the OB associations are young and compact. If we instead take a fraction (say 20%) of these clusters to be young then we would need a higher (by a factor of 5, say) fraction of cosmic ray injection efficiency to match the observed flux.

Elemental abundance: There are other uncertainties that arise from the assumed abundances of the eight elements considered here. This elemental abundance depends on the rotational velocity of the stars. For our calculations, we have used the abundances of stars, which rotate with a velocity that is 60% of the critical velocity of the star. Varying the rotational velocity would change the elemental abundances. This will give an uncertainty between $2-3\%$ in the mean logarithmic mass plot (see figure 3.5). Results may also change if abundances from other previous works (Heger et al. 2000, 2005) were to be used. Comparing the abundances from these works with the ones used here, we find that it would introduce an uncertainty of

$5-7\%$ in Figure 5. However, these variations will not significantly change the shape of our predicted $\langle \ln A \rangle$.

CR propagation: Another aspect that is important to mention is the mode of cosmic ray propagation. Our calculation of the second component assumes diffusion from the source. Nevertheless, it is crucial to acknowledge that the diffusion approximation may cease to be valid beyond a specific energy threshold, leading to a shift from diffusion to drift motion in the transport process. If we consider a mean magnetic field of 3 μG in the Galactic plane then the transition from diffusion to drift will occur at $\sim Z \times 10^{17-18}$ eV (Kääpä et al., 2023). The maximum energy for proton in WTS is $\sim$ 50 PeV (5×10^{16} eV) and is below the transition region. Therefore, the diffusion approximation works well for the energy range considered by us. However, we modified the diffusion coefficient above 10^{17} eV in a manner that mimics ballistic propagation beyond this energy threshold and found the spectra do not change significantly as the second component in this energy range is mainly dominated by the exponential cutoff.

3.8 Conclusions

In this chapter, we suggest that the 'second Galactic component of CRs', needed to explain the observed flux of CRs in the range between the 'knee' and the 'ankle' (10^7 GeV to 10^9 GeV), may arise from a distribution of massive star clusters.

This component can bridge the gap between the SNR-CR component, which dominates below $\sim 10^7$ GeV, and the extragalactic component, which dominates above $\sim 10^9$ GeV. It has been previously noted that SNR-CRs and CRs from star clusters need not be considered two separate components, but rather originating from similar sources, *viz.* massive star clusters, the less massive ones leading to individual SNRs and SNR-CRs, while the more massive ones can accelerate CRs in a variety of strong shocks appearing in the dense cluster environment. We have argued that there is a possibility of acceleration of protons up to a few tens of PeV by considering the particle acceleration around the WTS, as well as acceleration by SNR shocks inside massive star clusters. This value is larger than that possible in the standard paradigm of CR acceleration inside supernova remnants present in the ISM. In this work, we have carried out a detailed calculation of the propagation of CRs in the Galaxy and demonstrated that this model can possibly explain the all-particle CR spectrum measured at the Earth. Our calculation considers a realistic distribution of star clusters in the Galaxy and also includes all the important transport processes of CRs including re-acceleration by the old SNRs in the Galaxy.

Our analysis requires a proton cut-off energy of $\sim 5 \times 10^7$ GeV (50 PeV) for the CRs accelerated in star clusters. A comparison of our analytical results with the observed all-particle CR spectrum yields an injection fraction (the fraction of kinetic energy of shocks being deposited in CRs) of $\sim 5\%$ (depending on the choice of the extragalactic component). Furthermore, the variation of the mean logarithmic mass with CR energy (especially in the energy range of around 10^7–10^9 GeV) supports the argument that the suggested CR component from star clusters can be considered as the second Galactic component of CRs.

4

Effect of nearby cosmic ray sources on the observed elemental spectra

Based on:

"TeV spectral bump of cosmic-ray protons and helium nuclei: the role of nearby supernova remnants", **Bhadra, S.**, Thoudam, S., Nath, B., Sharma P., submitted in ApJ.

The presence of distinct cosmic-ray sources in close proximity can yield intriguing effects on the observed characteristics of cosmic rays (CRs). Recent observations from the DAMPE and CALET experiments have unveiled a novel bump-like feature in the proton and helium spectra within the energy range of approximately $1-100$ *TeV. Despite its emergence, the origin of this feature remains ambiguous. In this study, employing an enhanced and more comprehensive analysis compared to previous investigations, which includes utilizing the latest age and distance assessments of nearby supernova remnants and considering time-dependent CR escape mechanisms, we demonstrate that the spectral bump can be accounted for by the influx of CRs originating from these nearby supernova remnants.*

Main results

- This study demonstrates that the observed spectral bumps of cosmic-ray protons and helium nuclei in the TeV range, as identified by the DAMPE and CALET experiments, can be attributed to the influence of CRs originating from nearby supernova remnants (SNRs) located within approximately 1 kiloparsec, particularly emphasizing the role of the Vela supernova remnant.

- We incorporate a more realistic energy-dependent escape time for particles originating from the sources, a crucial factor in elucidating the occurrence of the spectral bump at varying energies for protons and other heavier elements.

- When examined alongside a background CR component originating from distant sources, the involvement of nearby remnants is likewise discovered to align with both the observed CR spectra of heavier elements spanning from carbon to iron and the all-particle spectrum at energies around the ‘knee’ region.

4.1 Introduction

In the previous chapter our focus was to explain the CR spectra in the high-energy regime beyond PeV. In this chapter, we shift our focus to the lower energy portion (TeV-PeV range) of the CR spectra. Recently, several experiments have observed a special spectral feature which is the hardening of CR proton, and helium spectra around several TeV energy. Using a similar CR propagation framework, which we used in the previous chapter, it is possible to investigate the underlying phenomenon of the spectral hardening around TeV. As discussed already in previous chapters, CRs are charged particles spanning a broad energy spectrum from 1 GeV to around $\sim 10^{11}$ GeV. Supernova remnants (hereafter SNRs) have long been regarded as promising candidates for particle acceleration (Axford et al., 1977; Blandford & Ostriker, 1978), particularly up to a few PeV (Lagage & Cesarsky, 1983a). Based on the fundamental principles outlined in the linear theory of diffusive shock acceleration (DSA) of CRs, along with the understanding of CR transport within the galaxy, it is anticipated that the CR spectrum will follow a single power law with an index -2.7, extending up to approximately $\sim 3 \times 10^6$ GeV (i,e 3 PeV), commonly referred to as the CR 'knee'. The spectrum steepens from -2.7 to -3.1 above 'knee' and again flattens back to -2.7 at 4×10^9 GeV, which is known as 'ankle'. Eventually, at $\sim 10^{11}$ GeV the CR spectrum was believed to terminate in the so-called GZK cutoff (Greisen, 1966; Zatsepin & Kuz'min, 1966) due to interaction with cosmic microwave background (CMB) photons.

Several additional distinctive features are present in the spectra of individual elements below the knee energy. In this work, we focus on the recent observations of a bump-like feature in the spectra of protons and helium nuclei by the DAMPE (An et al., 2019; Alemanno et al., 2021) and CALET (Adriani et al., 2022a, 2023) experiments. This feature exhibits a hardening in the spectra at energies of a few hundred GeV, confirming earlier detections by the AMS-02 (Aguilar et al., 2018b) and PAMELA (Adriani et al., 2011) experiments, followed by a subsequent softening around hundreds of TeV. The general expectation of a diffuse background of CRs, originating from a distribution of SNRs in the Galaxy cannot explain the observed bump-like feature. Various explanations for the spectral hardening have been proposed which include those based on different physical mechanisms affecting the CR source spectra (Biermann et al., 2010; Ohira et al., 2011; Ptuskin et al., 2013; Yuan et al., 2011) and the propagation properties of CRs in the Galaxy (Blasi et al., 2012; Tomassetti, 2012), additional processes such as CR reacceleration during their propagation (Thoudam & Hörandel, 2014) and the effect of nearby sources (Erlykin & Wolfendale, 2012; Thoudam & Hörandel, 2012d; Bernard et al., 2013). However, a convincing explanation for the origin of the spectral bump is still lacking. Here, we present an explanation based on a similar set of potential nearby sources that have been earlier proposed to account for the spectral hardening observed at a few hundred GeV (Thoudam & Hörandel, 2012d).

The presence of nearby discrete CR sources is expected to produce noticeable effects on the observed spectra of CRs. This effect on the CR electron spectrum has been studied by Mao & Shen (1972) and Cowsik & Lee (1979), and in later studies such as Kobayashi et al. (2004); Mertsch (2011), and Thoudam & Hörandel (2012a). The effect of source discreteness on CR nuclei has also been investigated by Büsching et al. (2005) and Strong et al. (2009). The recent observations of spectral hardening of CR proton and helium nuclei at a few hundred GeV by the PAMELA and AMS-02 experiments have drawn further interest towards a deeper understanding of the effect of nearby discrete sources.

The presence of nearby sources may also be responsible for the recently observed spectral bump feature in the CR proton and helium spectra by the DAMPE and CALET experiments. Current explanations for the spectral bump are based on a multi-component origin of CRs involving nearby sources. For instance, Yue et al. (2019) has proposed the existence of different CR components originating from different populations of SNRs and nearby sources, while Malkov & Moskalenko (2021) proposed the presence of nearby Epsilon Indi or Epsilon Eridani stars as the origin of the bump, and Li et al. (2024) explained it on the basis of the presence of nearby SNRs.

In this study, we investigate in detail the contribution of CRs at the Earth from nearby SNRs in the presence of a CR background generated by distant sources. We consider a total of 11 known SNRs located within a distance of ~ 1 kpc (listed in table 4.1), and show that these nearby SNRs can be responsible for the observed spectral bump, in particular the Vela remnant. We also show that our predicted spectra are also consistent with the all-particle spectrum observed at very high energies beyond the knee region (at few PeVs), something which has not been thoroughly explored in previous studies that had focused on the spectral bump. In addition, we use updated distances and ages of the nearby SNRs, account for their finite sizes in contrast to the commonly assumed point-like approximation, and consider a time-dependent escape for CRs of different energies from the remnants unlike in previous works. We also present our findings on the secondary-to-primary ratios and CR anisotropy based on our model.

The chapter is organized as follows. We describe our model and present the calculations for the CR flux from the background and the nearby sources in Section 4.2. We present the main results in Section 4.3, the discussion of our findings in Section 4.4, and the conclusion in Section 4.5.

4.2 The model

It is widely accepted that SNRs are the major particle accelerators that can accelerate CR particles up to $\sim 10^2 - 10^3$ TeV (Lagage & Cesarsky, 1983a; Axford, 1994). This predominant acceleration mechanism, known as the diffusive shock acceleration (DSA), has been firmly established through both theoretical (Fermi 1949; Axford et al. 1977; Bell 1978; Blandford & Ostriker 1978; Blasi 2013) and phenomenological (Drury et al., 1994; Ackermann et al., 2013; H. E. S. S. Collaboration et al., 2018c) studies. Based on these studies, we assume SNRs to be the major source of CRs, especially up to the energy range of $\leq 10^{5-6}$ GeV (Lagage & Cesarsky, 1983a). In our model, we consider two distinct components of CRs: a steady (time-independent) diffuse background CR that dominates the spectrum at most energies and a local CR component that has a contribution from nearby sources (Thoudam & Hörandel, 2013). We follow the procedure put forward in Thoudam (2008) for our analysis.

The background CR component is assumed to originate from distant particle accelerators distributed uniformly throughout the Galaxy. Conversely, the local, time-dependent CR component is considered to be produced from the nearby SNRs that lie within ~ 1 kpc from the Earth. Satyendra (2006) showed that the temporal density variations of CR particles at a given location in the Galactic disc are significant only due to a source located at a distance of ≤ 1 kpc (see their Fig. 3), hence we consider all the sources within this 1 kpc radius contribute significantly to the observed excess CR flux at Earth. For the background component, the CR diffusion region is taken to be a cylindrical volume with a radial boundary of $R = 20$ kpc and a vertical height of $\pm H$. The precise value of H remains uncertain. Estimates derived from various CR propagation models span a broad range of $2 - 12$ kpc (Strong & Moskalenko, 1998; Webber & Soutoul, 1998). We consider a typical value of $H = 5$ kpc.

In contrast, for the local CR component, we assume a diffusion region that is not constrained by any boundary. This assumption is justified because the CR spectrum originating from nearby sources remains unaffected by either vertical or radial boundaries. It is because of their very short propagation time to the Earth (since the sources we consider here, are distributed within 1 kpc distance from Earth) relative to the escape times from the Galactic boundaries (Thoudam, 2008). The propagation time ($t \approx L^2/4D$) for a TeV proton from 1 kpc distance is ≈ 0.2 Myr (using a diffusion coefficient $D = 1.72 \times 10^{28} (E/3\,\mathrm{GeV})^{0.5}$ cm^2 s^{-1}), which is much shorter than the confinement time of ≈ 10 Myr of CRs. The age and distances of the SNRs within a 1 kpc radius are mentioned in table 4.1.

SNR name	Distance (kpc)	Age (yr)	Ref.
Geminga	0.25	3.4×10^5	a,b
Loop1	0.17	2×10^5	c
Vela	0.30	10^4	d
Monogem	0.30	6.8×10^4	e
Cygnus Loop	0.73	2×10^4	f
G 114.3+0.3	0.70	8×10^3	g
Vela Junior	0.70	3.7×10^3	h,i
S147	0.90	3×10^4	j
HB9	0.80	8×10^3	k
HB21	0.80	1.5×10^4	l
SN185	0.95	1.8×10^3	m

Table 4.1 List of supernova remnants within a distance of 1 kpc from the Earth. The references are: (a) Faherty et al. (2007), (b) H. E. S. S. Collaboration et al. (2023), (c) Dickinson (2018), (d) Sushch et al. (2011), (e) Cappiello et al. (2023), (f) Fesen et al. (2018), (g) Yar-Uyaniker et al. (2004), (h) Maxted et al. (2018), (i) Berezhko et al. (2009), (j) Gvaramadze (2006), (k) Leahy & Tian (2007), (l) Lazendic & Slane (2006), (m) H. E. S. S. Collaboration et al. (2018a).

4.2.1 Cosmic rays from nearby sources

After getting accelerated at sources, CRs propagate through the ISM. This transport of CRs in the Galaxy originating from a single nearby source can be expressed by the time-dependent diffusion equation,

$$\nabla\cdot(D\nabla N_p)+Q=\frac{\partial N_p}{\partial t}\,, \tag{4.1}$$

where $N_p(r,E,t)$ denotes the number density of CR primary particles of kinetic energy per nucleon E at a distance r from the source at any given time t after their release, and $D(E)$ is the diffusion coefficient of CRs in the Galaxy. In Equation 4.1, we neglect losses due to the interaction with the interstellar matter since the time for CRs to reach the Earth from the nearby sources (considered to be those located within 1 kpc in the present study) is expected to be much less than the CR interaction time scale with the interstellar matter. For instance, the interaction time for 1 TeV protons $t\approx(n_d\sigma c)^{-1}\sim 30$ Myr for a matter density of $n_d\approx1$ cm^{-3}, is much larger than the propagation time of ≈ 0.2 Myr to the Earth from a source at 1 kpc for typical value of $D(E)$. We also neglect effects that are important mostly at low energies such as re-acceleration, ionization losses, and convection by the Galactic wind.

In the standard theory of diffusive shock acceleration (DSA), charged particles undergo acceleration each time they traverse the shock front of a supernova. Throughout this acceleration process, a minor portion of the particles are carried downstream of the shock and are unable to undergo further acceleration, whereas a significant portion diffuses upstream. These particles may then be recaptured by the expanding shock and continue their acceleration. Therefore, the particles are accelerated efficiently when they are confined near the shock in the upstream region. The confinement is actually due to the presence of magnetic turbulence generated around the shock. Particles remain confined as long as their upstream diffusion length $l_d = D_s/\upsilon_s$ (D_s is upstream diffusion co-efficient and υ_s is the shock speed) is less than the radius of the shock R_s (Thoudam & Hörandel, 2012a). The diffusion coefficient is expected to scale with energy as E^δ so that the diffusion length is expected to be proportional to energy as $l_d = E^\delta/\upsilon_s$, where δ is a positive constant. This shows that high-energy particles can escape at early stages of the evolution of the SNR, whereas low-energy particles are released at later stages when the shock becomes weak. Keeping this energy-dependent escape scenario in mind, in our model, the CR escape time has been parameterized as (Gabici et al. 2009),

$$t_{\rm esc} = t_{\rm sed}\left(\frac{AE}{Ze\rho_m}\right)^{-1/\alpha}, \tag{4.2}$$

where $t_{\rm sed}$ is the time associated with the onset of the Sedov phase of the SNRs, α is a positive constant whose value is taken as 2.4, which has been determined by the spectral fitting in Thoudam & Hörandel (2013), and $\rho_m = 1$ PV is the maximum rigidity (Berezhko, 1996). This equation indicates that the highest energy particles escape at the onset of the Sedov phase, with progressively lower energy particles escaping as time advances. In terms of physical properties, a greater value of α results in reduced confinement within the remnant, whereas a smaller D leads to a longer time for CRs to travel to Earth. Equation 4.2 implies that for a given energy E, heavy nuclei escape at a relatively early epoch compared to protons, with a time scale that is shorter by a factor of $(A/Z)^{-1/\alpha}$. Note that, this time-dependent escape of CRs is crucial for our model to explain the spectral hardening of protons and helium in the TeV range. Moreover, the early escape of heavier nuclei is the key to explaining the observed spectral hardening of heavier nuclei at lower energy/nucleon than the protons.

As discussed above, SNRs can confine high-energy particles during the early stage of their evolution. At a later stage, the shock becomes much weaker, cannot accelerate particles, and can no longer confine particles because the turbulence level goes down around the shock. We assume that all the low-energy particles will escape from the remnant at 10^5 yr when the shock becomes too weak. Details of this aspect of particle escape can be found in Caprioli et al. (2009). The CR escape time can be expressed as $T_{\rm esc} = \min\left[t_{\rm esc}(E), 10^5\ {\rm yr}\right]$. The corresponding escape radii can be calculated using the age–radius Sedov relation for SNRs which follows $R \propto t^{0.4}$. A detailed derivation provides the radius explicitly as (Thoudam & Hörandel, 2013):,

$$R_{\text{esc}} = 2.5 \upsilon_0 t_{\text{sed}} \left[\left(\frac{T_{\text{esc}}}{t_{\text{sed}}} \right)^{0.4} - 0.6 \right] , \tag{4.3}$$

where υ_0 is the initial shock velocity. We consider the SNR to be spherically symmetric. If we assume that the CRs are distributed uniformly on the the surface of the SNR before they are released, the spatial source term Q in equation 4.1 can be expressed as,

$$Q(r,E,t) = \frac{q(E)}{4\pi R_{\text{esc}}^2} \delta(r - R_{\text{esc}}) \delta(t - T_{\text{esc}}) . \tag{4.4}$$

The two delta functions specify that the source term Q is non-zero only under specific conditions: when the SNR radius r equals the escape radius (i.e $r = R_{\text{esc}}$) and when the time equals the escape time (i.e $t = t_{\text{esc}}$). For a particle with energy/nucleon E, it escapes the SNR at a time determined by the equation 4.2 with the corresponding SNR radius at that moment calculated using equation 4.3. These values are then substituted into equation 4.4 to evaluate Q. Here, $q(E)$ is the source spectrum which can be expressed as,

$$q(E) = Aq(U) = Af \times (U^2 + 2Um)^{-(\gamma+1)/2} (U + m). \tag{4.5}$$

where $U = AE$ is the total kinetic energy of the particle, m is the rest mass energy of the particle, γ is the spectral index of the source term, and f is a constant that has been considered as a parameter in our model, that represents the injection energy of CR particle. The value of f essentially denotes the fraction of the total kinetic energy that goes into CR nuclei. These parameters f and γ can be obtained by matching the theoretical prediction with observations. Following Thoudam & Hörandel (2012a), the solution of Equation 4.1 can be written as,

$$N_p(r,E,t) = \frac{q(E) R_{\text{esc}}}{r A_{\text{esc}} \sqrt{\pi D(t - T_{\text{esc}})}} \exp \left[- \frac{R_{\text{esc}}^2 + r^2}{4D(t - T_{\text{esc}})} \right] \times \sinh \left[\frac{r R_{\text{esc}}}{2D(t - T_{\text{esc}})} \right] . \tag{4.6}$$

This equation is valid only for time $t \geq T_{\text{esc}}$, the CR flux from nearby sources for $t < T_{\text{esc}}$ is taken to be zero. Here $N_p(r,E,t)$ denotes the differential number density of CR primary particles at a distance of r from the SNR and $A_{\text{esc}} = 4\pi R_{\text{esc}}^2$ is the area of the SNR corresponding to the escape time of CRs of kinetic energy/nucleon E.

The value of the onset of Sedov time t_{sed} depends on the initial shock velocity of the SNR shock (υ_0), the initial ejecta mass (M_{ej}), and the ambient ISM density (ρ), as $t_{\text{sed}} \approx (3M_{\text{ej}}/4\pi\rho)^{1/3} \upsilon_0^{-1}$. Typical values of Sedov time lie in the range $\sim 10^2 - 10^3$ yr. We consider a uniform value of $t_{\text{sed}} = 500$ yr for all of the nearby sources, and the initial shock velocity

$\upsilon_0 = 10^4$ km s^{-1} (Thoudam & Hörandel, 2013). The CR escape time is estimated to be in the range $T_{\rm esc} = (500 - 10^5)$ yr and the value of $R_{\rm esc} \sim (5 - 100)$ pc. For nearby sources, we employ identical injection efficiency and source index for a particular CR species as utilized in the background component calculation. Additionally, in our study, we assume that all nearby SNRs share the same set of model parameters. This is physically motivated because we are considering the same type of sources (which are SNRs) for both the nearby and the diffuse background components. Hence the physics behind the acceleration is the same and to keep consistency we took the same parameters.

4.2.2 Cosmic rays from Background sources

The background primary CR component can be calculated from the time-independent (i.e steady-state) diffusion-loss equation:

$$\nabla \cdot [D\nabla N_p(E)] - n_s \upsilon \sigma \delta(z) N_p(E) = -Q(E) \,. \tag{4.7}$$

Here, $N_p(E)$ represents the differential CR primary number density with the kinetic energy/nucleon E. The first and second terms on the left side represent the diffusion from sources and the energy loss due to collisions of CRs with ISM particles respectively. Here n_s is the averaged surface density of ISM, υ is the CR particle velocity, and $\sigma(E)$ is the inelastic collision cross-section. The uniform distribution of background sources is represented by $Q(E) = Sq(E)\delta(z)$, where S is the uniform surface density of supernova explosion rate in the Galactic plane, E is the kinetic energy per nucleon, and $q(E)$ is the source spectrum (defined in section 4.2.1, we use the same source spectrum for both background and local components). Following Thoudam (2008), equation 4.7 can be solved analytically using the Green's function method and the solution at $z = 0$ is,

$$N_p(0,E) = \frac{RSq(E)}{2D} \int_0^\infty \frac{J_1(KR)}{K\coth(KH) + \frac{n\upsilon\sigma}{2D}} \, dK \,. \tag{4.8}$$

Here, J_1 denotes the Bessel function of first order and R is the radial boundary of the source distribution which is taken to be 20 kpc. The collision cross-section has been taken from Thoudam & Hörandel (2013). Here, S is the supernova frequency, H is the CR halo height, and $q(E)$ is the source spectrum as discussed above. The solution here is derived using the Green's function method. This approach involves performing a Fourier transform to transition from real space to wave vector space, commonly referred to as K-space. To obtain the final solution, an inverse transformation is required, achieved through integration over K. Note that the solar system is slightly offset from the galactic midplane, positioned about $5 - 30$ pc above

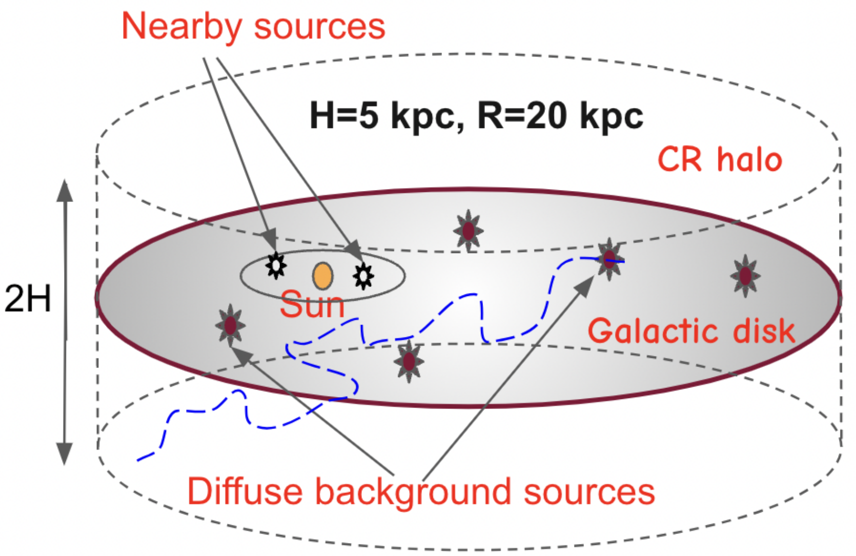

Fig. 4.1 The distribution of background and nearby sources (SNRs) on the Galactic plane. The circular region around the sun shows the 1 kpc radius and the sources within this radius are treated as the nearby CR sources. The propagation of CRs from an SNR is shown by the blue dashed line for illustration purposes.

it. However, when compared to our box height of approximately 5 kpc, this displacement is negligible. Thus, we approximate the solar system's position as $z = 0$, simplifying the calculations.

Primary CRs produce secondary particles due to spallation while they interact with ISM particles during their propagation. The secondary CR production rate can be calculated as

$$Q_s(r,E) = \int_E^\infty \eta \upsilon_p N_p(r,E')\delta(z)\frac{d\sigma_{ps}(E,E')dE'}{dE'} \tag{4.9}$$

where the suffix 's' indicates secondary species, N_p signifies the primary CR number density, σ_{ps} is the total spallation cross-section of the primary to the secondary and $d\sigma_{ps}(E,E')/dE'$ denotes the differential cross-section for generating a secondary nucleus with an energy per nucleon E from the spallation of a primary nucleus with energy per nucleon E'. As a whole the term on the right side of equation 4.9 represents the interaction of primary cosmic rays with interstellar matter. These collisions result in the production of new particles, which are generated as secondary products of the interaction. Given the conservation of energy per nucleon during the spallation process, the differential cross-section can be formulated as,

$$\frac{d\sigma_{ps}(E,E')}{dE'} = \sigma_{ps}\delta(E'-E) \tag{4.10}$$

The propagation of secondaries follows a similar-type equation that describes their primaries as given by equation 4.7, only the source term replaced by equation 4.9. The differential number density of CR secondaries is given by Thoudam (2008),

$$N_s(0,E) = \eta \upsilon_p \sigma_{ps} N_p(0,E) \frac{R}{2D_s} \int_0^\infty \frac{J_1(KR)\,dK}{K\coth(KH) + \frac{n\upsilon_s\sigma_s}{2D_s}}, \tag{4.11}$$

where $N_p(0,E)$ is calculated using equation 4.8. This gives the spectrum of secondary CRs measured at Earth. For the calculation of secondary particles, we only consider the spallation of the diffuse background of primary CRs but not the primary CRs originating from nearby sources for the following reason: the interaction time scale of CRs from nearby sources is much higher than the time required to reach Earth. Therefore those CRs will not produce any secondary particles during their propagation.

Our study focuses on boron as the secondary product due to spallation. In secondary boron production, we focus solely on the ^{12}C and ^{16}O primaries due to their predominant role in boron production within the Galaxy. These primaries undergo spallation, generating isotopes (^{11}B,^{10}B) and (^{11}C,^{10}C). The latter subsequently decay into (^{11}B,^{10}B), thus enhancing boron production.

4.2.3 Secondary-to-primary ratio from background cosmic rays

The secondary-to-primary ratio for the background CRs can be calculated using Equation 4.11. The ratio, $N_s/N_p \propto 1/D_s$, is used to determine an initial estimate of the diffusion coefficient in the Galaxy. For the present study, we model $D(E)$ in the form of,

$$\begin{aligned} D(E) &= D_0\left(\frac{\upsilon}{c}\right)\left(\frac{E}{E_0}\right)^{\delta}, \quad E \leq E_1 \\ &= D_0\left(\frac{\upsilon}{c}\right)\left(\frac{E}{E_1}\right)^{\delta_1}\left(\frac{E_1}{E_0}\right)^{\delta}, E > E_1 \end{aligned} \tag{4.12}$$

where υ is the particle velocity, D_0 is the normalisation constant. The introduction of the break at energy E_1 is necessary to explain the fact that B/C ratio slightly hardens at higher energies. Optimizing Equation 4.12 to match the recent boron-to-carbon ratio (B/C) from the AMS-02 experiment (Aguilar et al., 2018a), we obtain $D_0 = 1.72 \times 10^{28}$ cm^{2}s^{-1}, $E_0 = 3$ GeV, $\delta = 0.5$, $\delta_1 = 0.4$ and $E_1 = 100$ GeV (see Figure 4.1). This set of parameters for $D(E)$ of the three different optimization models considered in this work is described in detail in Section 4.2.4. Note that these values, in particular D_0, which are obtained purely based on the background

CRs for now, will be further modified by adding the contribution of CRs from the nearby sources (see Section 4.2.4).

It may be noted that recent measurements of B/C by the CALET (Adriani et al., 2022b) and DAMPE (Dampe Collaboration, 2022) experiments show an indication of flattening of the ratio above ~ 1 TeV. Such a flattening may be an effect of the re-acceleration of CRs by strong shocks associated with young SNRs during their propagation in the Galaxy (Wandel et al., 1987; Blasi, 2017) or the production of secondaries inside the source region from the nuclear interaction of primary nuclei with local matter (Berezhko et al., 2003; Cowsik & Burch, 2010). Neither of these mechanisms affects the spectral shape of the steady/background primaries. However, the shape of the background secondaries can be affected, particularly at high energies, due to the generation of an additional component of secondaries with a source spectrum similar to that of the primaries and much flatter than that of the secondaries produced in the ISM. In the present study, we neglect the flattening in B/C at TeV energies since it does not affect the major results presented here, which focus on the spectra of the primary CRs and the all-particle spectrum.

4.2.4 Different scenarios for explaining the bump and B/C ratio

We consider three different scenarios for our analysis. These different scenarios have been considered based on the measured secondary to primary (B/C) ratio and the observed spectral bump in the individual element spectra, especially for proton and helium.

In our first model, we calculate the primary to secondary (B/C) ratio following the procedure mentioned in section 4.2.3. In our second model, we include the contribution of nearby sources for the calculation of the B/C ratio. As we mentioned earlier in section 4.2.1, the interaction term is not considered in equation 4.1, which implies there is no production of CR secondaries from the primaries generated from nearby sources, however, the contribution of primaries is included. Boron is produced as a secondary product from CR primaries that are generated from diffuse background sources. Thus the B/C ratio is given by

$$\frac{B}{C} = \frac{B_{\rm bg}}{C_{\rm bg} + C_{\rm nearby}} . \tag{4.13}$$

Here, the quantity with subscripts *bg, nearby* denotes the background contribution and contribution from nearby sources, respectively. Therefore if we include the primary CR contribution from nearby sources (in this case, carbon), it will increase the denominator, but the numerator remains unchanged (as there is no secondary production in the case of nearby sources), which will eventually decrease the observed B/C ratio. By changing the constant term D_0 (see equation 4.12), one can readjust the B/C ratio to match the observed ratio. Following this procedure,

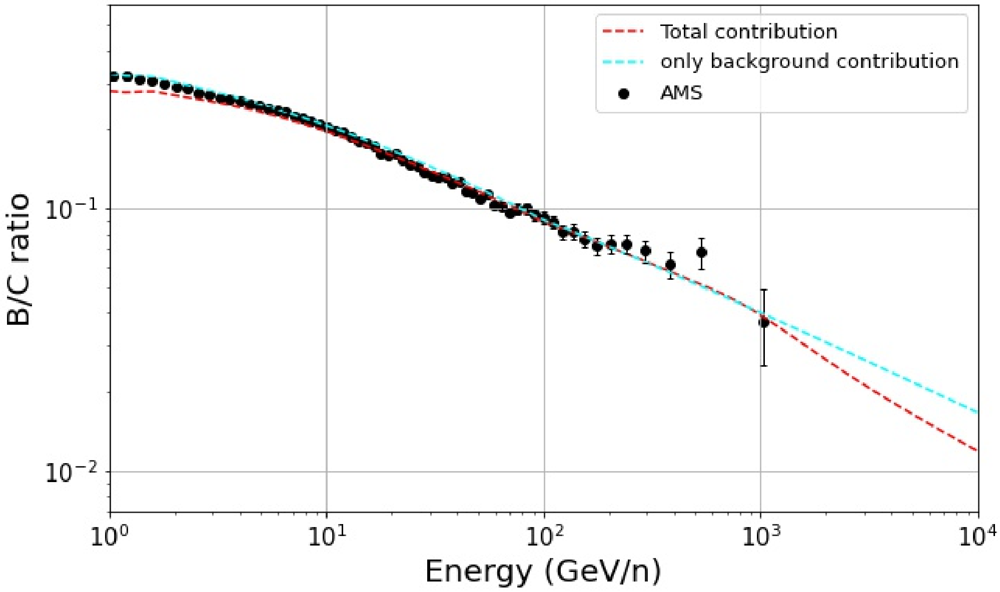

Fig. 4.2 Boron to carbon ratio measured by AMS02 (Aguilar et al., 2018a). The blue dashed line shows our model prediction considering only the contribution of CRs from a diffuse background and excluding the nearby sources. The red dashed line shows our model prediction, where we include both the nearby and background contributions for the primaries but only the background contribution for secondaries (see Eq. 4.13).

we obtain $D_0 = 1.56 \times 10^{28}$ cm^{2}s^{-1} (see equation 4.12). The calculated ratio of B/C is shown in figure 4.2. In this work, we do not focus on data below 10 GeV. In the low-energy region, various physical phenomena such as solar modulation, ionization losses, and the effects of convection due to Galactic winds play significant roles, which are not accounted for in our simplified model. Therefore, our analysis is restricted to energies above 10 GeV. The value of $D_0 = 1.56 \times 10^{28}$ is slightly lower than the value mentioned in section 4.2.5. Note that, we use this D_0 for the calculations of individual element spectra. Comparing the red and blue dashed line in figure 4.2, one can see the effect of adding the nearby sources on the B/C ratio, particularly above 1 TeV. Due to the significant contribution of CR primaries because of the nearby sources above 1 TeV, the calculated B/C ratio decreases and the ratio becomes steeper above 1 TeV. This is because nearby sources only contribute to the carbon flux, but not to boron.

In this work, we follow three different approaches for calculating and modeling the CR spectra as described below. Our exploration of different models is admittedly not exhaustive, but the models aim to show the sensitivity of our results to various model assumptions that are only weakly constrained.

Model 1 (B/C optimization model): Here, we optimize the individual element spectra and B/C ratio separately. This involves determining an appropriate diffusion coefficient by aligning our calculated B/C ratio with the measured B/C ratio (as depicted in Figure 4.2). We then utilize this diffusion coefficient in calculating the individual elemental spectra. The remaining parameters, such as injection spectral index and efficiency, are adjusted to match the calculated elemental spectra with observations. This method yields the following diffusion coefficient parameter values: $\delta = 0.50$, $\delta_1 = 0.40$, $E_1 = 100$ GeV/n.

Model 2 (B/C+spectra optimization model): In this approach, we conduct the optimization simultaneously over both the individual spectra and the B/C ratio. Note that, this method differs from the previous one in that in the previous method we determine the parameters of diffusion coefficient independently of the individual element spectra, however in this second method diffusion parameters are determined through the concurrent fitting of B/C ratio, proton, and helium spectra. For this approach, we find that $\delta = 0.50$, $\delta_1 = 0.45$, and $E_1 = 50$ GeV/n provided a satisfactory alignment with observations.

Model 3 (Diff-nearby-sources model): Here, we estimate the background cosmic-ray contribution using the approach from the first method, but employ a distinct diffusion coefficient ($D(E)$) for local sources. Here, we utilize $\delta = 0.50$, $\delta_1 = 0.40$, $E_1 = 100$ GeV/n for background sources and $\delta = \delta_1 = 0.50$, $E_1 = 100$ GeV/n for nearby sources. These three calculation methods are respectively referred to as Model 1 (B/C optimization model), Model 2 (B/C+spectra optimization model), and Model 3 (Diff-nearby-sources model) in this study, with the results of each presented and compared in the subsequent discussion.

4.2.5 Other model parameters

Given our assumption that interstellar matter is distributed within the thin Galactic disc, it is more relevant to use the surface matter density on the disc rather than the actual number density in our study. The average surface matter density of atomic hydrogen has been taken as $n_s = 5.17 \times 10^{20}$ atoms cm^{-2} (Thoudam & Hörandel, 2013), estimated from atomic and molecular observations near the solar position in the Galaxy. We add 10% to this value to take into account helium. The supernova surface density has been assumed as $S = 7.7$ Myr^{-1} kpc^{-2} (see equation 4.8), which corresponds to a supernova rate of 0.98 per century in the Galaxy. This value of supernova rate is consistent with 1.9 ± 1.1 per century, as inferred by Diehl et al. (2006). In our model, this supernova rate has been treated as a parameter and determined by matching the calculated spectra with observations. We also consider the effect of solar modulation assuming the force field approximation with modulation parameter $\phi = 350$ MV, which is slightly lower than the value used in Gleeson & Axford (1968). This value has been determined by fitting our calculated proton and helium spectra with the lower energy data points measured by AMS02 (Aguilar et al., 2018b) and PAMELA (Adriani et al., 2011).

4.3 Results on cosmic-ray spectra

In this section, we present the results on the individual element spectra and the all-particle CR spectra for each of the models discussed above, and compare the results.

4.3.1 Individual element spectra

Proton & helium spectra: Figure 4.3 shows the predicted flux measured at Earth for protons (top panel) and helium (bottom panel) using Model 1 (B/C optimization model). The blue dash-dotted line shows the background CR contribution and the black solid line represents the CR contribution from the nearby sources mentioned in Section 4.2.1. We use $\gamma_P = 2.34$, $f_P = 14.8\%$ for protons and $\gamma_{\mathrm{He}} = 2.28$, $f_{\mathrm{He}} = 1.52\%$ for helium, which are obtained from the best match fitting of observed spectra. These values produce a good fit for proton and helium spectra, respectively. The background CR component agrees well with the data up to TeV energies. However, the data shows some excess above 1 TeV and the background CR component is unable to explain this spectral hardening above ~ 1 TeV. This excess or hardening can be explained if we consider the additional contribution from nearby sources. From Figure 4.3, it is obvious that nearby sources show a dominant contribution above ~ 1 TeV, which can explain the spectral hardening measured by DAMPE (An et al., 2019; Alemanno et al., 2021) and CALET (Adriani et al., 2022a, 2023). At lower energies, the nearby contribution is dominated by Monogem and Loop 1, since these are much older SNRs, and at higher energies, the main contribution comes from Vela due to its relatively young age (see table 4.1). The absence of any component from Vela at lower energies is due to this young age of the SNR. This is the effect of the energy-dependent CR escape mechanism used in our model.

The CR flux also depends on the distance of the source. Despite being an older SNR, Geminga has a large distance (compared to Loop1 and Monogem) which results in a lower flux from this source. On the other hand, Vela Junior, SN185, and HB9 are younger SNRs and their distances are also large. Equation 4.6 ensures that the flux from these SNRs dominates only at a very high energy range, which can be seen from figure 4.3. Furthermore, the helium spectrum exhibits a hardening at lower energy per nucleon in comparison to the proton spectrum. This disparity, according to our model, is primarily ascribed to the earlier escape times of helium nuclei from the SNRs relative to protons. As elaborated in Section 4.2.1 of this chapter, our model predicts that a spectral hardening at lower energies per nucleon is anticipated for all

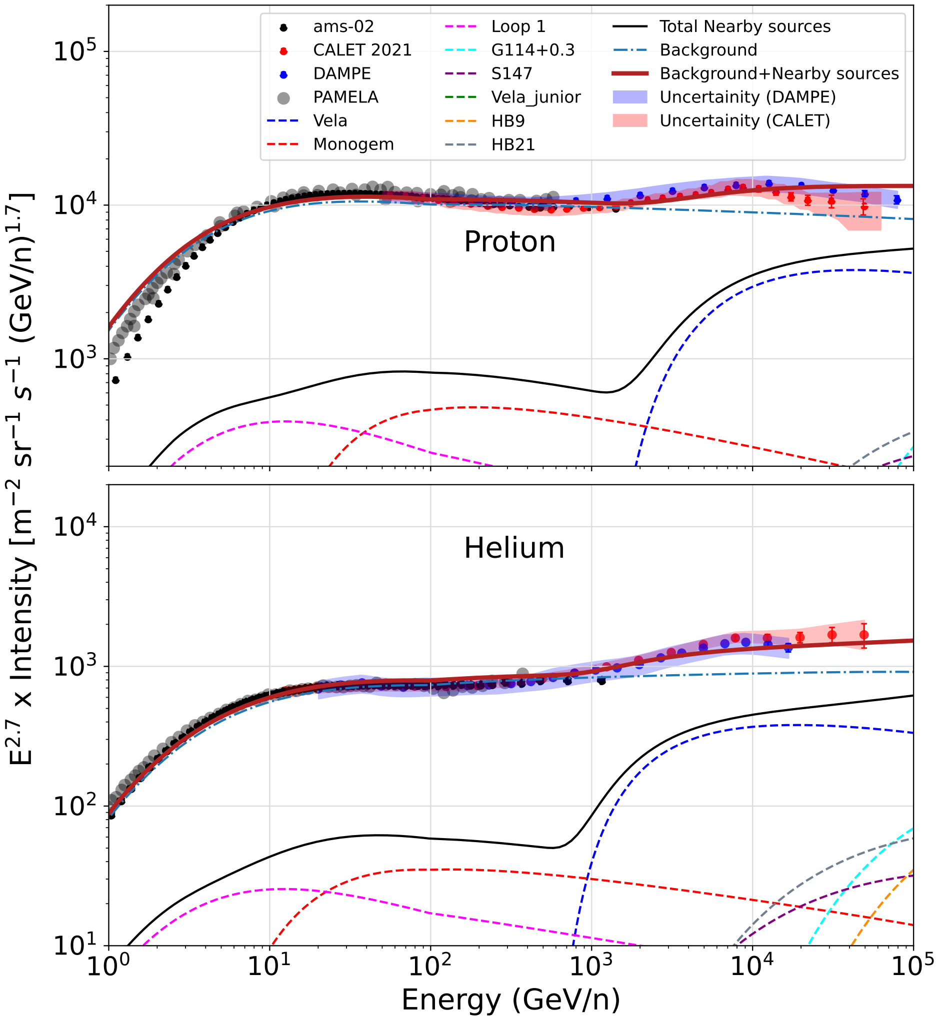

Fig. 4.3 Top panel: Proton spectra; bottom panel: helium spectra using Model 1 (B/C optimization model). The dash-dotted line shows the background CR component, the colored dashed lines show individual contributions from different SNRs, and the black solid line shows the nearby CR contributions. The solid maroon line shows the total (nearby+background) CR flux measured at Earth.

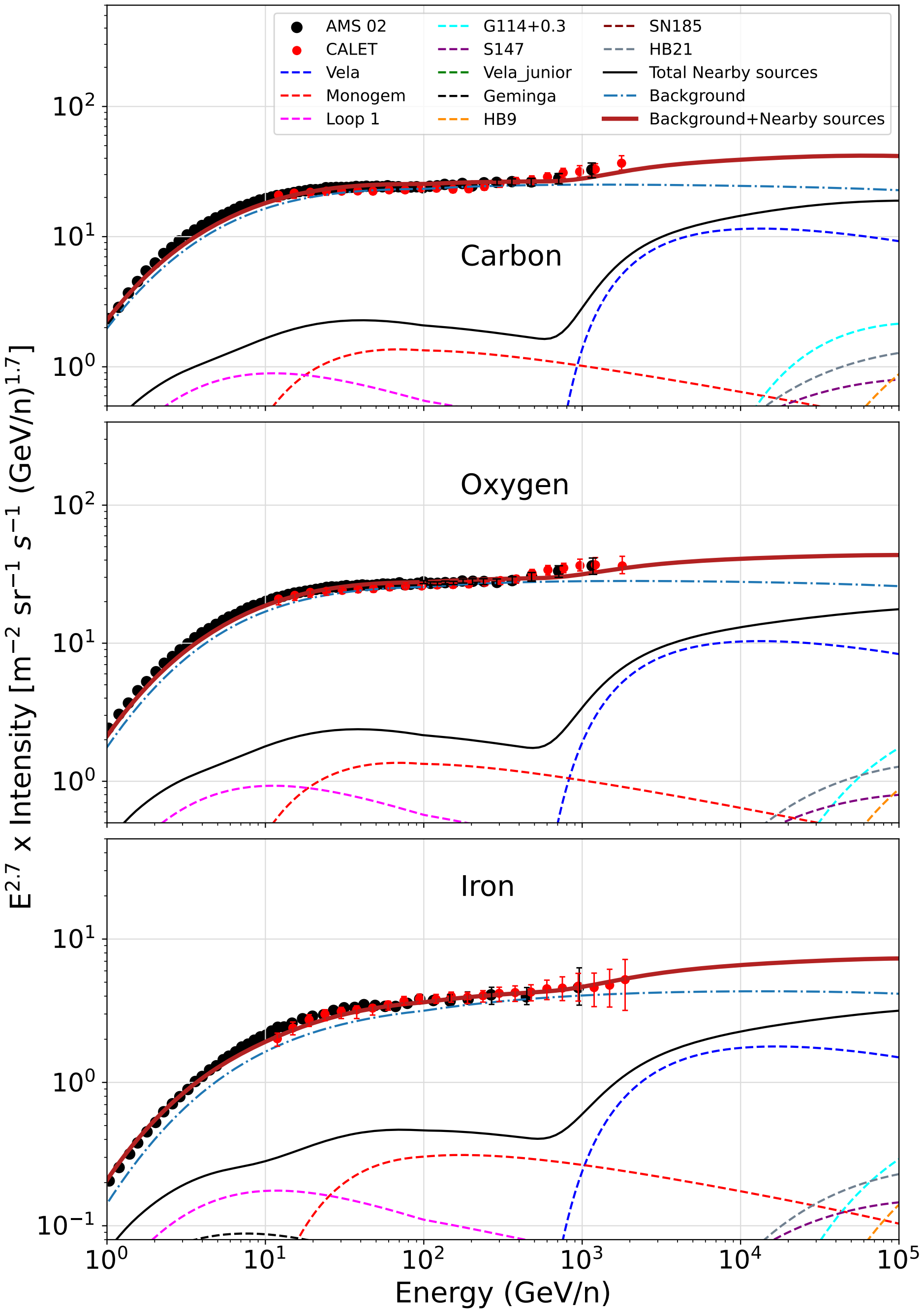

Fig. 4.4 Carbon (top), oxygen (middle), and Iron (bottom) energy spectra using Model 1 (B/C optimization model). Blue dash-dotted line: background spectrum, Black solid line: total nearby component, and the dashed colored lines: Individual source contribution. Thick-solid maroon line: total nearby plus background. The CALET data points have been shifted in energy by +8% for carbon and oxygen, and +6% for iron to minimize the systematic offset with respect to the AMS-02 data.

heavier elements. This occurs when their escape times are shorter than those of protons by a factor of $(A/Z)^{-1/\alpha}$ at equivalent energy per nucleon (see Eq. 4.2).

Heavier elements spectra: The spectra for heavier elements are shown in Figure 4.4 (carbon, oxygen, and iron) and Figure 4.5 (neon, silicon, and magnesium) using Model 1 (B/C optimization model). The results look similar to those obtained for the lighter nuclei in figure 4.3. Our model is consistent with these observations. For each of the heavier elements, there is a signature of spectral hardening few TeV/n, similar to the spectral hardening observed for proton and helium by the CALET (Adriani et al., 2022a, 2023) and CREAM (Yoon et al., 2011). This can also be explained by considering the contribution from nearby sources as shown above for proton and helium. The fitting parameters such as injection fraction, and spectral indices are mentioned in Table 4.2. Similar to proton and helium spectra, Vela has the most significant contribution around the spectral hardening. The observed spectral hardening for carbon, oxygen, and iron is accurately observed by CALET, however, the CREAM data shows a possible spectral hardening for neon, magnesium, and silicon, although this feature is not convincing due to the large error bars. This hardening feature for neon, magnesium, and silicon needs to be confirmed by future measurements. The measurements above a few times 10^3 GeV/n for neon, silicon, and magnesium are not very sensitive, as can be seen in large error bars, however, future sensitive measurements at high energies can provide a crucial check of our prediction for heavier elements.

We perform similar calculations for the other two optimization models. The required spectral indices, injection fraction for each element, and other parameters are listed in table 4.2, and the corresponding diffusion parameters have been discussed in section 4.2.4. The plot for proton and helium obtained using Model 2 (B/C+spectra optimization model) are shown in Figure 4.6 and for Model 3 (Diff-nearby-sources model) in Figure 4.7. We have not shown the heavier element plots for Model 2 (B/C+spectra optimization model) and Model 3 (diff-nearby-source model) as they are quite similar to Model 1 (B/C optimization model). The main difference can be seen in proton and helium, especially at higher energy and in the all-particle spectra. Using each of these different models the observed spectral bump can be explained. Note that In this study, the source indices span from $2.2-2.4$, showing a slightly steeper trend compared to the $2.0-2.2$ range predicted by standard DSA theory. In fact, an even higher value, approximately $2.4-2.5$, is suggested by the high level of CR isotropy observed within the range of around 1 to 100 TeV (Ptuskin et al., 2006).

4.3.2 All-particle spectra

The all-particle CR spectra for a wide range of energy can be calculated by combining all the different components of CRs (i.e. Galactic+extragalactic). For the CR component that

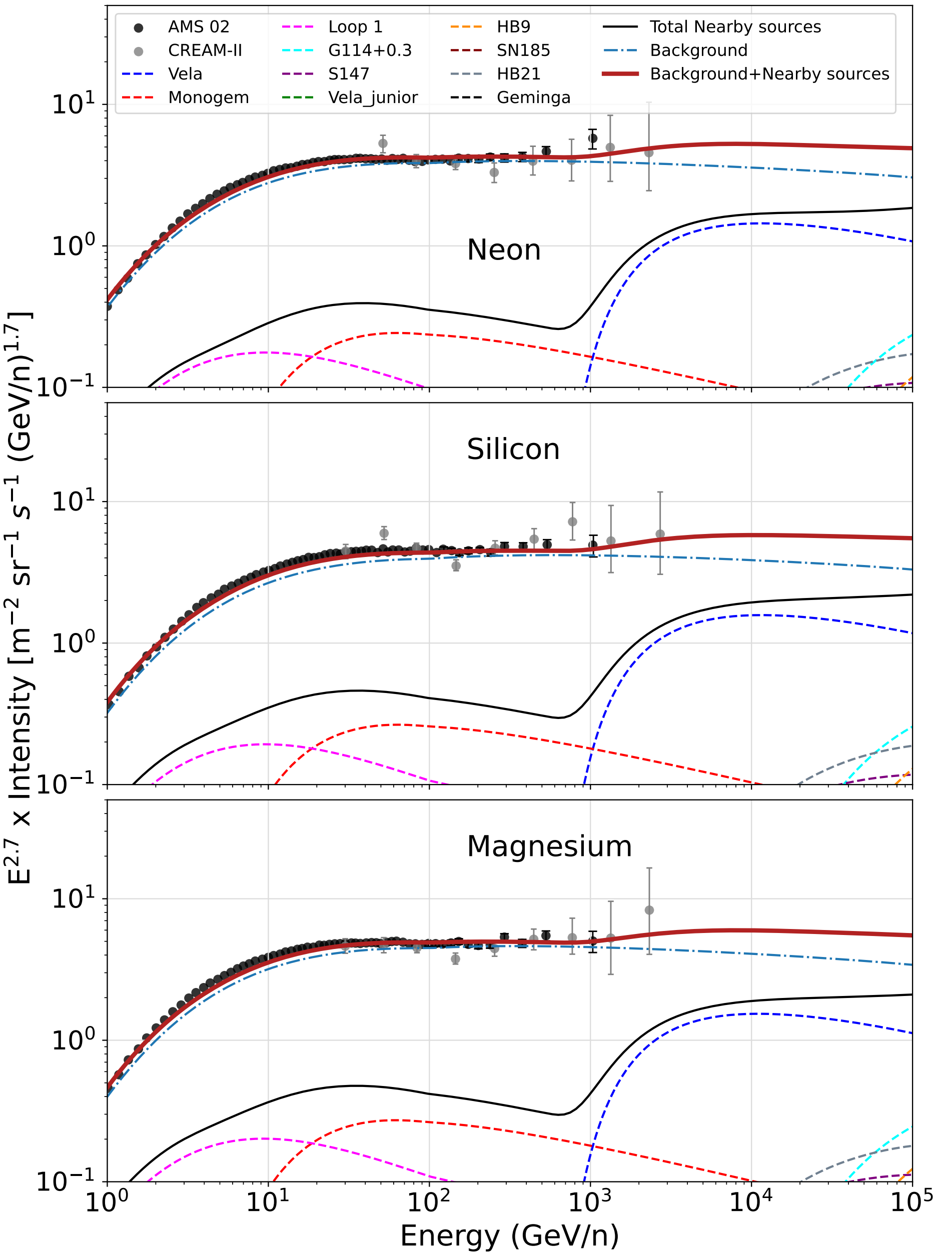

Fig. 4.5 Neon (top), silicon (middle), and magnesium (bottom) energy spectra using Model 1 (B/C optimization model). Blue dash-dotted line: background spectrum, Black solid line: total nearby component, and the dashed colored lines: Individual source contribution. Thick-solid maroon line: total nearby plus background. The CREAM data points have been shifted in energy by +11% for neon, silicon, and magnesium to minimize the systematic offset with respect to the AMS-02 data.

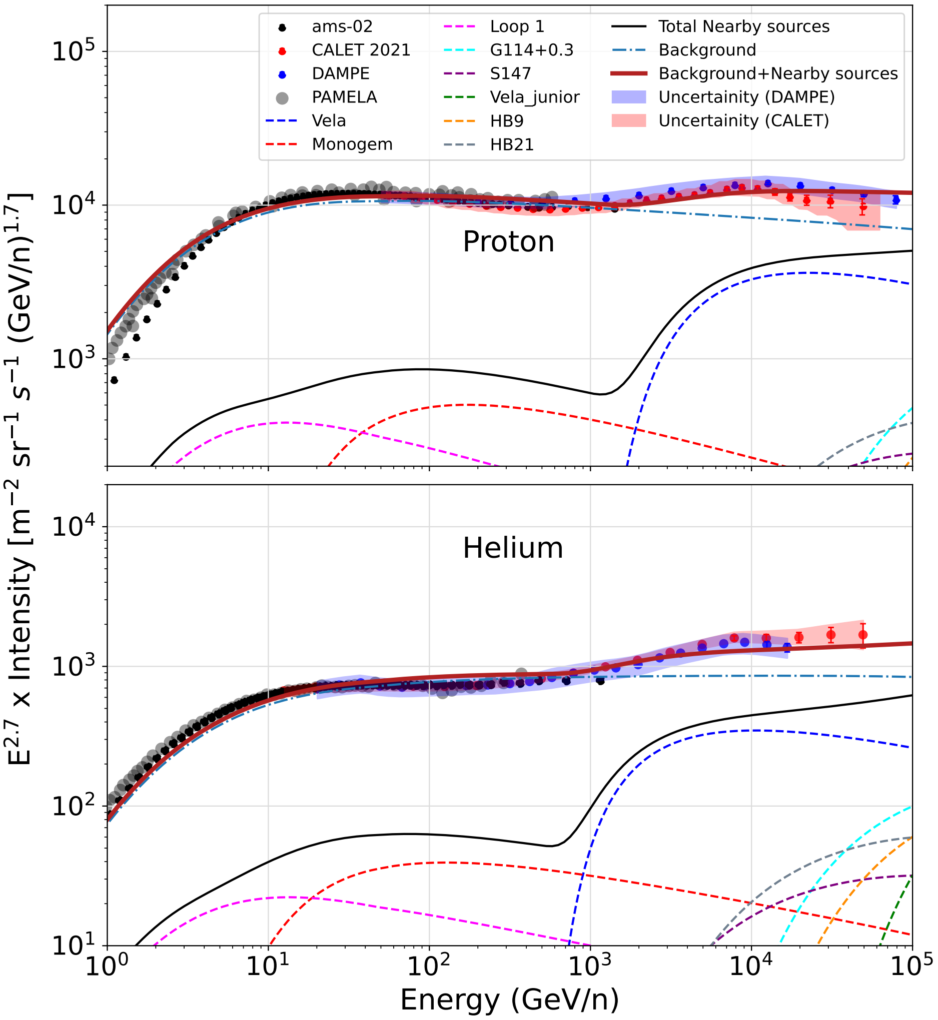

Fig. 4.6 Top panel: proton spectra; bottom panel: helium spectra using Model 2 (B/C+spectra optimization model). The dash-dotted line shows the background CR component, the colored dashed lines show individual contributions from different SNRs, and the black solid line shows the nearby CR contributions. The solid maroon line shows the total (nearby+background) CR flux measured at Earth

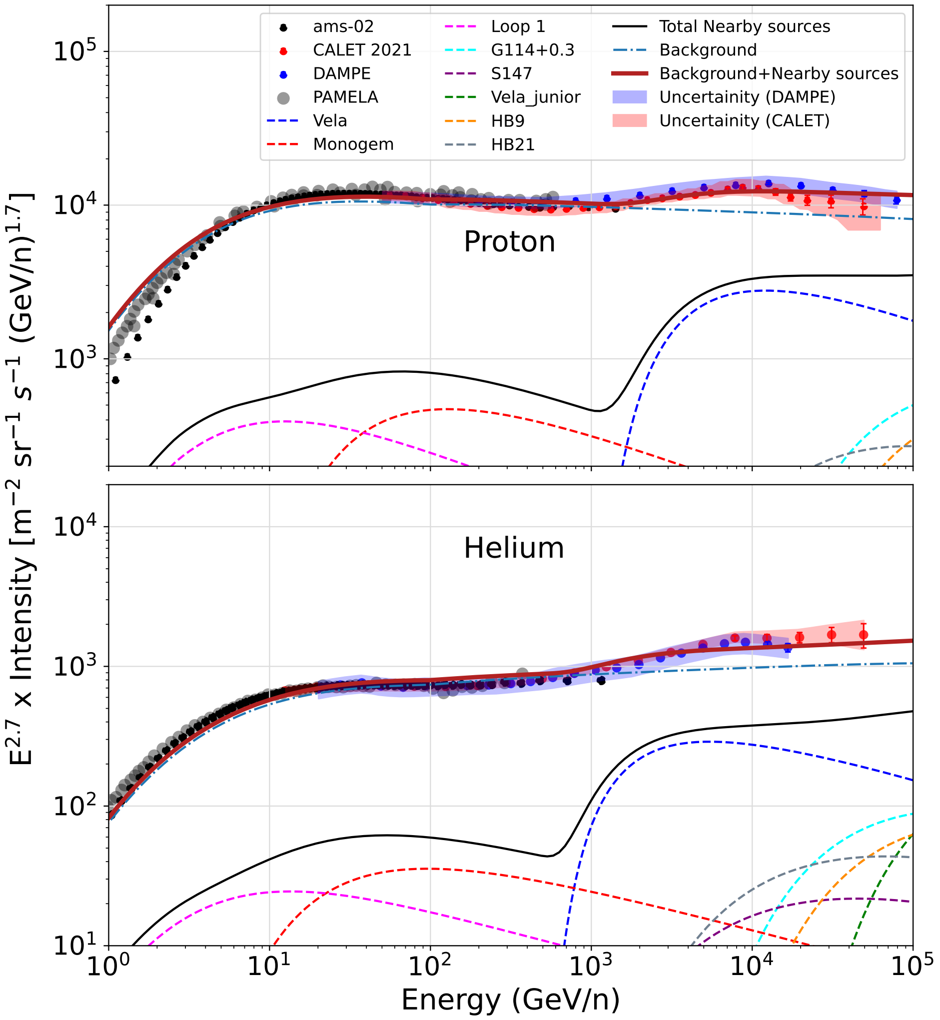

Fig. 4.7 Top panel: proton spectra; bottom panel: helium spectra using Model 3 (diff-nearby-source model). The dash-dotted line shows the background CR component, the colored dashed lines show individual contributions from different SNRs, and the black solid line shows the nearby CR contributions. The solid maroon line shows the total (nearby+background) CR flux measured at Earth.

	Model 1		**Model 2**		**Model 3**	
Diffusion parameters	$D_0 = 1.56 \times 10^{28}, \delta = 0.50$ $\delta_1 = 0.40, E_1 = 100$ GeV/n		$D_0 = 1.56 \times 10^{28}, \delta = 0.50$ $\delta_1 = 0.45, E_1 = 50$ GeV/n		$D_0 = 1.56 \times 10^{28}, \delta = 0.50, \delta_1 = 0.40$ (BG) $D_0 = 1.56 \times 10^{28}, \delta = 0.50 = \delta_1 = 0.50$ (Nearby)	
Elements	**index (γ)**	**efficiency (f)**	index (γ)	**efficiency (f)**	**index (γ)**	**efficiency (f)**
Proton	2.34	14.8	2.32	15.0	2.34	14.5
Helium	2.28	1.52	2.25	1.49	2.26	1.50
Carbon	2.33	0.054	2.31	0.053	2.34	0.054
Oxygen	2.33	0.055	2.31	0.054	2.34	0.054
Iron	2.33	0.012	2.31	0.010	2.34	0.011
Silicon	2.37	0.014	2.38	0.014	2.38	0.013
Neon	2.37	0.015	2.37	0.013	2.37	0.012
Magnesium	2.38	0.011	2.37	0.010	2.37	0.010

Table 4.2 Parameters for the discussion coefficient for different models and corresponding spectral indices and injection efficiency of different elements for all three assumed models.

originates from our assumed supernova distribution (both background+nearby), we use an exponential cut-off $\sim 6 \times 10^6 Z$ GeV for elements with the atomic number Z. As SNRs can not accelerate particles beyond the 'knee', it is necessary to add a second Galactic CR component to explain the observed data above 'knee' up to a few times 10^7 GeV. Hence, we also consider a second Galactic CR component that is being produced from a distribution of the young compact star clusters in our Galaxy (Bhadra et al., 2024), which dominates at a higher energy range, with an exponential cutoff $\sim 5 \times 10^7 Z$ GeV. This component is represented by the black dashed line in Figure 4.8). The calculated all-particle CR spectrum for all of the different models is shown in Figure 4.8. The data points around the 'knee' have been taken from IceTop (Aartsen et al., 2013) and Tibet III (Amenomori et al., 2008) experiments. Comparing the plots it is clear that Model 2 (B/C+spectra optimization model) and Model 3 (diff-nearby-source model) give a better match than Model 1 (B/C optimization model). Although Model 1 can explain the individual element spectra, however, it slightly over-predicts the total CR flux around the knee. Both the individual data of proton and helium as well as all particle data around the 'knee' can be explained well with Model 2 and Model 3. Hence, models 2 and 3 are slightly more favorable than Model 1.

4.4 Discussion

Explanation of the spectral bump: In this study, we show that the spectral bumps of the cosmic-ray protons and helium nuclei in the TeV region, recently observed by the DAMPE and CALET experiments, can be explained as an effect of the contribution of CRs from nearby SNRs within the proximity of $\sim$ 1 kpc, especially the Vela supernova remnant. In our model, the spectral bump is explained mainly as a result of a low-energy cut-off due to the energy-dependent escape of CRs from SNRs and a high-energy fall-off of the spectrum due to the

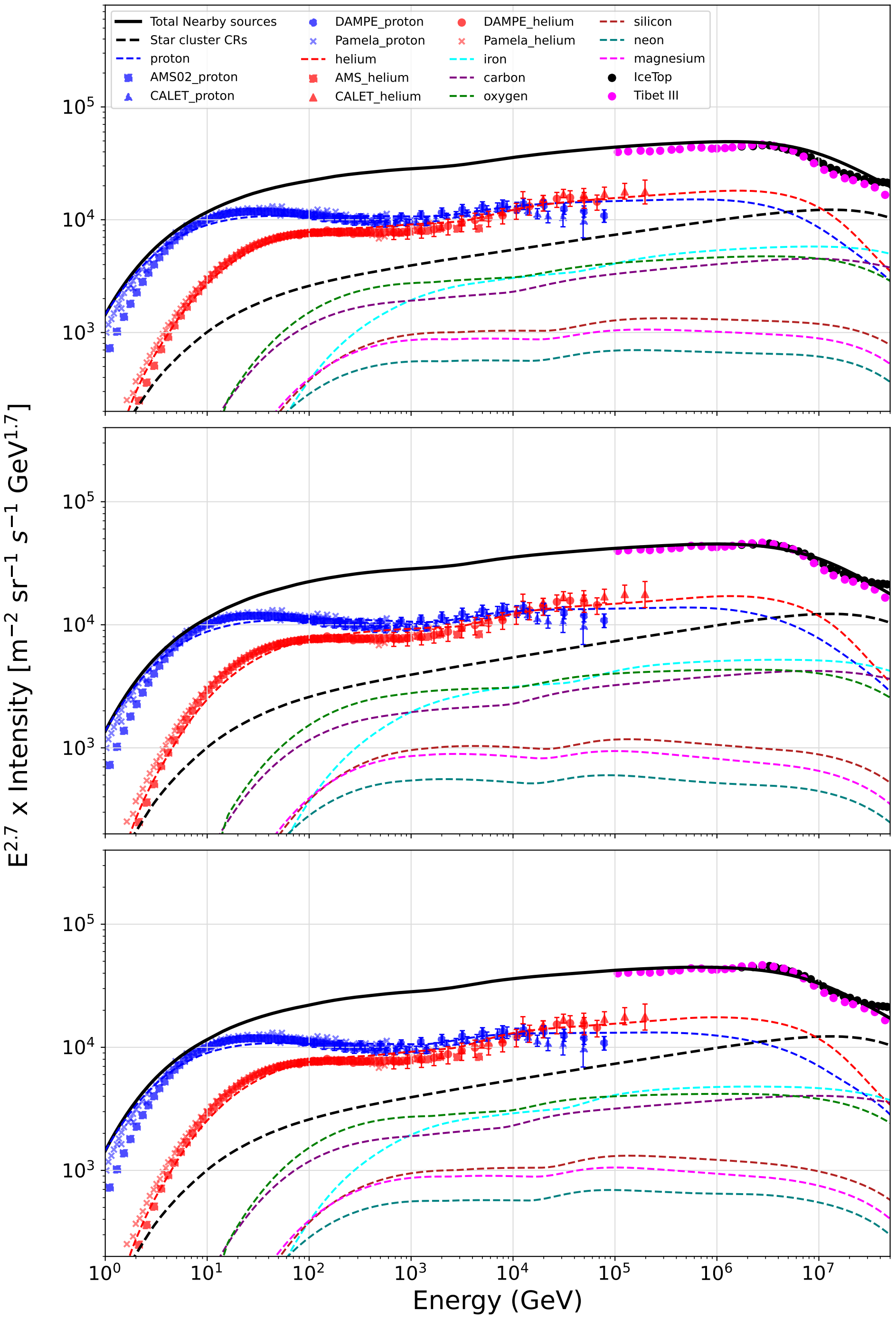

Fig. 4.8 The all-particle CR spectrum is shown by the black solid line. Top panel: Model 1 (B/C optimization model), Middle panel: Model 2 (B/C+spectra optimization model), Bottom panel: Model 3 (diff-nearby-source model). The contribution of different elements has been shown by thin-colored dashed lines. All particle data points have been taken from IceTop (Aartsen et al., 2013) and Tibet III (Amenomori et al., 2008) experiments.

energy-dependent propagation of CRs in the Galaxy. These results are in agreement with the earlier findings presented in Thoudam & Hörandel (2012d, 2013) in the context of the observed spectral hardening at $\sim (200-300)$ GeV/nucleon. In contrast, in a recent analysis, Li et al. (2024) identified other nearby sources such as Geminga, Monogem, and Loop I as the main contributors for the observed spectral bump. Their calculation differs from our approach in that we consider a more realistic energy-dependent escape time for particles from the sources while they assume an energy-independent burst-like injection. Moreover, we consider a more consistent approach by fixing the source parameters (spectral index and the CR injection energy) to be the same for all the nearby sources and the background component, while Li et al. (2024) allow the source parameters to vary among different nearby sources and also with respect to the background component. Our model is also shown to reproduce quite well the observed spectra up to ~ 2 TeV/nucleon for heavier elements up to iron. At the same time, it predicts a similar spectral bump for the heavier elements which can be tested with future observations at higher energies. In addition, our model reproduces the observed all-particle spectrum up to $\sim 10^8$ GeV when combined with a second Galactic component originating from compact star clusters (Bhadra et al., 2024).

Comparison with other existing models for the spectral hardening: The origin of the spectral bump is most likely connected with the spectral hardening observed at $\sim (200-300)$ GeV/nucleon. Several models have tried to explain the spectral hardening, but not all the models can easily explain the bump. For instance, an explanation based on a break in the diffusion coefficient (Tomassetti, 2012; Blasi et al., 2012) or on a hardened source spectrum (Yuan et al., 2011; Ptuskin et al., 2013) as well as model based on a global re-acceleration of CRs by weak shocks in the Galaxy (Thoudam & Hörandel, 2014) successfully reproduce the spectral hardening, but they cannot produce the observed bump unless multiple population of CR sources are invoked (e.g., Zatsepin & Sokolskaya, 2006; Yue et al., 2019). On the other hand, models based on the presence of nearby sources in addition to the background sources such as the one presented in this work (see also Thoudam & Hörandel, 2012d, 2013) or potential nearby CR re-acceleration sites as proposed in Malkov & Moskalenko (2021) can explain the spectral hardening and the bump at the same time. In our model, the bump is generated by CRs from a dominant nearby source (Vela) while the spectra beyond the bump ($E \gtrsim 5 \times 10^4$ GeV/nucleon) are dominated by the contribution from the background CRs and those produced by other nearby sources such as G114+0.3, HB9, and Vela Junior. At energies above the bump, this results in a slight flattening of the spectra of the individual elements until the spectra start to show a charge-dependent progressive cut-off in energy starting around the knee region in the all-particle spectrum (see Figure 4.8).

Effect of nearby sources on the B/C ratio: The presence of nearby sources can directly affect the secondary-to-primary ratios at the energies where their contribution to the primary CR spectra is significant. Secondary spectra remain unaffected as CR primaries from the nearby sources have to travel far distances in the Galaxy by the time they interact with the ISM and produce secondary CRs. This results in a negligible contribution of the secondaries produced by the primaries from nearby sources. This will lead to a suppression in the secondary-to-primary ratios at the energy range where the nearby sources show significant contributions in the primary spectra. This is visible in Figure 4.2 (red line) at energies above $\sim$ 1 TeV/n. However, at these energies, the ratio can also be strongly affected by CR re-acceleration by strong shocks in the Galaxy and the contribution of additional secondaries produced from the nuclear interaction of CR primaries inside the sources, none of which are included in the present study, as discussed in Section 4.2.3. Therefore, in reality, the steepening in the ratio caused by the presence of the nearby sources is expected to remain buried under other dominant effects mentioned above, making it hard to observe at high energies.

Effect on cosmic-ray anisotropy: The contribution of the nearby sources is also expected to produce some level of CR anisotropy at the Earth. For a single source dominating the CR flux at a given energy, the total anisotropy δ is calculated as (see Eq. 9 in Thoudam 2007),

$$\delta(E) = \frac{I_{\mathrm{m}}}{I_{\mathrm{T}}} \delta_{\mathrm{m}} \tag{4.14}$$

where I_{m} denotes the CR intensity from the dominant source at energy E and I_{T} is the total CR intensity (background plus nearby contribution) at that energy. The anisotropy from the dominant single source δ_{m} under the diffusion approximation is given by Mao & Shen (1972),

$$\delta_{\mathrm{m}} = \frac{3D}{c} \frac{|\nabla N_{\mathrm{m}}|}{N_{\mathrm{m}}} \tag{4.15}$$

where N_{m} is given by Equation (4.6) for a point source with distance r_{m} and age t_{m}. For our best-fitting proton results for Model 3 (diff-nearby-source model), we get $\delta \sim (0.61-3.1)\times 10^{-3}$ over the energy range of (1 – 100) TeV. Our estimates are larger than the measured anisotropy of $\sim (0.5-1)\times 10^{-3}$ by about a factor of $(1.2-3)$. The calculated anisotropy for proton for Model 1 is $\delta = (0.85-4.2)\times 10^{-3}$, and for Model 2 is $\delta = (0.78-3.8)\times 10^{-3}$, which are slightly larger than that of Model 1.

4.5 Conclusion

We have explored in detail the contribution of nearby SNRs to the observed flux of CRs at the Earth. Based on the results obtained in this work, we conclude that the spectral bump in the proton and helium spectra recently observed by the DAMPE and CALET experiments is most likely an effect of the contribution of nearby SNRs, in particular, the Vela SNR. The contribution of the nearby remnants is also found to be consistent with the observed CR spectra of the heavier elements from carbon to iron, and also with the all-particle spectrum at energies beyond the knee region when considered together with a background CR component produced by the distant sources.

5

Summary & Conclusions

In this thesis, we have studied young massive star clusters as potential accelerators for cosmic rays (CRs) especially in the TeV-PeV energy range. We use numerical PLUTO (Mignone et al., 2007) hydrodynamic simulation as well as analytical calculations to establish star cluster environments as particle acceleration sites. Continuous mass outflows from massive stars create a bubble-like structure around the core of the cluster. Particles can be accelerated in several regions within the stellar bubble. After getting accelerated, the propagation of these particles through space is a matter of extensive study. Using analytical and numerical calculations, we solve the particle propagation equation considering diffusion, energy loss due to interactions with ISM, and many other physical phenomena associated with it. The observed spectra at Earth and the actual spectra at the source can be significantly different due to these processes associated with particle propagation. For the lower energy regime i.e. up to a few hundred GeV we assume the CR production is dominated by the supernova remnants. Our focus has been on the higher energy (beyond PeV) where SNRs are insufficient to accelerate particles. On the basis of the recent γ-ray observations, we first demonstrated that the WD1 star cluster could be a potential site for CR acceleration (chapter 2). This finding motivated us to pursue a broader objective, where we considered a distribution of star clusters (each capable of individually accelerating particles) and estimated the total contribution from this collective distribution (Chapter 3). Also, we explored whether this component of CRs influences the observed all-particle spectrum beyond the 'knee' and explain observed spectral features in that region. Hence this thesis ties together a few strands in the study of cosmic ray acceleration in supernova remnants and star clusters. To complete the picture, one must also look at the lower energy segment of cosmic rays. In this case, it is the important contributions come from nearby supernova remnants. In our efforts to explain the spectral features of all particle CR spectra in the high-energy range (beyond PeV), our interest grew towards a recently observed spectral feature in the lower energy range, where the contribution from SNR CRs is dominant (chapter 4). With this interest, we aimed to explore the influence of nearby SNRs on the observed spectral features of various CR elements in the TeV-PeV energy range. Overall, we aim to gain a comprehensive understanding of the cosmic ray spectrum, spanning from the lowest to the highest energies. We now summarise the works presented in this thesis below in detail.

Cosmic rays from massive star clusters: a close look at Westerlund 1

In chapter 2, we performed 1-D two fluid hydrodynamical simulation to explain CR energy density around the young massive star cluster Westerlund 1 (WD1). We investigated various potential scenarios for CR acceleration within star clusters, including acceleration at the wind termination shock (WTS), the central free wind region, and the simultaneous occurrence of acceleration at both the WTS and central region. Additionally, alongside the continuous stellar outflow from young massive stars within the cluster, we considered the potential for multiple supernova-driven outflows in this environment. In each of these distinct scenarios, we computed the CR (CR) energy density and gamma-ray luminosity, accounting for their dependence on both the true radial distance and the projected distance from the center of the source. We explored the potential origins of gamma rays, encompassing both hadronic processes (such as proton-proton collisions leading to subsequent pion production and gamma ray decay) and leptonic mechanisms (inverse Compton scattering of high-energy background photons). Our analysis demonstrated that WD1 exhibits promising characteristics as a potential hadronic accelerator of CRs. Following the acceleration phase, we explore the propagation of these energetic particles using PLUTO simulation, which incorporates various microphysics, including diffusion of particles, cooling effects, thermal conduction, etc associated with their propagation through the medium.

The key insight from our analysis is that the observed $1/r$ profile of CR energy density (Aharonian et al., 2019) may not accurately represent its true radial distribution. Moreover, we have shown that the observed data can have a flatter CR energy density profile, particularly when considering revised error estimates. By dividing the projected gamma-ray luminosity (L_γ) by the projected mass within distinct annuli, we have illustrated how this approach can yield a CR energy density profile that differs significantly from the actual distribution. There are other circumstantial reasons why a flatter CR energy density profile should be considered. Recently Abeysekara et al. (2021) have shown that for Cygnus star cluster, the CR energy density above 10 TeV does not strictly follow a $1/r$ profile, and their observation does not rule out CR energy density being uniform, which would make it consistent with our simulation results. At the same time, the CR energy density profile for 100 GeV does follow $1/r$ profile (Aharonian et al., 2019). Abeysekara et al. (2021) interpreted this absence of a $1/r$ profile for TeV CRs on the basis of a larger diffusion rate for higher energy CRs. Furthermore, we have highlighted various uncertainties that complicate straightforward inference, including the absence of morphological symmetry and the uncertainty associated with mass estimation.

Although a $1/r$ profile for CR energy density offers a straightforward explanation, implying a steady-state CR luminosity at the cluster's center, which is conceptually appealing, we have investigated more realistic scenarios. These include the possibility of a time-varying CR luminosity or CR injection occurring outside the central region (such as at the WTS), demonstrating how these scenarios remain consistent with observations. Based on our analysis, we cannot dismiss any of the potential CR acceleration sites solely on observational grounds. This is because the observed luminosity and mass profile can be reconciled with all three CR injection methods, as well as the discrete supernova scenario, through the appropriate selection of diffusion coefficients and injection parameters.

The parameters yielding the best agreement with observations are not arbitrarily chosen but are supported by independent rationales. For instance, a lower diffusion coefficient value (10^{27} cm^2 s^{-1}) can explain the observations in the case of particle acceleration around shocks, whereas a higher value (3×10^{27} cm^2 s^{-1}) is necessary for particle acceleration in the central region. Likewise, the parameter characterizing the efficiency of CR energy injection, found within the range ~ 0.1–0.3, is consistent with prior studies (Gupta et al., 2018b).

Between the Cosmic-Ray 'Knee' and the 'Ankle': Contribution from Star Clusters

In chapter 3, we explored the possibility of a second Galactic CR component which can originate from young massive star clusters, and if these objects can accelerate particles beyond PeV. The standard paradigm of particle acceleration around supernova shocks can accelerate particles up to a maximum of a few times 10^6 GeV (Axford et al., 1977; Lagage & Cesarsky, 1983a). Towards the high-energy spectrum, CRs exceeding approximately 10^9 GeV are believed to originate beyond our Galaxy, potentially emanating from sources such as galaxy clusters (Kang et al., 1996), radio galaxies (Rachen & Biermann, 1993), active galactic nuclei (Mannheim et al., 2000), or gamma-ray bursts (Waxman, 1995). Consequently, there exists a noticeable gap in the energy range between 10^7 and 10^9 GeV (the region between the so-called 'knee' and 'ankle'), leaving the origin of particles within this energy range unexplained. We propose a particle acceleration model in star clusters, distributed in the Galaxy, which can accelerate particles in the above-mentioned energy range of $10^7 - 10^9$ GeV.

Star clusters are distributed all over the Galactic plane, with a Gaussian-like profile having a peak around 4.5 kpc from the Galactic center (Bronfman et al., 2000). Each cluster can accelerate particles according to a power law in momentum (p^{-q}) and with a maximum cutoff momentum (p_c). Depending on different scenarios of acceleration such as particle acceleration at the WTS, acceleration around SNR shocks inside star clusters, etc, particles can achieve a maximum energy of a few tens of PeV, which is higher than the isolated SNR acceleration scenario. CR particles have the potential to attain energies up to 10^8 GeV when supernova remnant (SNR) shocks traverse fast and highly magnetized stellar winds. Additionally, nonlinear effects in the acceleration process further contribute to this high-energy acceleration. Bell (2013); Sushch et al. (2011) emphasize that the outer shocks of SNRs can propel CR particles beyond the "knee" if the shock encounters a magnetic field significantly stronger than the typical interstellar field, a condition that may exist within a star cluster.

Considering suitable elemental compositions in their stellar winds, we introduce a model aimed at generating various nuclei observed in CRs originating from these clusters. We present a detailed calculation of CR transport throughout the Galaxy, which includes accounting for diffusion, interaction losses, and the re-acceleration of CRs by older supernova remnants during their propagation. Our analysis reveals that various acceleration sites inside star clusters such as WTS surrounding star clusters, and SNR shocks inside the star cluster can accelerate protons to energies reaching up to 5×10^7 GeV. It is admittedly a strong claim but it is based on (a) physical motivations regarding the shock structure of WTS and the supernova shocks inside the star clusters, (b) the resulting match with all particle spectrum above 10^{15} eV. For nuclei with a proton number Z, the maximum attainable energy corresponds to $Z \times 5 \times 10^7$ GeV. In our calculations, we have accounted for eight different elements, ranging from hydrogen to iron. By adding all the individual element flux we showed that the total CR contribution from star clusters dominates the energy spectrum between 10^7 and 10^9 GeV. Ultimately, by combining our suggested CRs component originating from star clusters with CRs emanating from Supernova remnants (which prevail up to 10^6 GeV, first Galactic CR component), and extragalactic sources (which dominate beyond 10^9 GeV), we achieve a comprehensive explanation for the entire particle spectrum of CRs, spanning from 1 GeV to 10^{11} GeV. Hence, the CR component from the massive star clusters can act as the second component of Galactic CRs.

Additionally, we have computed the mean logarithmic mass of CRs, which is indicative of CR composition. Our model's projections align with observed trends in the mean logarithmic mass of CRs. Thus, our newly proposed secondary component of Galactic CRs, stemming from young massive star clusters, adeptly accounts for both the entirety of CR spectra and the observed mean logarithmic mass.

TeV spectral bump of cosmic-ray protons and helium nuclei: the role of nearby supernova remnants

In chapter 4, we explored the effect of nearby supernova remnants on the observed spectra of individual CR elements. It is expected that the CR spectrum will adhere to a single power law with an index of -2.7, extending up to approximately 3×10^6 GeV (or 3 PeV), commonly referred to as the CR 'knee'. Above the knee, the spectrum steepens from -2.7 to -3.1, and then flattens back to -2.7 at 4×10^9 GeV, known as the 'ankle'. Eventually, around 10^{11} GeV, the CR spectrum was previously thought to terminate due to the Greisen-Zatsepin-Kuzmin (GZK) cutoff, attributed to interactions with cosmic microwave background (CMB) photons.

Several additional distinctive features are observed in the spectra of individual elements below the knee energy. In this study, we concentrate on recent observations of a bump-like feature in the spectra of protons and helium nuclei by the DAMPE (An et al., 2019; Alemanno et al., 2021) and CALET (Adriani et al., 2022a, 2023) experiments. This feature manifests as a hardening in the spectra at energies of a few hundred GeV, confirming earlier detections by the AMS-02 (Aguilar et al., 2018b) and PAMELA (Adriani et al., 2011) experiments, followed by a subsequent softening around hundreds of TeV. In our work, we have shown that the supernova remnants within a distance of 1 kpc distance from Earth can be a reason behind the origin of the spectral bump. We divide the total CR component into two parts: 1. A diffuse steady-state background CR contribution from the distribution of supernovae in the Galaxy, and 2. Contribution from nearby sources within 1 kpc. This nearby CR component can act as an additional component on top of the diffuse CR background. Combining these two components we can explain the observed spectral bump (i.e. the sudden increase in measured flux) in the energy range of $1-100$ TeV.

In this study, we consider a total of 11 known supernova remnants (SNR) that lie within a radius of ~ 1 kpc as the source of the local component of CRs. We have also considered the all-particle spectrum (available beyond a few PeV), concomitant with the explanation of features in the spectra of individual elements. We use the most recent and accurate measurements of these values. More importantly, we consider a time-dependent escape of CRs (which has not been considered in any previous works) from nearby sources to explain the spectral bump. We use a simple diffusion-only model where we consider the propagation of CR particles through diffusion after escaping from sources before reaching the Earth. We calculate the flux from the source and compare our model prediction with the measurements.

Our model prediction agrees well with the observation for the energy above 10 GeV and hints toward the possibility that the nearby source contribution is necessary to explain the spectral bump around TeV energy. This bump cannot be explained if one only considers the diffuse CR background component. We found the Vela supernova remnant to be the most important nearby source which can significantly affect the spectra. The observed hardening of the proton at 1 TeV can be explained by our assumed model. The time-dependent escape of particles plays a crucial role in explaining the hardening of helium at around a few hundred GeV. Not only proton and helium, our model is consistent with the observation of heavier elements and can explain the spectral hardening for these elements. Our proposed model also aligns with the observed all-particle cosmic-ray spectrum up to $\sim 10^{17}$ eV when an additional component of CRs from young compact star clusters (discussed in chapter 3) in our Galaxy is included.

References

Aartsen M. G., et al., 2013, Phys. Rev. D, 88, 042004

Abeysekara A. U., et al., 2020, Phys. Rev. Lett., 124, 021102

Abeysekara A. U., et al., 2021, Nature Astronomy, 5, 465

Abramowski A., et al., 2012, *A & A*, 537, A114

Ackermann M., et al., 2011, Science, 334, 1103

Ackermann M., et al., 2013, Science, 339, 807

Ackermann M., et al., 2015, *ApJ*, 799, 86

Adriani O., et al., 2011, Science, 332, 69

Adriani O., et al., 2022a, prl, 129, 251103

Adriani O., et al., 2022b, prl, 129, 251103

Adriani O., et al., 2023, prl, 130, 171002

Aghakhanloo M., et al., 2021, Research Notes of the American Astronomical Society, 5, 14

Aguilar M., et al., 2015, prl, 115, 211101

Aguilar M., et al., 2018a, prl, 120, 021101

Aguilar M., et al., 2018b, prl, 120, 021101

Aharonian F. A., Atoyan A. M., Voelk H. J., 1995, *A & A*, 294, L41

Aharonian F., et al., 2007, *ApJ*, 661, 236

Aharonian F., et al., 2009, *A & A*, 508, 561

Aharonian F., Yang R., de Oña Wilhelmi E., 2019, Nature Astronomy, 3, 561

Aharonian F., et al., 2022, *A & A*, 666, A124

Ahn H. S., et al., 2009, *ApJ*, 707, 593

Alemanno F., et al., 2021, prl, 126, 201102

Alessandra P. A., 2017, Revista Brasileira de Ensino de F´ısica,

Aloisio R., Berezinsky V., Gazizov A., 2012, Astroparticle Physics, 39, 129

Amenomori M., et al., 2008, *ApJ*, 678, 1165

Amsler C., et al., 2008, Physics Letters B, 667, 1

An Q., et al., 2019, Science Advances, 5, eaax3793

Antoni T., et al., 2005, Astroparticle Physics, 24, 1

Ave M., Boyle P. J., Gahbauer F., Höppner C., Hörandel J. R., Ichimura M., Müller D., Romero-Wolf A., 2008, *ApJ*, 678, 262

Axford W. I., 1994, *ApJ Suppl.*, 90, 937

Axford W. I., Leer E., Skadron G., 1977, in International Cosmic Ray Conference. p. 132

Bagnulo S., et al., 2020, *A & A*, 635, A163

Bartoli B., et al., 2014, *ApJ*, 790, 152

Beasor E. R., Davies B., Smith N., Gehrz R. D., Figer D. F., 2021, *ApJ*, 912, 16

Bell A. R., 1978, *MNRAS*, 182, 147

Bell A. R., 2013, Astroparticle Physics, 43, 56

Bell A. R., 2015, *MNRAS*, 447, 2224

Bell A. R., Lucek S. G., 2001, *MNRAS*, 321, 433

Berezhko E. G., 1996, Astroparticle Physics, 5, 367

Berezhko E. G., Ksenofontov L. T., Ptuskin V. S., Zirakashvili V. N., Völk H. J., 2003, aap, 410, 189

Berezhko E. G., Pühlhofer G., Völk H. J., 2009, *A & A*, 505, 641

Berezhnev S. F., 2015, Proc. 33rd ICRC, Paper ID 326

Berezinsky V., Gazizov A., Grigorieva S., 2006, Phys. Rev. D, 74, 043005

Beringer J., et al., 2012, Phys. Rev. D, 86, 010001

Bernard G., Delahaye T., Keum Y. Y., Liu W., Salati P., Taillet R., 2013, *A & A*, 555, A48

Bhadra S., Gupta S., Nath B. B., Sharma P., 2022, *MNRAS*, 510, 5579

Bhadra S., Thoudam S., Nath B. B., Sharma P., 2024, *ApJ*, 961, 215

Biermann P. L., Cassinelli J. P., 1993, *A & A*, 277, 691

Biermann P. L., Becker J. K., Dreyer J., Meli A., Seo E.-S., Stanev T., 2010, *ApJ*, 725, 184

Biermann P. L., et al., 2018, Advances in Space Research, 62, 2773

Blandford R. D., Ostriker J. P., 1978, *ApJL*, 221, L29

Blasi P., 2013, *A & A Rev.*, 21, 70

Blasi P., 2017, *MNRAS*, 471, 1662

Blasi P., Amato E., 2012, jcap, 2012, 011

Blasi P., Amato E., Serpico P. D., 2012, prl, 109, 061101

Blazère A., Neiner C., Tkachenko A., Bouret J. C., Rivinius T., 2015, *A & A*, 582, A110

Breitschwerdt D., Dogiel V. A., Völk H. J., 2002, *A & A*, 385, 216

Bronfman L., Casassus S., May J., Nyman L. Å., 2000, *A & A*, 358, 521

Büsching I., Kopp A., Pohl M., Schlickeiser R., Perrot C., Grenier I., 2005, *ApJ*, 619, 314

Bustard C., Zweibel E. G., Cotter C., 2017, *ApJ*, 835, 72

Bykov A. M., 2014, *A & A Rev.*, 22, 77

Bykov A. M., Toptygin I. N., 2001, Astronomy Letters, 27, 625

Bykov A. M., Ellison D. C., Gladilin P. E., Osipov S. M., 2015, *MNRAS*, 453, 113

Bykov A. M., Ellison D. C., Gladilin P. E., Osipov S. M., 2018, Advances in Space Research, 62, 2764

Bykov A. M., Marcowith A., Amato E., Kalyashova M. E., Kruijssen J. M. D., Waxman E., 2020, *Space Sci. Rev.*, 216, 42

Cao Z., et al., 2021, *Nature*, 594, 33

Cappiello C. V., Avis Kozar N. P., Vincent A. C., 2023, prd, 107, 035003

Caprioli D., Blasi P., Amato E., 2009, *MNRAS*, 396, 2065

Caprioli D., Blasi P., Amato E., 2011, Astroparticle Physics, 34, 447

Cesarsky C. J., Montmerle T., 1983, *Space Sci. Rev.*, 36, 173

Chevalier R. A., 1983, *ApJ*, 272, 765

Chevalier R. A., Clegg A. W., 1985, *Nature*, 317, 44

Cowsik R., Burch B., 2010, prd, 82, 023009

Cowsik R., Lee M. A., 1979, *ApJ*, 228, 297

Cowsik R., Madziwa-Nussinov T., 2016, *ApJ*, 827, 119

Dampe Collaboration 2022, Science Bulletin, 67, 2162

Dermer C. D., 1986, *A & A*, 157, 223

Dickinson C., 2018, Galaxies, 6, 56

Diehl R., et al., 2006, *Nature*, 439, 45

Drury L. O., Voelk J. H., 1981, *ApJ*, 248, 344

Drury L. O., Aharonian F. A., Voelk H. J., 1994, *A & A*, 287, 959

Eichler D., 2017, *ApJ*, 842, 50

Eichler D., Usov V., 1993, *ApJ*, 402, 271

Engelmann J. J., et al., 1990, *A & A*, 233, 96

Erlykin A. D., Wolfendale A. W., 2012, Astroparticle Physics, 35, 449

Faherty J., Walter F. M., Anderson J., 2007, *Astrophys. Space Sci.*, 308, 225

Ferland G. J., Korista K. T., Verner D. A., Ferguson J. W., Kingdon J. B., Verner E. M., 1998, *Pub. Astron. Soc. Pac.*, 110, 761

Fermi E., 1949, Phys. Rev., 75, 1169

Ferrand G., Marcowith A., 2010, *A & A*, 510, A101

Fesen R. A., Weil K. E., Cisneros I. A., Blair W. P., Raymond J. C., 2018, *MNRAS*, 481, 1786

Finke J. D., Dermer C. D., 2012, *ApJ*, 751, 65

Gabici S., Aharonian F. A., Casanova S., 2009, *MNRAS*, 396, 1629

Gabici S., Casanova S., Aharonian F. A., Rowell G., 2010, in Boissier S., Heydari-Malayeri M., Samadi R., Valls-Gabaud D., eds, SF2A-2010: Proceedings of the Annual meeting of the French Society of Astronomy and Astrophysics. p. 313 (`arXiv:1009.5291`), doi:10.48550/arXiv.1009.5291

Gabici S., Evoli C., Gaggero D., Lipari P., Mertsch P., Orlando E., Strong A., Vittino A., 2019, International Journal of Modern Physics D, 28, 1930022

Gaggero D., Zandanel F., Cristofari P., Gabici S., 2018, *MNRAS*, 475, 5237

Gaisser T. K., 1990, Cosmic rays and particle physics.

Ginzburg V. L., Syrovatskii S. I., 1964, The Origin of Cosmic Rays

Giuliani A., et al., 2010, *A & A*, 516, L11

Gleeson L. J., Axford W. I., 1968, *ApJ*, 154, 1011

Góra D., Pierre Auger Collaboration 2018, Universe, 4, 128

Greisen K., 1966, prl, 16, 748

Guo F., Oh S. P., 2008, *MNRAS*, 384, 251

Gupta S., Nath B. B., Sharma P., Shchekinov Y., 2016, *MNRAS*, 462, 4532

Gupta S., Nath B. B., Sharma P., Eichler D., 2018a, *MNRAS*, 473, 1537

Gupta S., Nath B. B., Sharma P., 2018b, *MNRAS*, 479, 5220

Gupta S., Nath B. B., Sharma P., Eichler D., 2020, *MNRAS*, 493, 3159

Gupta S., Sharma P., Mignone A., 2021, *MNRAS*, 502, 2733

Gvaramadze V. V., 2006, *A & A*, 454, 239

H. E. S. S. Collaboration et al., 2018a, *A & A*, 612, A4

H. E. S. S. Collaboration et al., 2018b, *A & A*, 612, A6

H. E. S. S. Collaboration et al., 2018c, *A & A*, 612, A6

H. E. S. S. Collaboration et al., 2023, *A & A*, 673, A148

Heger A., Langer N., Woosley S. E., 2000, *ApJ*, 528, 368

Heger A., Woosley S. E., Spruit H. C., 2005, *ApJ*, 626, 350

Heitler W., 1954, Quantum theory of radiation

Hewitt J. W., Lemoine-Goumard M., 2015, Comptes Rendus Physique, 16, 674

Higdon J. C., Lingenfelter R. E., 2003, *ApJ*, 590, 822

Higdon J. C., Lingenfelter R. E., 2005, *ApJ*, 628, 738

Higdon J. C., Lingenfelter R. E., 2013, *ApJ*, 775, 110

Higdon J. C., Lingenfelter R. E., Ramaty R., 1998, *ApJL*, 509, L33

High Resolution Fly'S Eye Collaboration et al., 2009, Astroparticle Physics, 32, 53

Hillas A. M., 1967, Physics Letters A, 24, 677

Hillas A. M., 1984, *Anu Rev. in Astronomy and Astrophysics.*, 22, 425

Hörandel J. R., 2003, Journal of Physics G Nuclear Physics, 29, 2439

Jana R., Roy M., Nath B. B., 2020, *ApJL*, 903, L9

Jokipii J. R., Morfill G., 1987, *ApJ*, 312, 170

Jones F. C., Lukasiak A., Ptuskin V., Webber W., 2001, *ApJ*, 547, 264

Kääpä A., Kampert K.-H., Becker Tjus J., 2023, in European Physical Journal Web of Conferences. p. 03006, doi:10.1051/epjconf/202328303006

Kampert K.-H., Unger M., 2012, Astroparticle Physics, 35, 660

Kang H., Ryu D., Jones T. W., 1996, *ApJ*, 456, 422

Katz-Stone D. M., Kassim N. E., Lazio T. J. W., O'Donnell R., 2000, *ApJ*, 529, 453

Kelner S. R., Aharonian F. A., Bugayov V. V., 2006, Phys. Rev. D, 74, 034018

Knödlseder J., 2013, in Torres D. F., Reimer O., eds, Astrophysics and Space Science Proceedings Vol. 34, Cosmic Rays in Star-Forming Environments. p. 169, doi:10.1007/978-3-642-35410-6_13

Knurenko S. P., Sabourov A., 2011, Astrophysics and Space Sciences Transactions, 7, 251

Kobayashi T., Komori Y., Yoshida K., Nishimura J., 2004, *ApJ*, 601, 340

Lagage P. O., Cesarsky C. J., 1983a, *A & A*, 125, 249

Lagage P. O., Cesarsky C. J., 1983b, *A & A*, 125, 249

Lazendic J. S., Slane P. O., 2006, *ApJ*, 647, 350

Leahy D. A., Tian W. W., 2007, *A & A*, 461, 1013

Leitherer C., et al., 1999, *ApJ Suppl.*, 123, 3

Lerche I., Schlickeiser R., 1982, *A & A*, 116, 10

Li H., Chen Y., 2010, *MNRAS*, 409, L35

Li A., Liu W., Guo Y., 2024, Symmetry, 16, 236

Longair M. S., 1992, High energy astrophysics. Vol.1: Particles, photons and their detection

Lund N., 1984, Advances in Space Research, 4, 5

Maeder A., Meynet G., 1993, *A & A*, 278, 406

Malkov M. A., Moskalenko I. V., 2021, *ApJ*, 911, 151

Mannheim K., Protheroe R. J., Rachen J. P., 2000, Phys. Rev. D, 63, 023003

Mao C. Y., Shen C. S., 1972, Chinese Journal of Physics, 10, 16

Marcowith A., Lemoine M., Pelletier G., 2006, *A & A*, 453, 193

Maurin D., Melot F., Taillet R., 2014, *A & A*, 569, A32

Maxted N. I., et al., 2018, *ApJ*, 866, 76

Merten L., Bustard C., Zweibel E. G., Becker Tjus J., 2018, *ApJ*, 859, 63

Mertsch P., 2011, jcap, 2011, 031

Mignone A., Bodo G., Massaglia S., Matsakos T., Tesileanu O., Zanni C., Ferrari A., 2007, *ApJ Suppl.*, 170, 228

Montmerle T., 1979, *ApJ*, 231, 95

Morlino G., 2017, in Alsabti A. W., Murdin P., eds, , Handbook of Supernovae. p. 1711, doi:10.1007/978-3-319-21846-5_11

Morlino G., Blasi P., Peretti E., Cristofari P., 2021, *MNRAS*, 504, 6096

Mueller D., Swordy S. P., Meyer P., L'Heureux J., Grunsfeld J. M., 1991, *ApJ*, 374, 356

Muno M. P., Law C., Clark J. S., Dougherty S. M., de Grijs R., Portegies Zwart S., Yusef-Zadeh F., 2006, *ApJ*, 650, 203

Nath B. B., Eichler D., 2020, *MNRAS*, 499, L1

Negueruela I., González-Fernández C., Marco A., Clark J. S., Martínez-Núñez S., 2010, *A & A*, 513, A74

Neiner C., Grunhut J., Leroy B., De Becker M., Rauw G., 2015, *A & A*, 575, A66

Obermeier A., Ave M., Boyle P., Höppner C., Hörandel J., Müller D., 2011, *ApJ*, 742, 14

Oey M. S., Clarke C. J., 1997, *MNRAS*, 289, 570

Ohira Y., Murase K., Yamazaki R., 2011, *MNRAS*, 410, 1577

Panov A. D., et al., 2006, arXiv e-prints, pp astro–ph/0612377

Panov A. D., et al., 2007, Bulletin of the Russian Academy of Sciences, Physics, 71, 494

Parizot E., 2014, Nuclear Physics B Proceedings Supplements, 256, 197

Parizot E., Drury L., 1999, *A & A*, 349, 673

Pfrommer C., Enßlin T. A., 2004, *A & A*, 413, 17

Pfrommer C., Pakmor R., Schaal K., Simpson C. M., Springel V., 2017, *MNRAS*, 465, 4500

Poelarends A. J. T., Herwig F., Langer N., Heger A., 2008, *ApJ*, 675, 614

Pohl M., Dwarkadaas V., Igor T., 2011, ICRC,2011

Ptuskin V. S., Jones F. C., Seo E. S., Sina R., 2006, Advances in Space Research, 37, 1909

Ptuskin V., Zirakashvili V., Seo E.-S., 2013, *ApJ*, 763, 47

Rachen J., 2015, Proc. 28th Texas Symp. Relativ. Astrophys., Geneva, Switzerland, 13–18 December 2015, Electronic Proceedings, 230

Rachen J. P., Biermann P. L., 1993, *A & A*, 272, 161

Reville B., Bell A. R., 2012, *MNRAS*, 419, 2433

Roy A., Dopita M. A., Krumholz M. R., Kewley L. J., Sutherland R. S., Heger A., 2021, *MNRAS*, 502, 4359

Rybicki G. B., Lightman A. P., 1979, Astronomy Quarterly, 3, 199

Ryu D., Das S., Kang H., 2010, *ApJ*, 710, 1422

Salpeter E. E., 1955, *ApJ*, 121, 161

Sander A., Hamann W. R., Todt H., 2012, *A & A*, 540, A144

Sarkar K. C., Nath B. B., Sharma P., Shchekinov Y., 2015, *MNRAS*, 448, 328

Satyendra T., 2006, *MNRAS*, 370, 263

Schlickeiser R., 2002, Cosmic Ray Astrophysics

Schure K. M., Bell A. R., 2013, *MNRAS*, 435, 1174

Shara M. M., Hurley J. R., 2002, *ApJ*, 571, 830

Sharma P., Roy A., Nath B. B., Shchekinov Y., 2014, *MNRAS*, 443, 3463

Simpson J. A., 1983, Annual Review of Nuclear and Particle Science, 33, 323

Smartt S. J., Eldridge J. J., Crockett R. M., Maund J. R., 2009, *MNRAS*, 395, 1409

Spitzer L., 1962, Physics of Fully Ionized Gases

Strong A. W., Moskalenko I. V., 1998, *ApJ*, 509, 212

Strong A. W., Moskalenko I. V., Porter T. A., Jóhannesson G., Orlando E., Digel S. W., 2009, arXiv e-prints, p. arXiv:0907.0559

Sushch I., Hnatyk B., Neronov A., 2011, *A & A*, 525, A154

Sutherland R. S., Dopita M. A., 1993, *ApJ Suppl.*, 88, 253

Suzuki H., Bamba A., Yamazaki R., Ohira Y., 2022, *ApJ*, 924, 45

Taillet R., Maurin D., 2003, *A & A*, 402, 971

Tatischeff V., Raymond J. C., Duprat J., Gabici S., Recchia S., 2021, *MNRAS*, 508, 1321

The Pierre Auger Collaboration et al., 2013, arXiv e-prints, p. arXiv:1307.5059

The Pierre Auger Collaboration et al., 2015, arXiv e-prints, p. arXiv:1509.03732

Thoudam S., 2007, *MNRAS*, 378, 48

Thoudam S., 2008, *MNRAS*, 388, 335

Thoudam S., Hörandel J. R., 2012a, *MNRAS*, 419, 624

Thoudam S., Hörandel J. R., 2012b, *MNRAS*, 421, 1209

Thoudam S., Hörandel J. R., 2012c, *MNRAS*, 421, 1209

Thoudam S., Hörandel J. R., 2012d, *MNRAS*, 421, 1209

Thoudam S., Hörandel J. R., 2013, *MNRAS*, 435, 2532

Thoudam S., Hörandel J. R., 2014, *A & A*, 567, A33

Thoudam S., Rachen J. P., van Vliet A., Achterberg A., Buitink S., Falcke H., Hörandel J. R., 2016, *A & A*, 595, A33

Tibet ASγ Collaboration et al., 2021, Nature Astronomy, 5, 460

Tomassetti N., 2012, apjl, 752, L13

Unger M., Farrar G. R., Anchordoqui L. A., 2015, Phys. Rev. D, 92, 123001

Vieu T., Reville B., 2023, *MNRAS*, 519, 136

Vieu T., Reville B., Aharonian F., 2022, *MNRAS*, 515, 2256

Voelk H. J., Biermann P. L., 1988, *ApJL*, 333, L65

Wandel A., Eichler D., Letaw J. R., Silberberg R., Tsao C. H., 1987, *ApJ*, 316, 676

Waxman E., 1995, Phys. Rev. Lett., 75, 386

Weaver R., McCray R., Castor J., Shapiro P., Moore R., 1977, *ApJ*, 218, 377

Webb G. M., Axford W. I., Forman M. A., 1985, *ApJ*, 298, 684

Webber W. R., 1983, in Shapiro M. M., ed., NATO Advanced Study Institute (ASI) Series C Vol. 107, Composition and Origin of Cosmic Rays. pp 83–100

Webber W. R., Soutoul A., 1998, *ApJ*, 506, 335

Werner M., Kissmann R., Strong A. W., Reimer O., 2015, Astroparticle Physics, 64, 18

Wiebel-Sooth B., Biermann P. L., Meyer H., 1998, *A & A*, 330, 389

Wiedenbeck M. E., et al., 1999, *ApJL*, 523, L61

Williams J. P., McKee C. F., 1997, *ApJ*, 476, 166

Yadav N., Mukherjee D., Sharma P., Nath B. B., 2017, *MNRAS*, 465, 1720

Yar-Uyaniker A., Uyaniker B., Kothes R., 2004, *ApJ*, 616, 247

Yoon Y. S., et al., 2011, *ApJ*, 728, 122

Yuan Q., Zhang B., Bi X.-J., 2011, prd, 84, 043002

Yue C., et al., 2019, Frontiers of Physics, 15, 24601

Zatsepin G. T., Kuz'min V. A., 1966, Soviet Journal of Experimental and Theoretical Physics Letters, 4, 78

Zatsepin V. I., Sokolskaya N. V., 2006, *A & A*, 458, 1

Zirakashvili V. N., Völk H. J., 2006, Advances in Space Research, 37, 1923

di Matteo A., 2015, for the Pierre Auger Collaboration 2015, POS(ICRC2015)249